1-1-2003

Starting and unstarting of hypersonic air inlets

Rabi Bin Tahir
Ryerson University

RYERSON UNIVERSITY

Faculty of Engineering and Applied Science

STARTING AND UNSTARTING OF HYPERSONIC AIR INLETS

BY

RÅBI BIN TAHIR

Bachelor of Engineering (B. Eng)
Faculty of Engineering and Applied Science
Ryerson Polytechnic University. June, 2000.

A thesis presented to Ryerson University
in partial fulfillment of the requirement for
the degree of Master of Applied Science in
the Program of Mechanical Engineering.

Toronto, Ontario, Canada.

Your file Votre référence
ISBN: 0-612-85325-X
Our file Notre référence
ISBN: 0-612-85325-X

This thesis is submitted in partial fulfillment of the requirements for the degree of Master of Applied Science in the program of Mechanical Engineering. All material in this thesis which is not my own work has been identified and no material is included for which a degree has previously been conferred. I authorise Ryerson University to lend this thesis to other institutions or individuals for the purpose of scholarly research.

Råbi Bin Tahir

I further authorise Ryerson University to reproduce this thesis, provided that the quality of reproduction is not significantly deteriorated, by photocopying or by other means, in total or in part, at the request of other institutions or individuals for the purpose of scholarly research. Further, this notice shall accompany any such reproduction to limit degradation of quality resulting from further reproduction.

Råbi Bin Tahir

Starting and Unstarting

of

Hypersonic Air Inlets

Approved on August 29, 2003, by:

Sannu Mölder	Paul Walsh
David Naylor	David Greatrix

Gregory Kawall (Chairperson)

The final copy of this thesis has been examined by the signatories, and we find that both the content and the form meet acceptable presentation standards of scholarly work in its discipline.

Ryerson University requires the signatures of all persons using or photocopying this thesis. Please sign below, and give address and date. If you find this work useful or would like to send comments, the author may be reached through e-mail: rbt@rogers.com

Contents

List of Tables

List of Figures

List of Symbols

β Compression parameter in the limiting process, page 35

δ Local flow deflection, page 29

δ_{ij} Kronecker delta function, page 33

ϵ Filter coefficient for Adaptive Mesh Refinement (AMR), page 38

ϵ Internal energy per unit mass, page 33

γ Ratio of specific heats, page 14

μ Local Mach angle, page 29

Ω Control volume, page 33

Ω_e Volumes of sub-elements formed about a node, page 35

ρ Density, page 14

A_∞ Free stream capture area, page 14

A_e Area at the exit plane, page 14

A_i Area at the entrance plane, page 14

a_i Acceleration along coordinate-i, page 34

A_s Area associated with sonic flow (isentropic diffusion process), page 14

A_t Area at the throat, page 14

c Signal velocity (absolute speed of sound in air), page 14

d Cell-wise local characteristic scale for AMR, page 38

e Total energy per unit volume, page 33

E_i Cell-wise local error measure for AMR, page 37

I_{sp} Specific impulse, page 4

M Local Mach number, page 2

M_∞ Free stream Mach number, page 14

$m_{\max}$ Upper limit on global level for AMR, page 37

$m_{\min}$ Lower limit on global level for AMR, page 37

M_θ Azimuthal Mach number in Taylor-Maccoll equation for conical flow, page 28

M_D Free stream Mach number at which the throat flow is sonic after isentropic diffusion ("design" value for isentropic diffuser), page 14

m_i Cell-wise local level for AMR, page 37

M_r Radial Mach number in Taylor-Maccoll equation for conical flow, page 28

M_S Free stream Mach number at which the shock swallowing process begins (pseudo-steady "starting" value for isentropic diffuser), page 14

p Pressure, page 14

R Gas constant, page 14

s_{ij} Control volume surface associated with volumes i and j, page 36

T Temperature, page 14

t Temporal dimension, page 14

T_c Coarsening threshold for AMR, page 37

T_r Refinement threshold for AMR, page 37

$\mathrm{d}\Omega$ Closed surface bounding Ω, page 33

$\mathbf{F}^j$ Convective flux of $\mathbf{U}$ (j is the contravariant index), page 33

$\mathbf{n}$ Outward-pointing normal to $\mathrm{d}\Omega$, page 33

$\mathbf{U}$ Vector of conserved quantities, page 33

$\vec{u}$ Vector of unknown quantities in a set of ODEs, page 28

u Velocity, page 14

$\mathbf{V}$ Vector of primitive variables, page 33

(r, θ) Location in polar coordinates along the cardinal streamline, page 28

$(x, y)_\beta$ Location in cartesian coordinates along the C^- characteristic, page 28

x Spatial dimension in cartesian coordinate system, page 13

Abstract

Starting and Unstarting of Hypersonic Air Inlets

Master of Applied Science, 2003

Råbi Bin Tahir

Faculty of Engineering and Applied Science, Ryerson University

This thesis concerns a technical hurdle that must be overcome in relation to air-breathing propulsion technologies for future space access vehicles—it discusses the flow starting process in supersonic and hypersonic air-inlets. A study is conducted, with the aid of numerical simulations, based on an inviscid model of a thermally perfect gas.

Effects of boundary-imposed temporal and spatial gradients on the *inlet starting phenomenon* are documented for the first time. It is shown that purely accelerative starting is generally not possible, for inlets of any positive contraction, unless thousands of g's of acceleration are imposed. It is proposed that removal of frangible structures, such as fast rupturing diaphragms, be used to impose sufficiently high spatial gradients, as necessary to permit starting beyond Kantrowitz' limit. It is shown that, for a perforated diffuser, starting takes place if a sonic line, at the leading edge of a slit, occurs at an area ratio equal to, or higher than, that corresponding to Kantrowitz' limit.

Acknowledgements

In the following pages is compiled a (nearly two year long) focused effort that has benefited from the experience, guidance, and support of many individuals. In the following lines, I would like to single-out *some* of these people.

Firstly, I hereby acknowledge the unconditional love and support afforded to me by my parents. I am conscious of their personal sacrifices and I am grateful to them for it all, and promise never to place them in an old folks home. I am thankful also to the, albeit troublesome, brother they provided.

Prof. Sannu Mölder played an instrumental role in arranging financial support during the second year of my studies, and also provided continuing technical supervision, help and advice throughout.

I am also grateful to Dr. F. S. Billig for providing useful technical comments and insight, and also for his influential role and continuing efforts in arranging support for this research effort.

I would like to single out Prof. Eugene Timofeev for his encouragement, patience and most importantly his friendship. He has made invaluable contributions to my research and provided countless TEXnical suggestions with diligent care and effort to make this document a better one.

The author wishes to extend gratitude to Prof. Paul Walsh for supervision of this thesis. I am much obliged to him for providing valuable suggestions in the

editing of work presented herein.

I would like to acknowledge Dr. S. M. Alvi as well as Dr. D. Greatrix, for they deserve a mention in performing the most painstaking task of all—that of proof-reading. While some punctuation has survived, many a comma are no more, thanks to their keen eyes.

Lastly, the author is grateful to all his friends for *everything*, both good and bad. I hesitate and can not name you in fear that some may get offended that I dared consider us friends.

Financial support

This research effort has been financially supported in part by Taitech, Inc. under subcontract TS02-37-002 to S. Molder and Associates.

Chapter 1

Introduction

1.1 Historical Perspective

Mankind has an innate urge to explore, and ofttimes this quest necessitates invention of new vehicles and means of travel. The twentieth century saw an unprecedented growth in the transportation of people over long distances as the means of travel became safer and ever faster. Automobiles and aeroplanes may now be considered vehicles economically accessible to the masses.

1.1.1 The Three Flight Regimes

From the incompressible flight regime experienced by the 35 mph Wright flyer at sea level in 1903 to fighter aircraft with 400 mph compressible flow at 30 000 ft in World War II (WWII), the flow regime remained entirely *subsonic*[†]. All this changed late in 1947 with Bell XS-1, the first manned rocket propelled airplane

[†]Slower than speed of sound (Mach number is less than unity; Mach number is a dimensionless parameter that is indicative of compressibility effects, and is defined as the ratio of local flow velocity to local signal velocity).

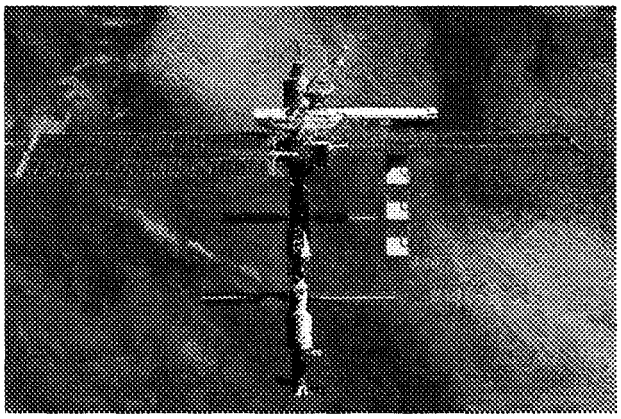

Figure 1.1: ISS photographed by a crew member on board the space shuttle Atlantis following the undocking of the two spacecraft, October 16, 2002 [20]. The ISS has an orbital altitude of 361 km at perigee and 437 km at apogee (*ibid.*).

to finally break the sound barrier. With the jet powered AVRO Arrow sustaining Mach 1.98 at 50 000 ft in 1958 and the rocket powered X-15 airplane achieving Mach 5.27 in 1961 and later reaching an astounding altitude of 354 200 ft in 1963, *supersonic*[†] and *hypersonic*[‡] flight near edge of space had been well demonstrated.

1.1.2 Space Transport

In the past few decades, unmanned probes have been sent to most of the planets in our solar system and man has even set foot on the Moon. Today, hundreds of man-made satellites are orbiting earth; technological advances in the more recent years have even lead to the establishment of an international space station (Fig. 1.1).

Routine access to space, however, offers unique challenges and as a result, the cost of space travel, even to Low Earth Orbit(s) (LEO)*, to date has been extremely high. The high cost of space travel is due in part to the fact that a

[†]Faster than speed of sound (Mach number > 1).

[‡]Much faster than speed of sound (usu. considered as $M > 5$).

*LEO is usually considered up to 3 000 km above earth's surface.

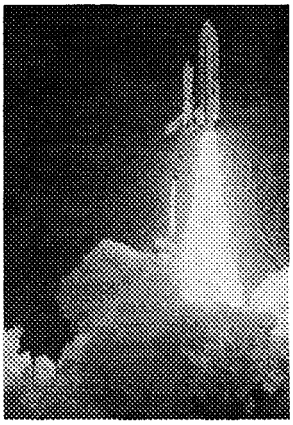

Figure 1.2: Launch view of Columbia for the STS-1 mission, April 12, 1981 [20].

large amount of energy is required to attain orbital altitudes and speeds. Robert A. Heinlein, the late, great science fiction writer, put it so eloquently when he said [21], "Reach low [earth] orbit and you are halfway to anywhere in the solar system." In fact, orbital velocity for a typical LEO is around 8 km/s, whereas the escape velocity is about 11 km/s. An additional amount of energy, roughly equal to that required for a typical LEO flight, would be sufficient for a space ship to reach any destination in the solar system. Indeed, for orbital vehicles, this fact determines the required amount of onboard fuel and its high ratio to payload.

1.1.3 Rocket Technology

The Space Transportation System (STS), designed during the 1970s at National Aeronautics and Space Administration (NASA), relies on phenomenal rocket power to soar beyond the atmosphere itself. It uses rocket technology to launch shuttles into low earth orbits—a technology that requires carrying onboard oxidiser to burn the fuel even during the atmospheric phase of flight. As a result, a significant portion of the total weight of the vehicle at take-off is in fuel oxidiser.

The space shuttle (Fig. 1.2) uses two Solid Rocket Booster(s) (SRB) that provide 72% of the thrust in the initial boost phase; nearly 70% of the boosters' weight at liftoff is in fuel oxidiser [21]. The remaining 28% of the thrust is provided by the three engines that are supplied fuel from an external tank (ET), of which more than 81% is liquid oxygen by weight [21].

1.2 Propulsion For Future Space Planes

One way to reduce the overall cost is to improve the specific impulse[†] (I_{sp}). The higher the I_{sp} value, the better the performance; a higher value of I_{sp} indicates that for a given amount of fuel, the same amount of thrust can be generated for a longer time period. Although I_{sp} values for any given propulsion technology will vary, to gain some perspective, it might be instructive to examine some characteristic values. A quick survey reveals: a typical solid rocket has an I_{sp} value around 250 seconds; this, compared to 3 500 to 1 500 seconds for a turbojet operable at low subsonic to high supersonic speeds ($0 < M < 3$); 1 500 to 500 for a ramjet operable at ($2 < M < 5$), and perhaps 1 000 for a scramjet operable at hypersonic flight speeds ($M > 5$), limited by altitude, *i.e.*, up to approximately 40 km above earth's surface. Thus, the higher I_{sp} value is a major advantage shared by various kinds of air-breathing engines over rockets. On the other hand, rockets generate thrust efficiently outside the atmosphere in a vacuum. At high altitudes (above 40 km), there is too little oxygen for air-breathing engines to function, and oxidiser must be carried onboard to travel outside the atmosphere. For future space planes, the above considerations will likely lead to a propulsive device, utilising a combination of air-breathing and rocket-based technologies.

[†]Here, specific impulse is defined as the thrust produced per unit weight (on earth), of fuel consumed per unit of time.

1.2.1 Ramjets and Scramjets

Even though some amount of oxidiser must be carried onboard to attain a LEO, undoubtedly, a significant portion of the boost phase could utilise oxygen present in the earth's atmosphere—so long as efficient air-breathing engines can be designed. In the early 1960s, the United States Air Force (USAF) considered the concept of an aerospace plane relying primarily on air-breathing propulsion provided by scramjets [1]. Work on an early aerospace plane was cancelled in October 1963 due mainly to the design requirements exceeding the state of the art at that time. The idea was later resurrected in the mid-1980s by Defense Advanced Research Projects Agency (DARPA), alongside NASA and others, with the object to create a fully reusable single-stage-to-orbit (SSTO) vehicle, but no successful National Aerospace Plane (NASP) design could be produced (*ibid.*). Lately, there has been a resurgence of similar ideas that employ Rocket Based Combined Cycle (RBCC) [2] engines for application to transport as well as to missiles for defence purposes; presently, there is a sense of urgency in finding solutions to the unique problems associated with hypersonic propulsion. Indeed, hypersonic vehicle designs for the twenty-first century will require an integrated airframe propulsion system that will fully utilise the oxygen present in the atmosphere.

For air-breathing engines to work, the air stream is first compressed to high pressures (*e.g.*, 30 times the free-stream value). Fuel is then added to a stable high pressure stream in the injector section, which is burnt in the combustor section, thus increasing the internal energy of the air mass. This energy is then converted to kinetic energy as the mass is accelerated through a nozzle providing net thrust. Jet engines are limited by structural materials that can withstand only limited temperatures, and conventional turbojets become inoperable much beyond Mach 3. In a ramjet engine, the air inlet takes a supersonic stream (*e.g.*, Mach 3 to 5)

and efficiently compresses it to a subsonic stream. Thus, combustion in a ramjet occurs within a subsonic stream. At hypersonic velocities, total[†] temperatures are progressively higher and high temperature effects [1] become significant. Slowing the gas molecules can cause vibrational excitation and dissociation, and may even lead to ionisation of the molecules. These effects are detrimental to engine performance; thus, at hypersonic speeds, it is more efficient to have supersonic combustion (*e.g.*, scramjet operation up to Mach 15).

1.3 Air Inlets

An important aspect of supersonic and hypersonic air-breathing engines is the air inlet[‡]. At various flight conditions, efficient compression of the free-stream is of paramount importance, so that high total pressure recovery is desired. To this end, many inlet designs exist for supersonic and hypersonic applications and generally fall under one of two main classes: 1) internal compression and 2) external compression. Most designs can be further subclassified as having either planar (two-dimensional) or axisymmetric flow geometry. External compression, axisymmetric inlets are commonly known as spike inlets, *e.g.*, Oswatitsch-based designs (Fig. 1.3). Internal- and external-compression planar inlets also exist, *e.g.*, designs based on Prandtl-Meyer theory (Fig. 1.4). Internal compression inlets based on conical flow symmetry are particularly efficient, *e.g.*, Busemann-based designs (Fig. 1.5).

A study, juxtaposing these designs, was conducted in the early 1990s by various researchers, and the interested reader is referred to Ref. [17] for further details.

[†]In the gas dynamics sense, total refers to stagnation, *i.e.*, the total available in the stream.
[‡]The common British term for the same device is air-intake.

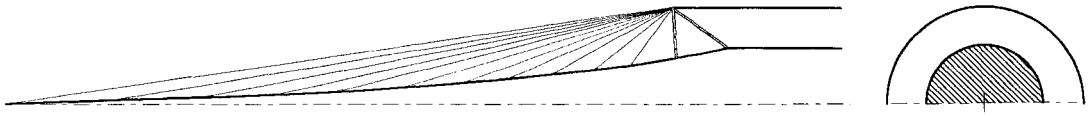

Figure 1.3: Schematic representation of Oswatitsch-based inlet-design.

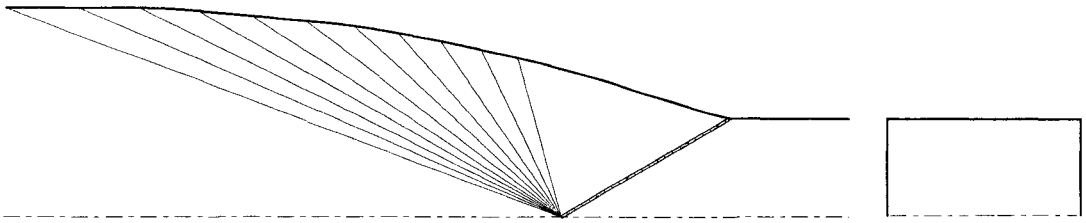

Figure 1.4: Mach lines in a prototypal, internal compression, Prandtl-Meyer inlet.

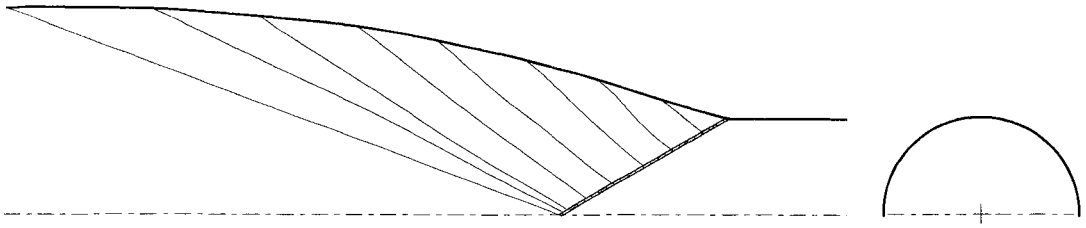

Figure 1.5: Mach lines in a Busemann model-inlet.

1.3.1 Starting Characteristics of Basic Inlets

The basic idea here is to develop methods of establishing started flow in high contraction inlets. The reader will note that the area contraction is not always fixed, and temporarily lowering the contraction facilitates starting; this point will become clear, once the theoretical limitations on starting have been examined.

External compression inlets are generally considered easier to *start* than internal compression inlets because of a built-in mechanism, which is present in the former—the effective area contraction in external compression inlets is significantly reduced (in the unstarted mode), and this facilitates the starting process.

Planar inlets are usually the easiest to start, because it is relatively easy to employ variable geometry in such inlets; the effective area contraction can be (mechanically) lowered during the starting process.

There is little opportunity for overboard spillage in internal compression geometries. As such, the basic Busemann inlets (described in Article 2.3), prove to be among the most challenging, and in relation to general inlet starting, these ideas will be further explored in Articles (1.3.2, 1.3.3, and 2.2).

1.3.2 Starting—A Key Issue

It is an interesting feature of aerodynamics that sometimes two distinctly different steady state flows are possible for the same (free-stream and boundary) conditions. Generally, flows with such phenomena involve a dependence on initial conditions and/or a two-way change in boundary conditions. Classical examples of this include some form of hysteresis, such as in: 1) stall angle of a wing and 2) Mach number for transition between regular to Mach reflection and back. Such is also the case for all practical inlets operating in the supersonic (and hypersonic) regime,

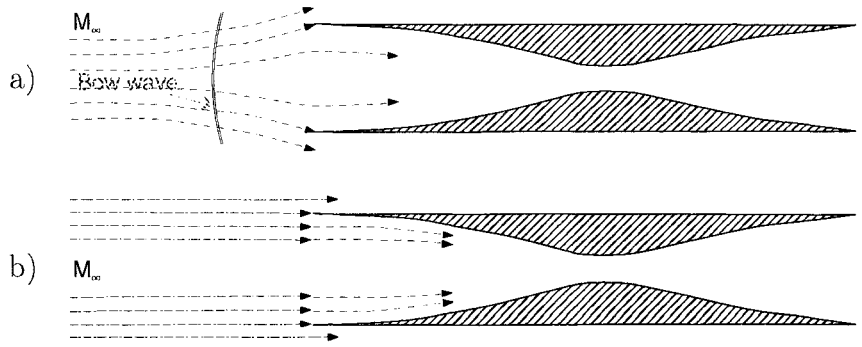

Figure 1.6: Two possible modes of operation at the same free stream condition: a) an unstarted inlet; b) a started inlet.

in that two modes of flow (*Started* and *Unstarted*) are possible.

Figure 1.6 shows these two modes in a quasi-one-dimensional, converging-diverging section. Although theoretical considerations will be examined in Article 2.2, for the sake of introduction in this chapter, a brief note will suffice—generally speaking, for inlets of practical interest, started flow is not easily established, and once established, unstarted flow is highly undesired.

1.3.3 Current Applications

As hinted earlier (Article 1.3.1), for both planar and spike inlets, it is relatively easy to establish steady started flow. Indeed, two well-known applications of such inlets include the British Concorde and the USAF Blackbird (SR-71), respectively. In Article 2.2, the fundamentals of inlet-starting are discussed, and it is clear that geometries, which are inherently easy to vary from a structural and mechanical point of view, are also the easiest to start. For the case of a simple planar inlet, a flap or hinged door can be used to vary the area ratio during the starting process. For the case of unstarted spike-inlets, large amount of spillage occurs, and a natural mechanism exists permitting flow-starting.

1.4 Brief Review of Literature

In the post-war (WWII) era (1940s and 1950s), a need was felt for supersonic fighter aircraft. A lot of studies were carried out by NACA (National Advisory Committee for Aeronautics—predecessor to NASA), and a major effort was devoted to examine perforated diffusers[†]. References [19], [22], and [24] describe this work. In particular, the work of Kantrowitz [10] and Donaldson [11], led to the establishment of a criterion for *quasi-steady starting*, and their supersonic diffusers were designed to automatically meet this criterion at design conditions. In an exploratory study, Evvard and Blakey [5] employed perforations to extend the range of operation and to enable starting of diffusers beyond Kantrowitz' limit. Hunczak and Kremzier [8] continued the aforementioned investigation (also at NACA) to study shock stability for subsonic combustors. During the late 1950s and early 1960s, Brown, Clark [4] and Wu [35] (in chronological order), performed experimental tests on a two-dimensional perforated diffuser based on a reversed de Laval nozzle designed for Mach number of 2.5. At the time of these studies, emphasis was placed on stabilisation of shock for subsonic combustion and also perforations were to remain open even after the starting process had come to completion; Clark's work will be described in some detail in Article 4.2.4.3.

It should be pointed out that there is no known literature, numerical or otherwise, describing the unsteady starting methods, as studied in the present work. The hiatus in the reported work in this field is due likely, not to a lack of interest in this field, but to the classification of work done by military organisations, and also due to the sensitivity of information for national security and its strategic military value. Indeed, much of the above reference material was once classified!

[†]Another common term used to describe supersonic air inlets.

1.5 Overview

1.5.1 Purpose

The purpose of this research is to numerically investigate methods of establishing steady, started flow in supersonic and hypersonic air inlets (no experimental work has been carried out). The proposed methods (of inlet starting) are in themselves not restricted to be of a quasi-steady nature—but once these methods are applied, the end result should be steady started operation. The starting problem is approached mostly from an academic point of view, without delving into the practicality, and without performing feasibility studies.

1.5.2 Outline

The remainder of the document is organised as follows. Chapter 2 outlines some of the theoretical considerations for establishing started flow in a hypersonic air inlet; the aim is to review quasi-steady flows and to lay the ground-work for discussion of results in Chapter 4. An exploratory study has been performed to highlight some promising techniques for inlet starting. Chapter 3 describes the mathematical model and the numerical technique used to obtain the high-resolution solutions presented in this thesis. Additionally, some test cases are presented for verification purposes. Chapter 5 presents a brief summary of the work.

1.6 Software

Research work reported in Ch. 4 was largely produced using `SolverII` [27]. Some of the other major tools used in the production of this work that are worthy of mention include: `UGG` [31], `Viewer` [26], `Mayura draw` [15] and `gnuplot` [34].

Finally, typesetting for this dissertation was performed using LaTeX 2_ε; a template class is available upon request.

A detailed description of the above-mentioned codes is not within the scope of present discussion. The author is intimately aware of the effort that goes into the development and debugging of useful software, and hence, he feels it fit to name these products as a gesture of acknowledgment towards the respective developers. At the same time, this also makes it possible for the interested reader to obtain further information about the software used in the production of this work.

Chapter 2

Theory

2.1 Background

To gain a basic insight into the starting and unstarting phenomenon associated with supersonic air inlets, let us review the quasi-steady, quasi-one-dimensional model of an inlet (with Fig. 2.1 in mind). This model describes the flow as a function of one spatial dimension (x) only, while accounting for area variation, $A = A(x)$; the other two spatial dimensions (y, z) and the temporal variation are neglected, *i.e.*, $u = u(x)$. Conservation laws for mass, momentum and energy, along with a state relation can then be used to describe the simple flow in an arbitrary stream tube, so long as the assumptions of uniform density and velocity

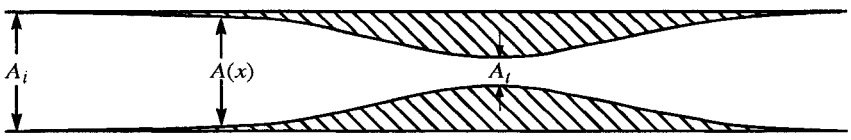

Figure 2.1: Geometrical model of an inlet.

across any section of the stream tube remain valid.

In the present context, air is modelled as a calorically perfect gas. Additionally, thermal and viscous dissipation effects are not accounted for. Fortunately, this greatly simplified analysis still retains the essential features of *quasi-steady* starting phenomena; this fact will become clear with further discussion in Articles 4.2.1 and 4.2.2.

2.1.1 Nomenclature

For the remainder of this chapter, in the context of inlet geometries, subscripts (i, t, and e) signify inlet, throat, and exit planes, respectively. These subscripts are reserved for area $A(x)$, Mach number $M(x)$, and mass flow $\dot{m}(x)$, exclusively. The rest of the symbols and corresponding flow properties are: $\rho(x)$ for density, $u(x)$ for velocity, $p(x)$ for pressure, and $T(x)$ for temperature. In this context, subscript t always refers to the total or stagnation condition. In addition, R is the gas constant, c the signal velocity, and γ the polytropic index; ($\gamma = 7/5$, for air). Let us now review some of the fundamental relationships between local flow area and the average flow properties at a cross-section.

2.1.2 Area-Velocity Relation

Flow parameters often show a dual-natured relationship with Mach number. To further motivate this point, the area-velocity relation needs to be explained first. Conservation of mass states, $\frac{d}{dx}(\rho u A) = 0$, expanding and rearranging one obtains [13]:

$$\frac{d\rho}{\rho} + \frac{du}{u} + \frac{dA}{A} = 0 \tag{2.1}$$

Similarly, conservation of momentum states that for unit mass: $a_x = u\frac{du}{dx} = f_x$, where a_x is the acceleration experienced by a fluid element and f_x is the pressure force acting on a unit of mass in that element [13]. For an arbitrary control volume, the total pressure force along x-coordinate is (*ibid.*): $-\frac{\partial p}{\partial x}(\Delta x A)$; dividing the latter by mass contained in the fluid element $\rho \Delta x A$, one obtains the force per unit mass, $f_x = -\frac{1}{\rho}\frac{\partial p}{\partial x}$, and equating acceleration to force per unit mass one gets, $u\frac{du}{dx} = -\frac{1}{\rho}\frac{dp}{dx}$, or,

$$udu + \frac{dp}{\rho} = 0 \tag{2.2}$$

This is called *Euler's equation*. Using the chain rule for the second term in this equation, $\frac{dp}{\rho} = \frac{dp}{d\rho}\frac{d\rho}{\rho}$ and introducing the square of the signal velocity $c^2 = \left(\frac{\partial p}{\partial \rho}\right)_s$ [9], $\frac{dp}{\rho} = c^2\frac{d\rho}{\rho}$, one obtains the *density-velocity relation*:

$$\frac{d\rho}{\rho} = -M^2\frac{du}{u} \tag{2.3}$$

Substituting Eq. (2.3) in Eq. (2.1) results in the classical *area-velocity relation*:

$$\frac{du}{u} = \frac{1}{M^2 - 1}\frac{dA}{A} \tag{2.4}$$

It is clear from the area-velocity relation that at small subsonic values (incompressible flow, $M << 1$), a decrease in area causes a proportionate increase in velocity. For higher subsonic values (compressible flow), the same trend holds, and decreasing area results in increasing velocity. At supersonic velocities, the $(M^2 - 1)$ term switches sign, so that a decrease in area results in decrease in velocity. Alternatively, from Eq. (2.3), it is evident that density decreases faster than velocity increases, so that area must increase to conserve mass [13]. Lastly, it is apparent that when $(M = 1)$, for (du/u) to remain finite and continuous,

(dA/A) must be zero, *i.e.*, $(M = 1)$ can be attained only at a throat! If the throat flow is not sonic, then (du/u) must be zero from Eq. (2.4)—that is, the velocity reaches a minimum or a maximum at the throat, depending on whether the flow is supersonic or subsonic.

2.1.3 Choking

Mass flux $\left(\frac{\dot{m}}{A}\right)$ can be formulated as a function of local Mach number and total conditions in the flow. For a given set of total conditions, the maximum mass flow per unit area occurs when the local Mach number reaches unity. The area is a minimum at the throat, and sonic conditions $(M = 1)$ can occur only at the throat; when these conditions are met, the flow is said to be choked—no more mass can be ingested. In other words, for a given set of stagnation conditions, the mass flux has an upper limit, which is reached at the throat. For the model inlet in Fig. 2.1, $\dot{m} = (\rho u A)$; using the standard equation of state $(p = \rho RT)$, and definition of Mach number $M = u/c$, with $c = \sqrt{\gamma RT}$, one obtains:

$$\dot{m} = \frac{p}{RT} M \sqrt{\gamma RT} A \tag{2.5}$$

From definitions of constant pressure specific heat $(c_p = \frac{dh}{dT})$, and total enthalpy $h_t = h + u^2/2$, and relating $(c_p = \gamma R/(\gamma - 1))$, one obtains: $T_t = f(T, \gamma, M)$. For details of these derivations, see [9].

$$T_t = T\left(1 + \frac{\gamma - 1}{2} M^2\right) \tag{2.6}$$

With isentropic flow relation $\frac{p_t}{p} = \left(\frac{T_t}{T}\right)^{\gamma/(\gamma-1)}$, one obtains $p_t = f(p, \gamma, M)$.

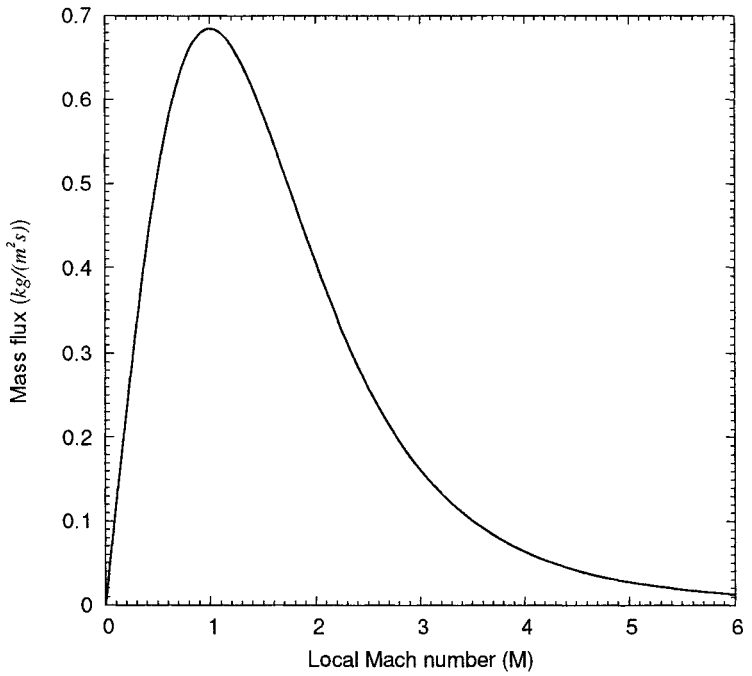

Figure 2.2: Mass flow per unit area, as a function of Mach number.

$$p_t = p\left(1 + \frac{\gamma - 1}{2}M^2\right)^{\gamma/(\gamma-1)} \tag{2.7}$$

Replacing (p, T) in Eq. (2.5) with (p_t, T_t) from Eq. (2.6) and Eq. (2.7), one obtains an expression for the mass flux, $\frac{\dot{m}}{A} = \frac{p_t}{\sqrt{RT_t}} f(\gamma, M)$:

$$\frac{\dot{m}}{A} = p_t\sqrt{\frac{\gamma}{RT_t}}M\left(1 + \frac{\gamma - 1}{2}M^2\right)^{-\frac{1}{2}\frac{\gamma+1}{\gamma-1}} \tag{2.8}$$

A plot of the result of Eq. (2.8) is shown in Fig. 2.2, and it is clear that for a *given set of total conditions*, the maximum value occurs at $(M = 1)$. Thus, the maximum ingestible air mass during the starting process is equal to that which will pass through the minimum area (A_t), while the flow is choked $(M_t = 1)$.

2.1.4 Limit on Steady, Started Operation

Recall from the previous section that the maximum area reduction permitted for an isentropic process occurs when the local Mach number reaches unity. For steady flow conditions, using Eq. (2.8) to relate conservation of mass between two arbitrary states results in:

$$\frac{A_2}{A_1} = \frac{p_{t1}}{p_{t2}}\sqrt{\frac{T_{t2}}{T_{t1}}}\frac{M_1}{M_2}\left[\frac{\left(1+\frac{\gamma-1}{2}M_1^2\right)}{\left(1+\frac{\gamma-1}{2}M_2^2\right)}\right]^{-\frac{1}{2}\frac{\gamma+1}{\gamma-1}} \tag{2.9}$$

Simplifying, this relates conservation of mass between entrance and throat, thus one obtains the minimum (isentropic) area ratio required for flow choking ($M = 1$) at the throat:

$$\frac{A_s}{A_\infty} = M_\infty\left[\frac{1+\frac{\gamma-1}{2}M_\infty^2}{1+\frac{\gamma-1}{2}}\right]^{-\frac{1}{2}\frac{\gamma+1}{\gamma-1}} \tag{2.10}$$

For supersonic inlets, *this result demonstrates the maximum area contraction permitted for steady, started operation* (plotted in Fig. 2.3, and compared with results in Article 4.2.2).

2.1.5 Limit on Quasi-Steady Flow-Starting

There exists a critical contraction ratio for a given value of free stream Mach number at which a previously unstarted inlet naturally switches to started mode. For all converging sections (strictly speaking, supersonic inlets of practical interest), flow choking occurs as the design Mach number is approached (accelerating from subsonic values). This prevents spontaneous starting and a bow wave forms to accommodate spillage of mass not ingestible by the throat under free stream total conditions; *cf.* Fig. 2.4e and Fig. 2.3, with $\left(\frac{A_t}{A_i} = \frac{A_t}{A_\infty}\right)_{M_S}$. If the flow aft of this

bow shock is assumed to be isentropic, then one simply replaces M_∞ in Eq. (2.10) with Mach number M_2 behind the shock [†], thus yielding another limiting contraction commonly known as Kantrowitz' relation:

$$\frac{A_t}{A_\infty} = M_2 \left[\frac{1 + \frac{\gamma-1}{2} M_2^2}{1 + \frac{\gamma-1}{2}} \right]^{-\frac{1}{2}\frac{\gamma+1}{\gamma-1}} \tag{2.11}$$

with,

$$M_2 = \sqrt{\frac{\frac{2}{\gamma-1} + {M_1}^2}{\frac{2}{\gamma-1}\gamma {M_1}^2 - 1}} \tag{2.12}$$

where, $M_1 = M_\infty$, *i.e.*, the Mach number in front of the bow shock. For supersonic inlets, *this result demonstrates the maximum area contraction permitted for spontaneous starting under quasi-steady flow conditions* (plotted in Fig. 2.3, and compared with results in Article 4.2.1). This criterion generally holds well (Article 4.2.1) even for multi-dimensional inlets because the quasi-steady starting process is usually one dimensional. The reader will note that Kantrowitz' area ratio has an asymptote at hypersonic values of Mach number, so that for $\gamma = 7/5$, A_t/A_∞ tends to ~ 0.6 as $M_\infty \to \infty$ (*vide* Fig. 2.3). The significance of this fact will become clear with further discussion in Article 2.2.1.

2.2 The Starting Process

Establishment of supersonic flow in a fixed geometry, converging section always requires swallowing of a bow shock. Figure 2.3 shows one possible way of achieving steady-started flow in low contraction, fixed geometry air inlets. The principles

[†] $M_2 = f(\gamma, M_1)$ can be obtained by applying conservation of mass, momentum and energy across the shock (pg. 70 ref. [9]). Clearly, in Eq. (2.12), $M_1 = M_\infty$, *i.e.*, the Mach number in front of the bow shock.

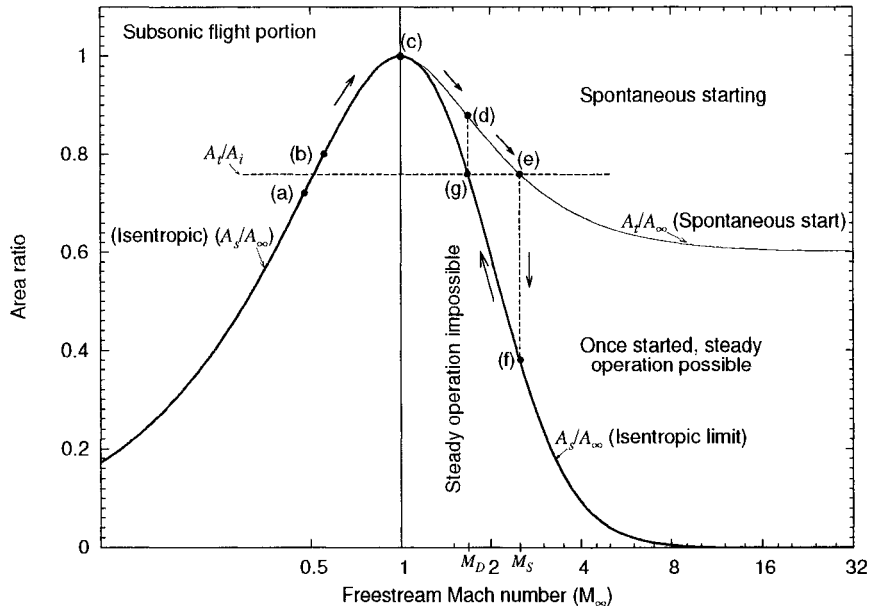

Figure 2.3: An illustration of starting by over-speeding. Perfect gas, $\gamma = 7/5$.

outlined below (Article 2.2.1) hold in general, however, for all inlets; this fact warrants a detailed discussion of the *starting phenomenon* that is involved in the over-speeding procedure.

2.2.1 Over-Speeding

Figure 2.4 summarises the *corresponding flow configurations* labelled in Fig. 2.3 and illustrates successive steps in the over-speeding procedure [9]. Table 2.1 lists the local Mach number at various stations as the inlet is first accelerated from low subsonic values (a) to the design Mach number M_D (d), and then over-sped to starting Mach number M_S (e,f) before finally being slowed back to the design conditions (g).

Configuration (a) describes the initial phase of acceleration where $M_t < 1$ so that the mass flow and hence the capture area A_∞ depend entirely on conditions

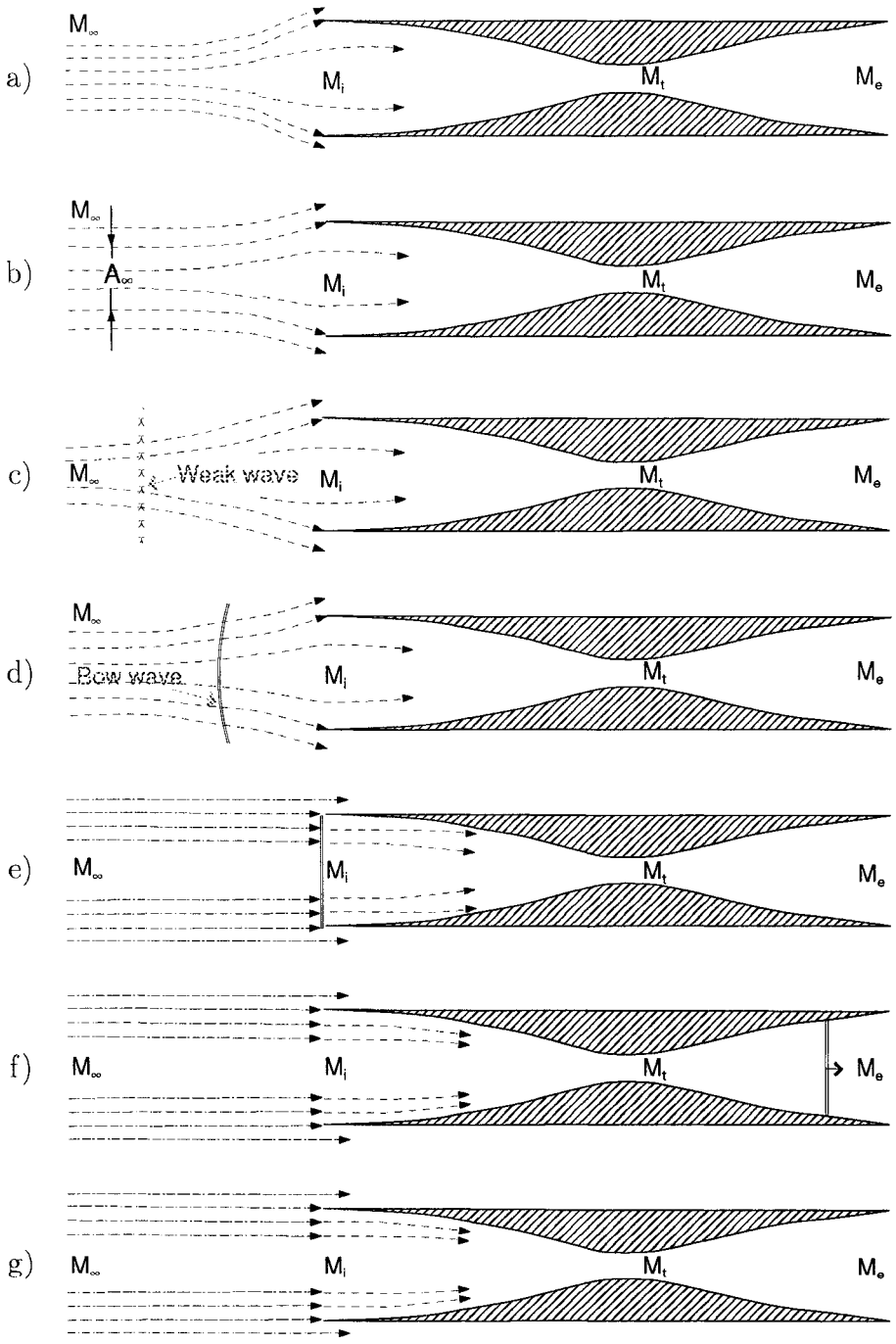

Figure 2.4: Starting schedule (a-g), showing basic flow stages during the starting process.

	M_∞	M_i	M_t	M_e
a	< 1	< 1	< 1	< 1
b	< 1	< 1	$= 1$	< 1
c	$= 1$	< 1	$= 1$	< 1
d	> 1	< 1	$= 1$	< 1
e	M_S-	< 1	$= 1$	< 1
f	M_S+	> 1	> 1	< 1
g	M_D	> 1	$= 1$	< 1

Table 2.1: Flow regime at each station during starting (*vide* Figs. 2.3 and 2.4)

downstream of the inlet. As the free stream Mach number is increased to a higher subsonic value, throat Mach number reaches unity and flow choking takes place. Under these conditions (b), the capture area A_∞ is given by Eq. (2.10) with $A_s = A_t$ and $A_i > A_\infty$ (Fig. 2.3). Further increasing the free stream Mach number to the sonic value causes a weak wave to form (c) and $A_s/A_\infty = 1$, so that with $A_s = A_t$, the capture area equals the throat area. Further increase in free stream Mach number leads to the appearance of a bow-wave (d).

In supersonic flight, the presence of an inlet can not be detected in the free stream because signals cannot travel upstream. Since the throat remains choked, a bow wave must form to provide a mechanism for continued spillage with subsonic flow immediately ahead of the inlet. The shock stand-off distance is compatible with the amount of spillage required. There is an increase in entropy and loss in total pressure across the shock, causing lowered mass flow through the throat, as stated by Eq. (2.8). The capture area is then governed by Eq. (2.11) as indicated by A_t/A_∞ in Fig. 2.3. *Thus, $A_i > A_\infty$ and the inlet does not start at the design Mach number.*

To permit shock swallowing, the inlet must be accelerated to M_S (Fig. 2.3), whereby A_t/A_∞ intersects A_t/A_i. A stable shock-configuration can not be established in a converging section, so that once $A_\infty = A_i$, the inlet starts spontaneously

(e) as described in Article 2.1.5. Once the shock is fully swallowed (f), the Mach number may be gently lowered back to the design conditions (g). The reader will note that for medium and high contraction inlets, ($A_t/A_i < 0.6$) and it can not intersect A_t/A_∞ at any value of free stream Mach number. *This fact reflects the limit on area ratio for inlets that may be started using the over-speeding process.*

2.2.2 Popular Methods

Though over-speeding is a simple and effective method, unfortunately all by itself, its application is limited to low contraction inlets only. Other measures must be taken to start high contraction[†] air inlets of interest in ramjet and scramjet applications. Generally speaking, these additional measures only aim to relax the limit on A_t/A_∞, while the basics of the starting procedure remain unchanged. For instance, it is inherently easier to employ variable geometry in planar inlets, and starting can be promoted by varying A_t/A_i; that is to say, it is possible to avoid formation of the bow shock by varying A_t/A_i in such a way that it never drops below the A_s/A_∞ curve. Inlets based on scoop-like geometries have different effective values of A_t/A_i in the started and un-started mode because overboard spillage is possible even after the shock travels past the entrance plane. The same spillage mechanism, compounded with translating centre bodies, also makes it possible to establish started flow in spike-inlets.

2.2.3 Slits

Another method used to attain started flow is to perforate the diffuser walls, thereby allowing enough flow spillage for the inlet to start at a desired Mach

[†]For $\gamma = 7/5$, A_t/A_∞ tends to ~ 0.6 as $M \to \infty$.

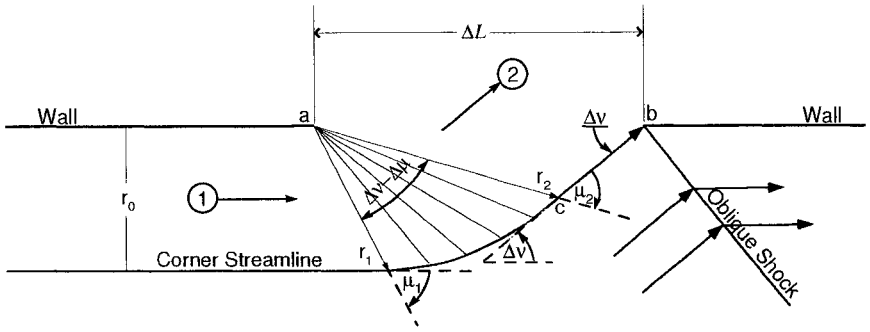

Figure 2.5: Perforation model based on Prandtl-Meyer flow.

number. As mentioned earlier (Article 1.4), inlet starting by way of wall perforations was popularised by Evvard and Blakey [5]. Here, a simple expression for spillage through a slit-like perforation is derived, and the analytical results obtained† below will be compared with numerical results presented in Article 4.2.4. The general idea here is to highlight the trends and important parameters affecting mass flow across a perforation.

Referring to Fig. 2.5, let us consider a transverse slit *ab*, in the wall, through which some flow spillage takes place. In this figure, μ represents the local Mach angle, and $\Delta\nu = \nu(M_2) - \nu(M_1)$ is the flow deflection determined using the classical Prandtl-Meyer function [13]. The flow captured by the slit undergoes an isentropic process between states ① and ②. Under these conditions, Eq. (2.9) can be used to relate the captured flow areas A_1, and the spillage area A_2, simplifying, one obtains:

$$\frac{A_2}{A_1} = \frac{M_1}{M_2}\left(\frac{1+\frac{\gamma-1}{2}{M_1}^2}{1+\frac{\gamma-1}{2}{M_2}^2}\right)^{-\frac{1}{2}\frac{\gamma+1}{\gamma-1}} \tag{2.13}$$

In the strictest sense, this flow is representative of planar geometries only, although in practice axially symmetric slits may also be approximately analysed this

†Suggested by Prof. Mölder.

way—so long as the flow remains locally planar. Clearly, appropriate expressions for areas (A_i) must be used depending on the local geometry being considered.

The general idea here is to highlight the trends and important parameters affecting mass flow across the slit. To this end, it is instructive to plot mass-flow as a function of external pressure (outside the inlet), for various internal values of Mach number near the slit leading edge (M_1). For a unit depth (Δz into the page), we have, $A_1 = r_0 \Delta z$, but from geometry, $r_0 = r_1 \sin\mu_1 = r_1 \frac{1}{M_1}$, so that $A_1 = r_1 \frac{1}{M_1} \Delta z$. Substituting a similar expression for area A_2, in Eq. (2.13), one gets:

$$\frac{r_2}{r_1} = \left(\frac{1 + \frac{\gamma-1}{2} {M_1}^2}{1 + \frac{\gamma-1}{2} {M_2}^2} \right)^{-\frac{1}{2}\frac{\gamma+1}{\gamma-1}} \tag{2.14}$$

Applying sine-law to $\triangle abc$ in Fig. 2.5, $\frac{|r_2|}{\sin\Delta\nu} = \frac{|\Delta L|}{\sin(\pi-\mu_2)}$, and substituting for μ_2 yields, $\Delta L = f(r_2,\, M_2,\, \Delta\nu) = \frac{r_2}{M_2 \sin\Delta\nu}$. The ratio of captured height (r_0) to spillage width (ΔL) is an indicator of the overall efficacy of the slit; simplifying, one gets:

$$\frac{r_0}{\Delta L} = \frac{r_1}{r_2} \frac{M_2}{M_1} \sin\Delta\nu \tag{2.15}$$

Equation (2.15) can be plotted for various values of approach Mach number M_1 (at slit leading), against the slit pressure ratio p_2/p_1. Additionally, using Eq. (2.6), $M_2 = f(M_1,\, p_2/p_1)$ can be obtained (because total pressure is constant for an isentropic process), and the result can be substituted in Eq. (2.14). Thus, $r_0/\Delta L = f(M_1,\, p_2/p_1)$ is plotted in Fig. 2.6, and it is clear, at each value of M_1, there exists a maximum value of $r_0/\Delta L$. The absolute maximum occurs for a slit with a sonic leading edge, whereas for higher values of M_1 the value is significantly reduced. This value occurs when the normal component of Mach number

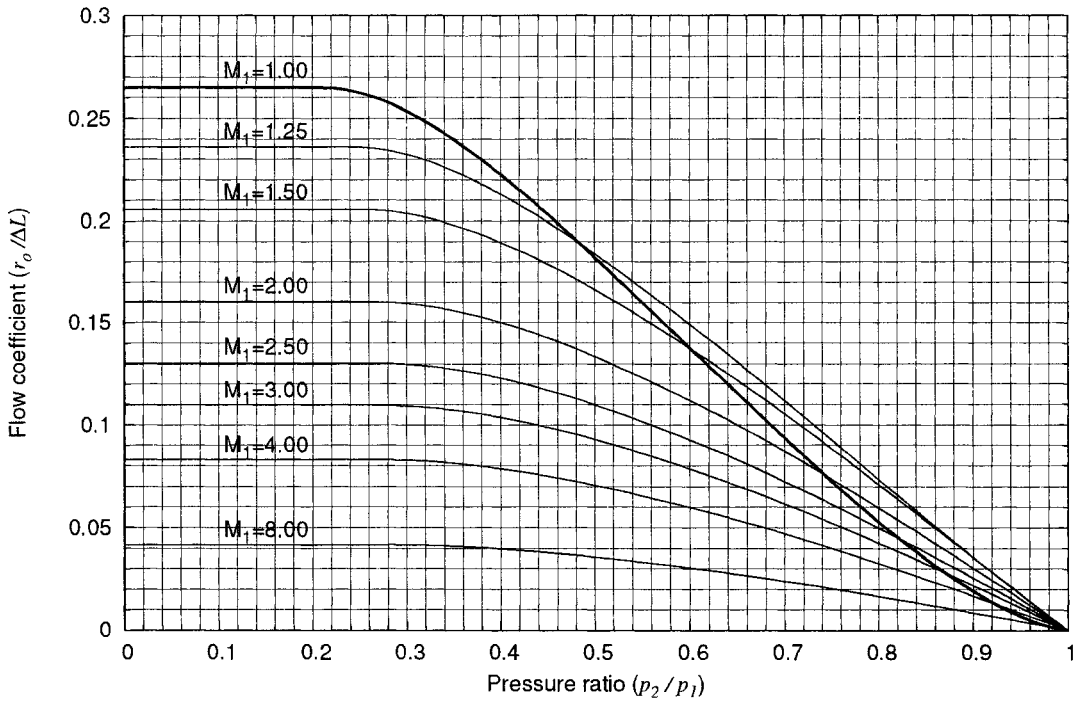

Figure 2.6: Mass flow coefficient for a slit-like perforation, as a function of external to internal pressure ratio, at various values of approach Mach number at the slit leading edge. Perfect gas, $\gamma = 7/5$.

at the slit reaches unity, *i.e.*, locally, the flow becomes choked. Under these conditions (as the critical pressure ratio is reached), rays of the expansion fan approach the wall; further lowering the external pressure (beyond the critical value) is not beneficial.

2.3 Busemann Flow

As indicated earlier (Article 1.3), there exists a class of internal compression inlets based on a conically symmetric flow; this flow was first postulated in the post WWII era by Adolf Busemann [3]. Beginning with an infinitesimal-strength wave in the uniform free stream, it undergoes isentropic compression and is terminated

by a finite-strength wave resulting in uniform outflow (*vide* Fig. 2.7). Design methodologies for efficient, two and three-dimensional, Busemann-based inlets for hypersonic application have already been popularised by various researchers in the 1960s and '70s [16], [18], and [32]. Busemann flow offers tremendous flexibility to an inlet designer in that even non-axisymmetric versions of Busemann-based, modular, streamline-traced, efficient and aesthetically pleasing geometries can be generated. From a geometrical point of view, Busemann inlets provide a logical basis for the present work (see Article 1.3.1).

2.3.1 Basic Busemann Inlet

In Fig. 2.7, compression is initiated at the high Mach number (free stream) and terminated at the exit Mach number by a shock; the isentropic portion is bounded on the upstream by a Mach cone and on the downstream by a shock cone. The flow is irrotational, conically and axially symmetric and is described analytically in polar coordinates (r, θ), by the classical Taylor-Maccoll equation [12]:

$$0 = \hat{u}_\theta - \frac{\partial \hat{u}_r}{\partial \theta}$$

$$0 = \frac{\gamma - 1}{2}\left[1 - \hat{u}_r^2 - \left(\frac{\partial \hat{u}_r}{\partial \theta}\right)^2\right]\left[2\hat{u}_r + \frac{\partial \hat{u}_r}{\partial \theta}\cot\theta + \frac{\partial^2 \hat{u}_r}{\partial \theta^2}\right] - \left(\frac{\partial \hat{u}_r}{\partial \theta}\right)^2\left[\hat{u}_r + \frac{\partial^2 \hat{u}_r}{\partial \theta^2}\right] \tag{2.16}$$

where the velocity u has been nondimensionalised, so that $\hat{u} = \frac{u}{u_{max}}$, with $u_{max} = u\sqrt{\frac{2}{(\gamma-1)M^2} + 1}$. The most well-known numerical integration of this equation is for the flow over an axisymmetric cone at zero angle of attack in supersonic flow. Mathematically, a more elegant form of the Taylor-Maccoll equation was recently obtained by Mölder [28], recasting it in terms of the radial and azimuthal

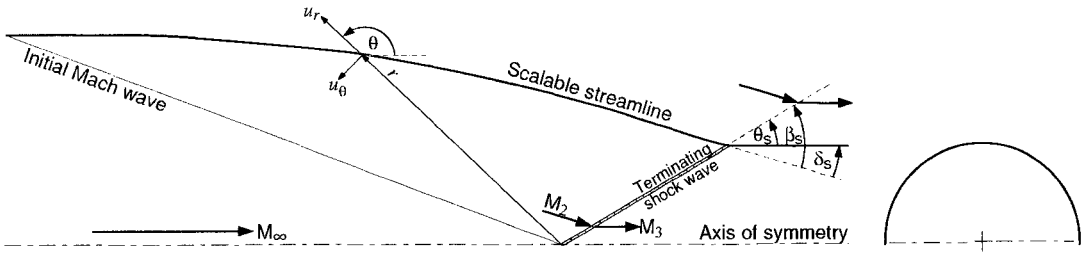

Figure 2.7: Flow geometry in a (basic) Busemann inlet.

Mach numbers (M_r, M_θ).

$$\frac{d}{d\theta}M_r = M_\theta + \left(\frac{\gamma-1}{2}M_r M_\theta\right)\left[\frac{M_r + M_\theta \cot\theta}{M_\theta^2 - 1}\right] \tag{2.17a}$$

$$\frac{d}{d\theta}M_\theta = -M_r + \left(1 + \frac{\gamma-1}{2}M_\theta^2\right)\left[\frac{M_r + M_\theta \cot\theta}{M_\theta^2 - 1}\right] \tag{2.17b}$$

The Taylor-Maccoll equation, written above as a set of two, first-order, coupled, non-linear Ordinary Differential Equation(s) (ODE), forms an initial value problem, amenable to numerical integration. These equations are used in the solution method below.

2.3.2 Solution Method

For the Busemann inlet, streamline and characteristics integration can be conveniently included the in the solution process.

$$\begin{aligned}\vec{u} &= \begin{bmatrix} M_r & M_\theta & r & x_\beta & y_\beta \end{bmatrix}^T \\ &= \begin{bmatrix} u_1 & u_2 & u_3 & u_4 & u_5 \end{bmatrix}^T \end{aligned} \tag{2.18a}$$

where, u_1-radial Mach number, u_2-azimuthal Mach number, u_3-radial location, u_4 and u_5-location in cartesian coordinates along the C^- characteristic. θ-derivatives

for above variables in Eq. (2.18a) [28], may be written in vector form as:

$$\begin{aligned}\vec{u}' &= \begin{bmatrix} M_r' & M_\theta' & r' & x_\beta' & y_\beta' \end{bmatrix}^T \\ &= \begin{bmatrix} M_\theta + \left(\frac{\gamma-1}{2} M_r M_\theta\right)\left[\frac{M_r + M_\theta \cot\theta}{M_\theta^2 - 1}\right] \\ -M_r + \left(1 + \frac{\gamma-1}{2} M_\theta^2\right)\left[\frac{M_r + M_\theta \cot\theta}{M_\theta^2 - 1}\right] \\ r\frac{M_r}{M_\theta} \\ r\cos(\delta - \mu) / \cos(\pi/2 - \delta + \mu) \\ r\sin(\delta - \mu) / \cos(\pi/2 - \delta + \mu) \end{bmatrix} \\ &= \begin{bmatrix} F_1 & F_2 & F_3 & F_4 & F_5 \end{bmatrix}^T \end{aligned} \tag{2.18b}$$

where, δ is the local flow deflection given by:

$$\delta(\vec{u},\, \theta) = \arctan\left(\frac{u_1 \sin\theta + u_2 \cos\theta}{u_1 \cos\theta - u_2 \sin\theta}\right),$$

and μ is the local Mach angle is obtained using:

$$\mu(\vec{u},\, \theta) = \arcsin\left[\left(u_1^2 + u_2^2\right)^{-\frac{1}{2}}\right].$$

Equation (2.18b) can now be written in the general form of a nonlinear ODE, $\frac{d\vec{u}}{dt} = \vec{F}(\vec{u}, t)$, giving:

$$\vec{u}' = \vec{F}(\vec{u}, \theta) = \begin{bmatrix} u_2 + \left(\frac{\gamma-1}{2} u_1 u_2\right)\left[\frac{u_1 + u_2 \cot\theta}{u_2^2 - 1}\right] \\ -u_1 + \left(1 + \frac{\gamma-1}{2} u_2^2\right)\left[\frac{u_1 + u_2 \cot\theta}{u_2^2 - 1}\right] \\ u_3 u_1 / u_2 \\ u_3 \cos(g_1) / \cos(\pi/2 - g_1) \\ u_3 \sin(g_1) / \cos(\pi/2 - g_1) \end{bmatrix} \tag{2.19}$$

where, $g_1 = \delta(\vec{u}, \theta) - \mu(\vec{u}, \theta)$. Using θ as a time like variable, Eq. (2.19) may be written as an Ordinary Difference Equation (OΔE) and integrated starting with, $\vec{u}_n = \vec{u}_0(\theta_s)$ at the conical shock, and marching in θ using $h = d\theta$ with $\vec{u}_{n+1} = \vec{u}_n + h\vec{u}'_n$. The stopping criterion is that flow becomes parallel to the free stream, *i.e.*, $\delta = 0$. A typical result of this method is shown in Fig. 2.8. Since the flow is conical, isolines for density, pressure, temperature and velocity all form perfect radials. Figure 2.9 shows contours of constant Mach number; this is used for verification purposes later in Article 3.4.3.

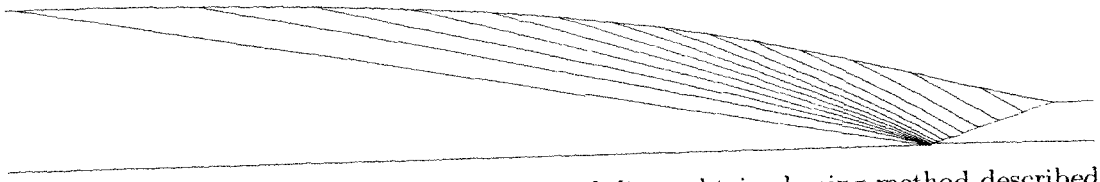

Figure 2.8: Busemann inlet contour and Mach lines obtained using method described in Article 2.3.2.

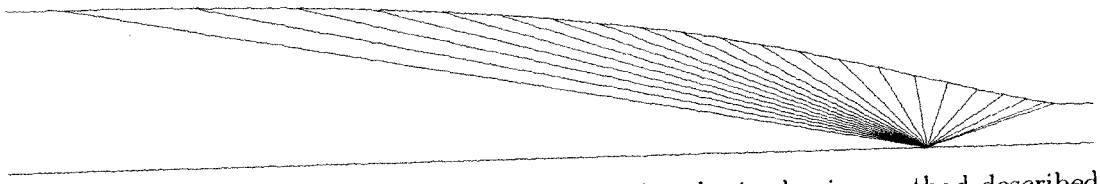

Figure 2.9: Iso-Mach contours in a Busemann inlet obtained using method described in Article 2.3.2.

Chapter 3

Numerical Modelling

3.1 Background

From a gasdynamics point of view, the inlet starting and unstarting processes often contain some very complex phenomena, which can lead to unsteady flows involving multiple shock waves, contact and slip surfaces, vortices, and boundary layers. The presence of such localised features leads to complex interactions among these flow structures, as well as to interaction with the inlet geometry. Generally, such problems can not be approached from an analytical point of view alone.

3.1.1 Motivation For Numerical Modelling

As outlined earlier in Article 1.5.2, this study has been performed with the aid of numerical tools only, and no experimental work has been carried out. For initial studies, such an approach is becoming increasingly popular, and some of the factors promoting this include: 1) the prohibitively high costs associated with the initial establishment of a hypersonic experimental facility; 2) the operating costs

of such a facility; 3) the manufacturing costs associated with (scaled) test models; 4) diagnostic issues and difficulties associated with flow visualisation of internal, non-planar flows (which take place in axisymmetric and modular geometries). Under these circumstances, capable Computational Fluid Dynamics (CFD) tools prove to be an effective and economical alternative. The aim of this chapter is to describe the numerical scheme used here, and also to verify the CFD tools employed herein.

3.2 Mathematical Model

In the broadest sense, the starting problem should be addressed with Navier-Stokes equations and circumstantial turbulence modelling. Such an approach is however, out of the scope of the present study. As a first effort in this study, the problem is approached mathematically from a slightly simpler set of equations (following the Eulerian gas model). The basic premise is, in the spirit of G. I. Taylor [33], that an ideal model should introduce the minimum amount of complexity while capturing the essence of the relevant physics. This simplification is justified as follows: Firstly, an initial study including some "simple" phenomena can lead to a fundamental understanding of the problem being studied, so that one can gradually include and study the secondary effects of more "complex" phenomena. Secondly, the flows being studied here are generally dominated by advective phenomena, and in this respect the most essential features of the starting problem are well-represented in the inviscid framework; this is true with the proviso that the flow is not dominated by large separation zones. This concludes the basis for the selection of mathematical model.

3.2.1 Governing Equations

As motivated above, the present discussion is restricted to an inviscid gas model: conservation laws for mass, momentum and energy written in an integral form underlie the mathematical model. The governing equation relates the vector of conserved quantities $\mathbf{U}$, and its convective flux per unit area per unit time $\mathbf{F}$, for volume of gas Ω, bounded by a closed surface $\mathrm{d}\Omega$, with normal $\mathbf{n}$ pointing outwards:

$$\int_{\Omega} \mathbf{U}\,\mathrm{d}\Omega\Big|_{t_0}^{t} + \int_{t_0}^{t} \oint_{\mathrm{d}\Omega} \mathbf{F}\cdot\mathbf{n}\,\mathrm{d}s\,\mathrm{d}t = \int_{t_0}^{t} \mathbf{H}\,\mathrm{d}t \tag{3.1}$$

with,

$$\mathbf{U} = \begin{bmatrix} \rho \\ \rho u_i \\ e \end{bmatrix}, \quad \mathbf{F}^j = \begin{bmatrix} \rho u_j \\ \rho u_i u_j + p\,\delta_{ij} \\ u_j\,(e+p) \end{bmatrix}, \quad \mathbf{H} = \mathbf{H_1} + \mathbf{H_2}\ ,$$

where,

$$\mathbf{H_1} = \begin{bmatrix} 0 \\ \alpha\delta_{i2}\overline{p}\oint_{\mathrm{d}\Omega} n_i\,\mathrm{d}s \\ 0 \end{bmatrix}, \quad \mathbf{H_2} = \begin{bmatrix} 0 \\ \int_{\Omega} \rho a_i\,\mathrm{d}\Omega \\ \int_{\Omega} \rho u_i a_i\,\mathrm{d}\Omega \end{bmatrix}.$$

Here, ρ is the fluid density, p is the pressure, e is the total energy per unit volume, and u is the velocity vector. The total energy e is composed of kinetic energy per unit volume $\frac{1}{2}\rho u_j u_j$, as well as the internal energy per unit volume $\rho\,\epsilon$ (where ϵ is the internal energy per unit mass). δ_{ij} is the Kronecker symbol, and source vector $\mathbf{H_2}$ contains acceleration terms for computation in non-inertial frames of reference, while $\mathbf{H_1}$ incorporates the geometric source terms for computation with axisymmetric geometries. In this context, $\overline{p}$ is the average pressure in the control volume, obtained from conservative variables in $\mathbf{U}$. For axisymmetric geometries $\alpha = 1$, while $\alpha = 0$ corresponds to planar geometries. The system of equations

is closed mathematically by a state law, such as the perfect gas law, so that pressure is related to internal energy via, $p = (\gamma - 1)\left[e - \frac{1}{2}\rho u_j u_j\right]$, with a constant polytropic index γ. Acceleration in source terms is represented by a_i along coordinate-i. In all but a few cases (see Article 4.3), body forces are negligible so that $a_x = a_y = 0$.

3.3 Numerical Method

For highly unsteady flows, with fast moving shock waves, grid adaptation should be performed at each time step. The presence of large physical time scales (often exceeding 10 s in the present work) requires computationally efficient data structures and code implementation. A two-dimensional code based on these considerations was implemented (*ca.* 1993) by Voinovich [30], and has been successfully applied to a vast array of problems by various researchers [23] since. In recent years, a new version has been under development, based essentially on the above code, and under the product name `SolverII` by Tahir *et al.* [27]. The present study was carried out using `SolverII`, and for the sake of completeness, the particulars of this numerical tool are briefly described next. Conceptually, `SolverII` may be classified as a time accurate, locally-adaptive, multi-block, unstructured, quasi-monotone, finite-volume, Godunov-type code. It uses the Monotone Upwind Scheme for Conservation Laws (MUSCL) strategy for variable extrapolation, relies on Total Variation Diminishing (TVD) slope limiters to achieve monotonicity, employs an exact Riemann solver for flux differencing, and uses h-refinement[†] for mesh adaptivity.

[†]In the theory of CPDEs, h-refinement refers to local adaptation of the mesh by addition of vertices in areas where the error is expected to be large; r-refinement refers to movement of vertices for the same purpose, whereas p-refinement refers to adaptation of the order of the local basis function, which is used for solution approximation.

3.3.1 Discretization of Computational Domain

Among the prerequisites for a successful CFD simulation is the good approximation of the geometry under study. In this respect, even moderately complex geometries necessitate the use of unstructured meshes, and a good quality discretization of the computational domain is essential. To this end, an incremental triangulation is performed using `UGG` [31], yielding a boundary-fitted unstructured grid composed of triangular area elements. Non-overlapping control volumes are then formed about the primary grid nodes (vertex-centred scheme), where volume-averaged values of the dependent gas dynamic variables reside. In the solution process, the mesh is locally adapted; some further details will be presented in Article 3.3.5.

3.3.2 Reconstruction

High-resolution numerical schemes (with global accuracy of at least second-order) can be employed to easily achieve a desired level of accuracy in regions of smooth flow (*i.e.*, where the mesh is not refined), while spurious oscillation near flow discontinuities can be eliminated using TVD operators. To this end, piece-wise linear reconstruction of primitive variables stored in $\mathbf{V}$ is performed in the dual mesh (vertex-centred scheme), providing second order spatial accuracy.

The volume-averaged gradients at vertex i are first computed using its neighbours in the primary mesh (forming triangular elements) of sub-volumes Ω_e, with:

$$\left(\overline{\nabla \mathbf{V}}\right)_i \sum_e \Omega_e = \sum_e \left(\nabla \mathbf{V}\right)_e \Omega_e \tag{3.2}$$

where, $\sum_e \Omega_e = \Omega_i$. The mean gradients are then limited using a minmod-type

function:

$$\mathcal{L}\left(\nabla \mathbf{V}\right)_i = \underset{e}{\text{minmod}}\left[\left(\overline{\nabla \mathbf{V}}\right)_i, \beta\left(\nabla \mathbf{V}\right)_e\right] \tag{3.3}$$

with $\beta = 1.4$ for most problems. Reconstruction is performed using:

$$\mathbf{V}_{ij}^{\text{in}} = \mathbf{V}_i + \frac{1}{2}\mathcal{L}\left(\nabla \mathbf{V}\right)_i \cdot \overrightarrow{ij} \tag{3.4}$$

yielding a vector containing primitive variables at the inner side of the control volume surface s_{ij}, associated with volumes i, j.

3.3.3 Time Integration—Evolution and Projection

Time integration is performed using a predictor-corrector method due to Hancock, commonly known as the MUSCL-Hancock Method (MHM) [29]. It offers second order temporal and spatial accuracy. The predictor step does not involve a Riemann solver for flux computation, thus contributing to the computational efficiency of the method. After incorporating source terms into the standard MHM predictor step, one gets:

$$\tilde{\mathbf{U}}_i = \mathbf{U}_i^n - \frac{\Delta t}{\Omega_i}\left[\sum_j \left(\mathbf{F}\left(\mathbf{V}_{ij}^{\text{in}}\right) \cdot \mathbf{n}\, s_{ij} + \mathbf{H_1}\right) + \mathbf{H_2}\Omega_i\right] \tag{3.5}$$

The solution is then advanced to time level $(n+1)$ by a corrector step; incorporating the source terms, one obtains:

$$\mathbf{U}_i^{n+1} - \mathbf{U}_i^n = -\frac{\Delta t}{\Omega_i}\left[\sum_j \left(\mathbf{F}\left(\breve{\mathbf{W}}_{ij}\right) \cdot \mathbf{n}\, s_{ij} + \breve{\mathbf{H}}_{\mathbf{1}}\right) + \breve{\mathbf{H}}_{\mathbf{2}}\Omega_i\right] \tag{3.6}$$

Here, $\breve{\mathbf{W}}_{ij} = \mathit{Riemann}\left(\breve{\mathbf{V}}_{ij}^{\text{in}}, \breve{\mathbf{V}}_{ij}^{\text{out}}\right)$ is the vector of primitive variables obtained

from an exact, pressure-iterative Riemann solver, with left and right states corresponding to:

$$\check{\mathbf{V}}_{ij}^{\text{in}} = \frac{1}{2}\left(\mathbf{V}(\tilde{\mathbf{U}}_i) + \mathbf{V}(\mathbf{U}_i) + \mathcal{L}\left(\nabla\mathbf{V}\right)_i \cdot \overrightarrow{ij}\right) \tag{3.7}$$

$$\check{\mathbf{V}}_{ij}^{\text{out}} = \frac{1}{2}\left(\mathbf{V}(\tilde{\mathbf{U}}_j) + \mathbf{V}(\mathbf{U}_j) + \mathcal{L}\left(\nabla\mathbf{V}\right)_j \cdot \overrightarrow{ji}\right) \tag{3.8}$$

Source terms in Eqs. 3.5 and 3.6 are treated in a uniform (unsplit) manner at each time step. Source terms in the corrector step are obtained using:

$$\check{\mathbf{H}} = \frac{1}{2}\left(\mathbf{H}(\tilde{\mathbf{U}}) + \mathbf{H}(\mathbf{U})\right) \tag{3.9}$$

In this way, by using a consistent predictor-corrector procedure, globally second order temporal accuracy is achieved.

3.3.4 Riemann Solver

For all computations reported in Ch. 4, an exact pressure-iterative Riemann solver has been used. The interested reader is referred to literature for further details; for instance, a good treatise on Riemann solvers is provided by Toro [29].

3.3.5 Adaptive Meshing

Compressible flows (described by the Navier-Stokes and Euler equations) admit the presence of non-linear physical phenomena which can lead to the formation of shock waves and contact discontinuities. Under these circumstances, the fidelity of a numerical solution depends on the resolution of highly localised flow features. Computational efficiency can be increased by employing solution-adaptive mesh-refinement. The Adaptive Mesh Refinement (classical red-green h-refinement) (AMR) algorithm used in `SolverII` follows the procedure and rules outlined by

Löhner [14]. The refinement sensor is based on first and second-differences:

$$E_i = \max_j \left[\frac{\left| (\nabla U)_{\Omega_{ij}} - \overline{(\nabla U)}_i \right|}{\left| (\nabla U)_{\Omega_{ij}} \right| + \left| \overline{(\nabla U)}_i \right| + |U_i| \, \epsilon d^{-1}} \right] \tag{3.4}$$

Here, d is a local characteristic scale ("diameter" of cell i), ϵ is a filter coefficient (typically 1.5 for unit sized domain), and $U = U_1 = \rho$ is typically used in the sensor. This criterion is consistent with the hybrid formulation, in that the mesh is refined in locations where the local order of accuracy is reduced by the limiting operation. The local error measure E_i is compared with (user specified) threshold parameters for refinement and coarsening, T_r and T_c, respectively. Additionally, the existing refinement level m_i, in cell i is compared with the maximum and minimum permissible global values (also user-specified) and in conjunction with the error thresholds, this forms the basis for refinement and coarsening criteria. Mathematically, if $(E_i > T_r) \bigcap (m_{max} > m_i)$ then $h_i \leftarrow h_i/2$, *i.e.*, if the global refinement threshold value is smaller than the local value and the local refinement level is below the maximum permissible, then locally the mesh size is reduced in half. Similarly, if $(E_i < T_c) \bigcap (m_{min} < m_i)$ then $(h_i \leftarrow 2h_i)$. In the event of tied criteria, refinement supersedes coarsening. The standard refinement pattern leads to $h_{m+1} = h_m/2$, *i.e.*, compared to the basis mesh, with each additional level of refinement, the local mesh size reduces successively as $h_0/2^m$.

3.4 SolverII

3.4.1 Basic Features

The basic strategy adopted[†] here places emphasis on fully unstructured meshes that dynamically adapt to the solution. The local refinement and de-refinement is made automatic by detecting any moving or stationary discontinuities in the solution; this contributes towards achieving high computational efficiency. Formally, the method offers second order temporal and spatial accuracy in smooth-flow regions; in practice, the scheme is made hybrid with a TVD operator in order to reduce spurious oscillations and as a result, global order of accuracy is usually less than two. The general operation of `SolverII` is automated to a high degree and it requires minimal input from the user. To facilitate ease of use while retaining flexibility, a built-in parser is provided. For flow visualisation purposes, an integrated, Windows XP compliant post-processor is provided that is both fast and robust. A prototypical result was produced in less than one half-hour (including mesh generation, computation and post processing). Excellent qualitative agreement with the experimental result can be seen in Fig. 3.1, although only a minimal effort has been made to ensure quantitative validity of the comparison.

3.4.2 Computational Resources

Overall 43 words are reserved to store nodal data (including completely specified topology, no additional parent-child structures are used). The refinement algorithm is invoked at each time step with up to 5% of the total computational cost. The cost of the exact Riemann solver is approximately 10% of the total computa-

[†]Data structures designed by P.A. Voinovich, Supercomputer Centre at Ioffe Physico Technical Institute, Russian Academy of Sciences, St. Petersburg, Russia.

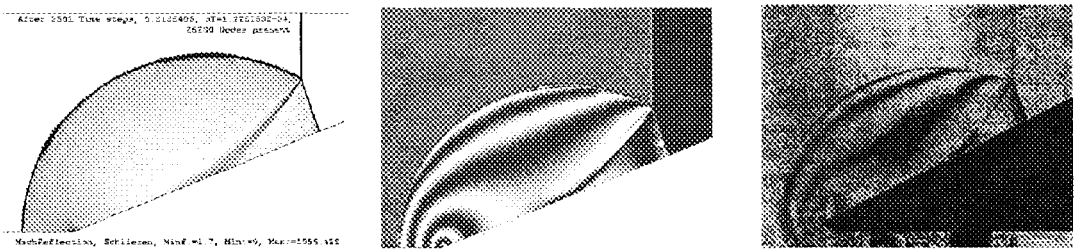

(a) (b) (c)

Figure 3.1: Mach reflection on a 25° wedge, $M_s = 1.7$—Comparison of figures from `SolverII` with experimentally produced holographic interferogram. (a) `SolverII` pseudo-schlieren; (b) `SolverII` numerical interferogram; (c) holographic interferogram (by Takayma *et al.*, SWRC, Tohoku University).

tional cost. The typical mesh size is $\mathcal{O}(10^3)$, requiring less than 4 MB of memory; in practice, usually 24 MB are requested from the operating system (including reserves for GUI). Approximately 75 000 nodes are processed per second on a 1 GFlop/s processor (Pentium*4* class machine, at the time of writing).

3.4.3 Verification

At the time of this writing, computational tools can not yet fully substitute for experimental studies, and it is important to have some degree of faith in code implementation. For the sake of completeness, in this section the aim is to show the level of temporal and spatial accuracy achieved by the scheme outlined above. Two test cases are presented: the first one is for unsteady computation, and the second one is for convergence to a valid steady state.

Case 1: Steady State

In the steady state, from a numerical stand point, one expects that the residual vector, right hand side of Eq. (3.6), should tend to zero irrespective of initial conditions. Calculation for a typical Busemann inlet was performed with initial

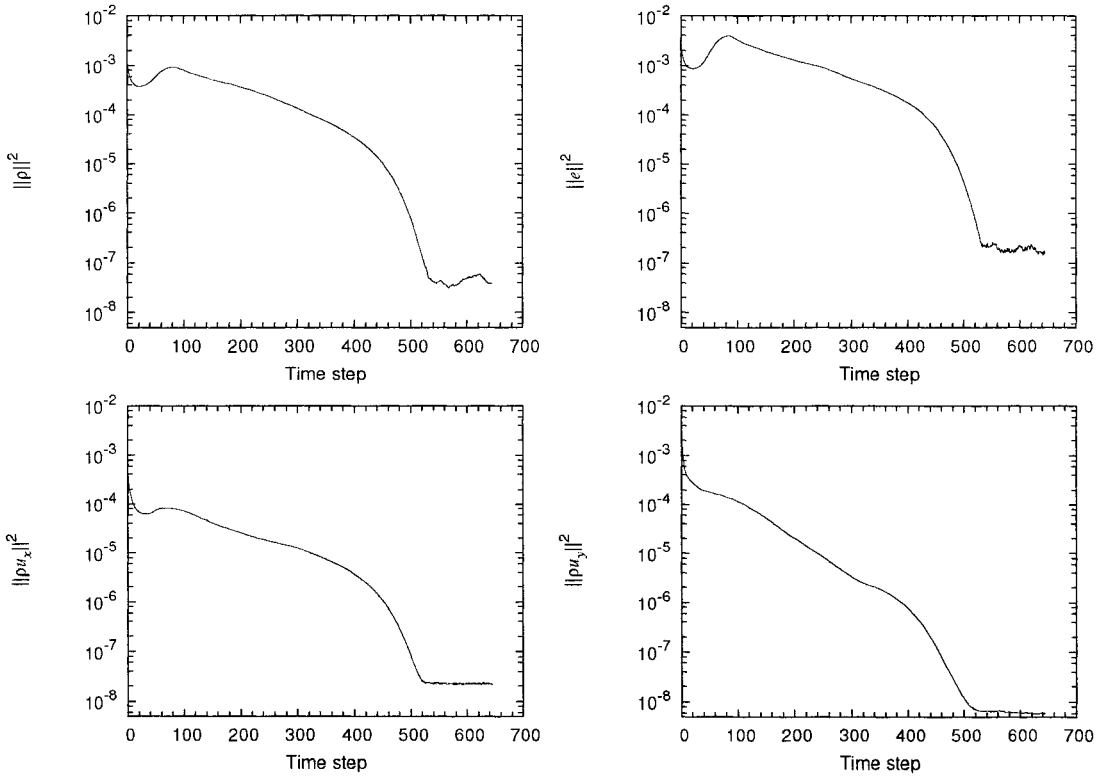

Figure 3.2: L_2-norm of residual vector, normalised by mesh size

conditions set to free-stream flow everywhere, and convergence to steady state was obtained as shown in Fig. 3.2.

This provides a good check when coupled with the fact that earlier a pseudo-analytical solution was obtained for a steady-state Mach number field in a Busemann inlet (*c.f.*, Article 2.3.2); a good comparison with this non-trivial solutions proves code reliance. Figures 3.3 and 3.4 compare respective solutions obtained using Taylor-Maccoll and `SolverII`. At 3 levels of refinement, with approximately 6300 nodes, excellent agreement is obtained. Further grid-refinement (4 levels, Fig. 3.4) produces a more sharply captured shock, showing the effectiveness of the refinement sensor.

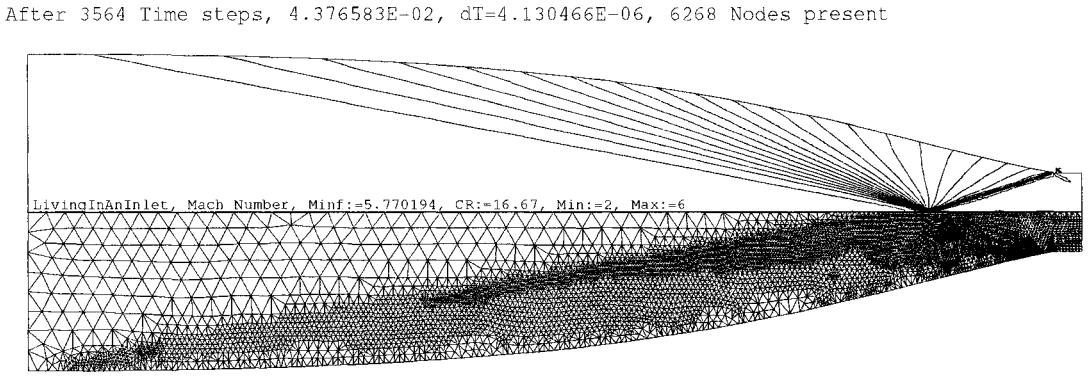

Figure 3.3: Iso-Mach contours plotted for Busemann M5.77C16.67 inlet (top-half); solution adapted mesh, with $m_{\max} = 3$ (bottom-half).

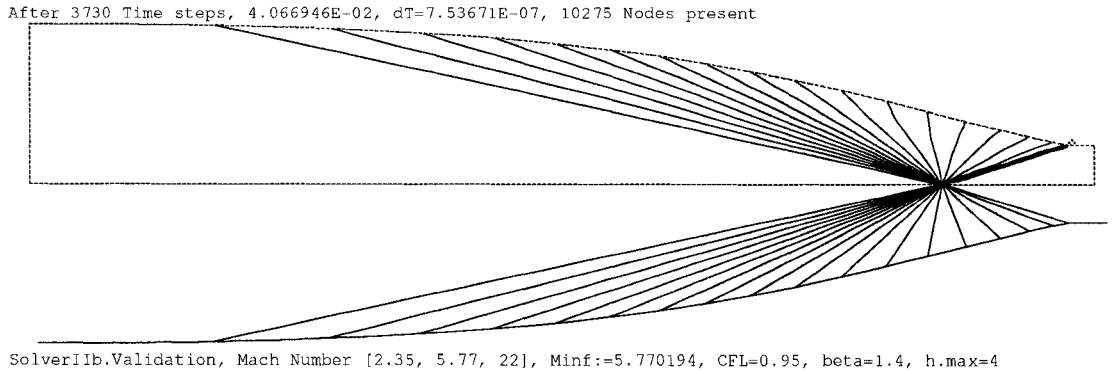

Figure 3.4: Comparison of iso-Mach contours: top-half shows `SolverII` results, while the Taylor-Maccoll solution is shown in bottom-half); corresponding contours are drawn at the same values, in increments of 0.155.

Case 2: Transience

The starting process is inherently unsteady in that it involves a moving shock wave. It is therefore important to ensure that some level of temporal accuracy is maintained. To this end, one may extend to two dimensions (axisymmetric) the 1-D classical problem known as Sod's [25]. The problem consists of two states (labelled as the left and right states) that are separated initially at $t = 0$. Solution starts with a hot, high-density gas in the region $x < 0$, and a cold, low-density gas in the region $x > 0$; the gases are initially at rest. The standard parameters for this problem are: $p_L/p_r = 10$, $\rho_L/\rho_r = 8$. The flow evolution is tracked in time as the gasses are allowed to interact, causing a shock wave to propagate rightward into the low-density medium, and also causing a rarefaction wave to propagate leftward into the high density region. The resulting flow regions are separated by a contact surface. Analytic solutions for the three resulting states can be obtained from the shock-tube theory at $t = 0^+$, and because the problem is self-similar, the exact solution is available in the (x, t)-plane. It should be noted that a good comparison (between `SolverII` results and the analytical solution to this problem), verifies not only the unsteady terms, but also gives an indication of the efficacy of the adaptive mesh refinement. As an added bonus here, the instantaneous rupture of the diaphragm is simulated using the multi-block facility with invisible internal boundary, thus guarantying proper functioning of the sum of various parts of `SolverII`. Figure 3.5a shows the initial mesh with intact diaphragm at $t = 0$. Figure 3.5b compares the exact solution with `SolverII` results, and excellent agreement is found between the two; it is clear that the shock travels at the correct speed, and that it is captured exactly (near $x = 8.4$). The contact surface also travels at the correct speed, but is somewhat smeared (near $x = 6.8$, although, it may still be considered as *state of the art*). Figure 3.5c shows the density-field in

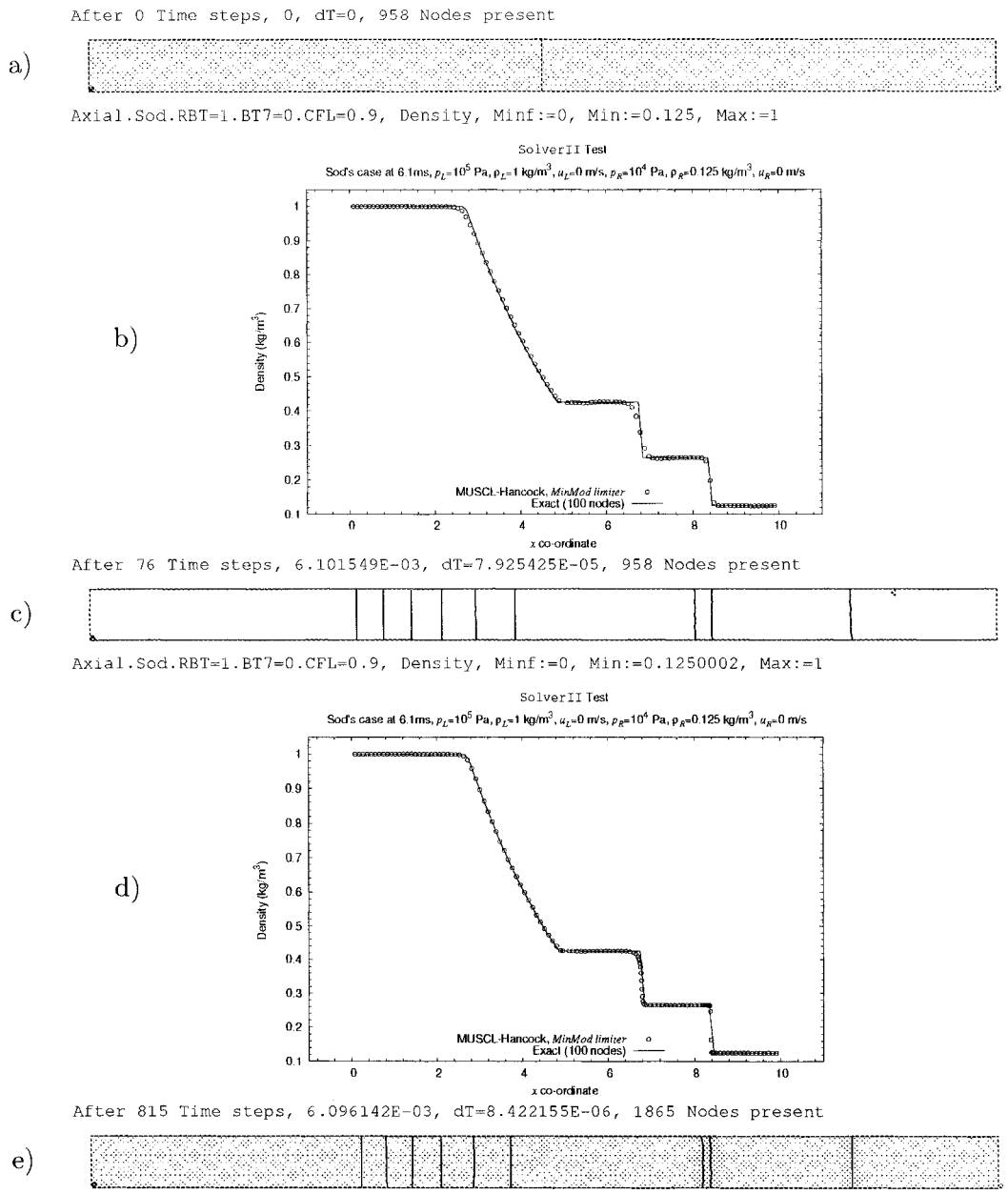

Figure 3.5: `SolverII` verification using Sod's problem: (a) initial mesh, showing intact diaphragm; (b) comparison with exact solution, $m_{\max} = 0$; (c) isopycnics at $t = 6.1\,\mathrm{ms}$, $m_{\max} = 0$; (d) same as (b), except $m_{\max} = 3$; (e) same as (c), but with $m_{\max} = 3$.

the axisymmetric solution, corresponding to Fig. 3.5b. Similarly, Figs. 3.5(d and e) show an excellent comparison with the exact solution at $t = 6.1$ ms, with three levels of refinement. It is clear that the refinement algorithm tracks the moving discontinuities in time, while restoring the basis mesh in regions left behind by the discontinuities. Thus, the contact surface is much less smeared in Figs. 3.5(d and e) compared to Figs. 3.5(b and c). Roughly speaking, there's an eight-fold increase in accuracy (near discontinuities, the mesh is eight times finer), even though the total number of finite-volumes was only doubled (from 958 in Fig. 3.5c to 1865 in Fig. 3.5e).

Chapter 4

Results and Discussion

4.1 Background

The main objective of this effort was to *numerically* investigate various ways in which high contraction air inlets may be started—this chapter of the document aims to present numerical results and to identify some novel possibilities for the same purpose. In essence, an attempt is made to identify the effects of flow-unsteadiness on the overall starting process—especially as a result of boundary-imposed high temporal/spatial gradients in the flow.

4.1.1 Overview

This chapter is broken into several main sections (see table of contents). First, the naming convention for identifying simulation models is explained. The nomenclature will be defined in a local context as each new symbol is introduced. Second, results dealing with *quasi-steady* flows will be presented and discussed, showing application of over-speeding, unstarting and mass-spillage. In the third section,

results associated with *unsteady* flow phenomena are examined. The first part of that section pertains to accelerative starting (high temporal gradients in flow), while the second part will address the concept of frangible structures such as diaphragms (high spatial gradients). Every effort is made to provide a smooth transition between discussions of a disparate nature, and it is hoped that this will help the reader keep a mental picture of the underlying structure among various sections and subsections.

4.1.2 Models and Naming Convention

Most of the research described here is based on a standardised set of models, generated in the early stages of the study; some examples include: Busemann.M2.2A0.74, Busemann.M4C5, and Busemann.M6C10. The naming convention is as follows: the first part of the name refers to the type of geometry under consideration, *e.g.*, "Busemann" or "Reversed de Laval." The second part contains design conditions, *viz.*, Mach number M, and either the exit to entrance area ratio AR (A_t/A_i), or a more descriptive contraction ratio CR (A_i/A_t)—*these notations will be used interchangeably.* Additional information may be conveyed by adding suffixes, usually carrying context specific details, *e.g.*, θ35.P0.05 for a conical diaphragm at 35° with initial internal pressure ratio of 0.05 as compared to the free stream value. In this context, initial means before diaphragm rupture (Article 4.3.2.2).

Figure 4.1 is provided as a reference for the reader, showing *some* of the models discussed in this chapter in relation to their starting characteristics. For reasons that will become clear later on, two sets of models are shown in Fig. 4.1, *viz.*, low contraction and high contraction. In this context, low contraction inlets refer to all such geometries, which are effectively located (in the inlet parameter space), close to the quasi-steady starting-curve as described by Eq. (2.11). Conversely,

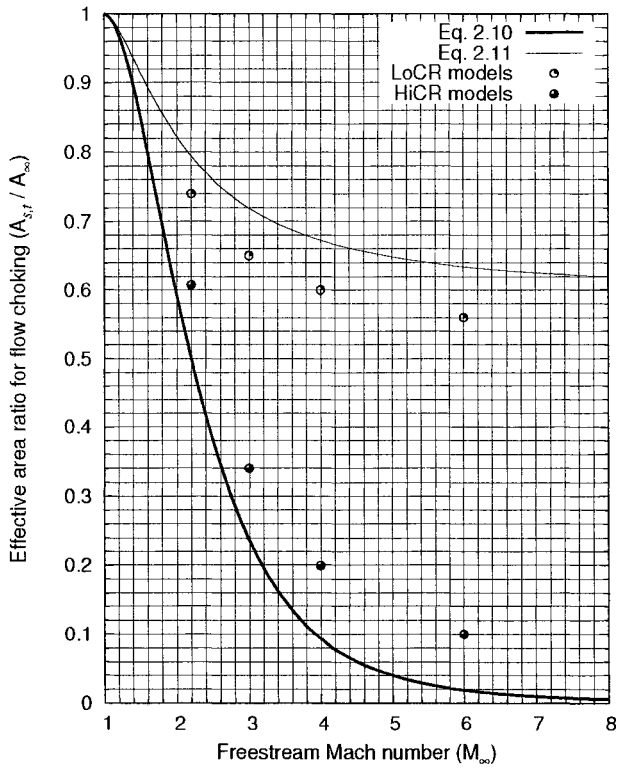

Figure 4.1: Starting and operational characteristics of some models used in this study.

high contraction inlets, in Fig. 4.1, are located close to the isentropic diffusion curve described by Eq. (2.10).

This classification may seem a bit simplistic at first, and certainly there are several parameters associated with an inlet designed for hypersonic flight conditions. However, in the present context, two parameters are relevant (at the least, considered most important by the author). Thus, Fig. 4.1 shows some of the models, discussed in the following material, in relation to the two most important design parameters: *viz.* Mach number and the effective area ratio.

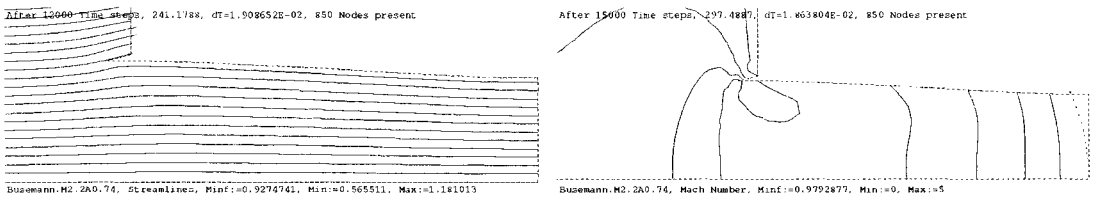

(a) (b)

Figure 4.2: Late stage in the subsonic phase of acceleration for a low contraction inlet (Model: Busemann.M2.2A0.74): (a) Streamlines showing flow spillage; $M_\infty = 0.93$, $t = 0.84\,\mathrm{s}$. (b) Iso-Mach contours, signifying flow choking by the presence of grey contour in the throat region; $M_\infty = 0.98$, $t = 1.03\,\mathrm{s}$.

4.2 Quasi-Steady Flows

4.2.1 Starting by Over-Speeding

The basics of inlet starting by the over-speeding process were detailed in Article 2.2.1, with the assumption of one-dimensional, quasi-steady flow. It was noted that Kantrowitz' condition holds well in practice and that it enables one to use over-speeding as an effective method for establishing started flow in relatively low contraction inlets. To further examine this statement, a Busemann inlet was designed for Mach 2.2, with an area ratio of 0.74 (Model: Busemann.M2.2A0.74), and then subjected to a constant acceleration at 10 *g's*, causing it to accelerate[†] from M0 to M2.2.

Figure 4.2 shows subsonic stages similar to the ones described in Fig. 2.4. The first picture shows subsonic flow throughout, while some flow spillage is taking place. The second image shows subsonic free stream flow, while the throat is choked (the right most grey contour is a sonic line). As the inlet is further accelerated and the free stream Mach number goes supersonic, a bow shock is formed

[†]Here, $g = 9.806\,\mathrm{m/s^2}$; it will be shown in Article 4.3.1, $10\,g$ flow is well within the realm of quasi-steady conditions.

(as shown in Fig. 4.3), thereby restoring the subsonic mechanism of flow-spillage behind it.

For this particular model, as the Mach number reaches the design value, $M_D = 2.2$, it is unable to swallow the required mass and thus remains unstarted. From Fig. 2.3 and Eq. (2.11), the inlet must be over-sped beyond $M_S = 2.72$ for the shock to enter the inlet; this is precisely the value of M_∞ shown in the last image of Fig. 4.3. Further increasing the Mach number leads to a started inlet as shown in Fig. 4.4.

Conceptually, the shock reaches a position compatible with conservation of mass across it, so one may induce the following fact: for external compression inlets, such as spike-based geometries, as well as for three-dimensional scoop-like inlets, the effective area contraction during the starting process is still governed by Eq. (2.11).

Once started, the craft may be slowed back to inlet design conditions for optimal performance. Figure 4.3 shows the started inlet at $M_\infty = M_S^+$ and $M_\infty = M_D$. It should be noted that for scramjet applications, supersonic Mach number is desired throughout; this highlights a minor difference between Fig. 2.4 and those described in the present chapter. This section is concluded by remarking that quasi-steady starting in multi-dimensional inlets is described by Kantrowitz' relation.

4.2.2 Operating Limit and Unstarting

In the discussion thus far, emphasis has been placed on establishing started flow in inlets. It is equally important to prevent a started inlet from spontaneously switching to the unstarted mode. In Article 2.1.4, an upper limit on area contraction was described for steady operation of a started inlet. Additionally, it is

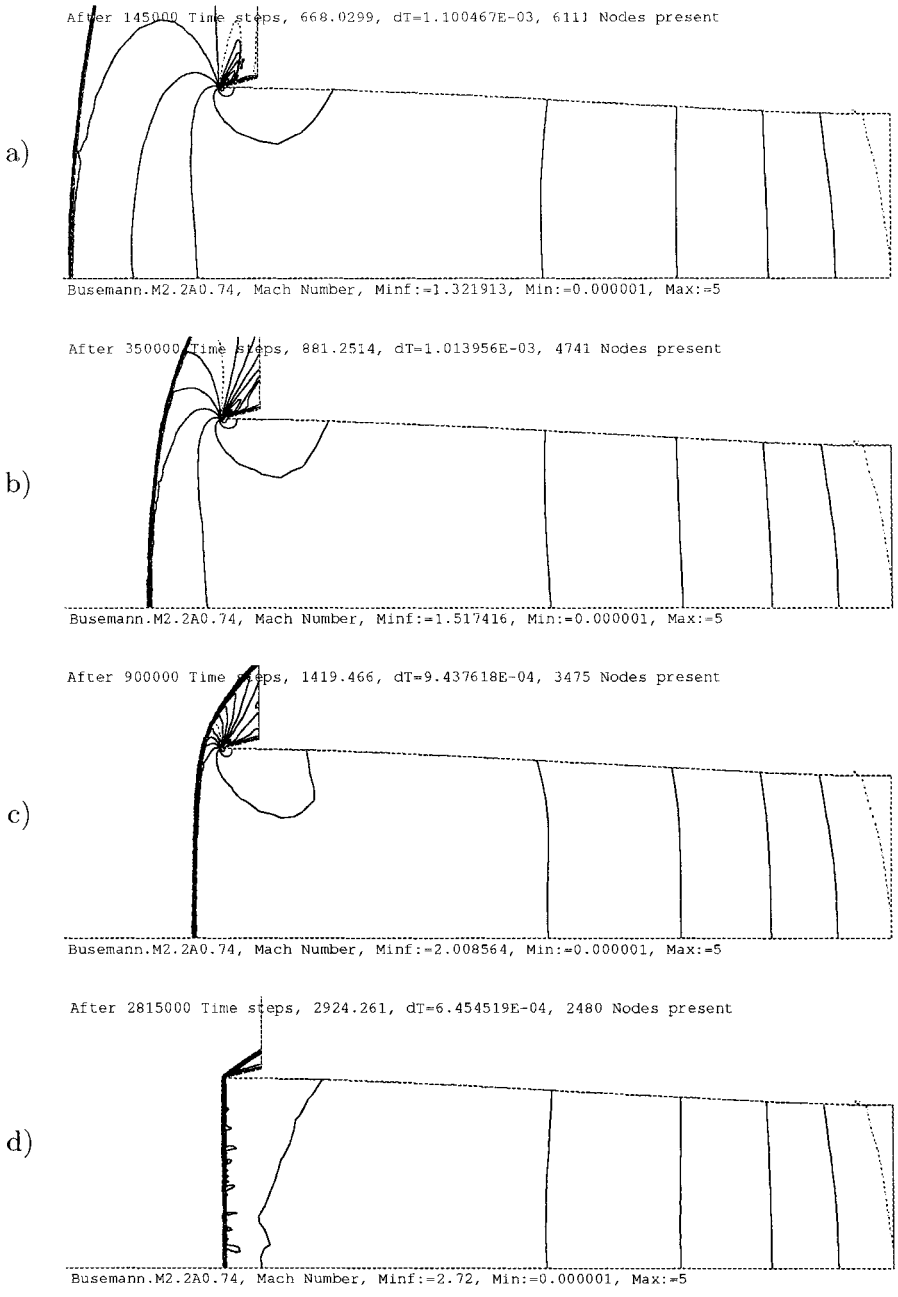

Figure 4.3: Stages in the supersonic phase of acceleration for a low contraction inlet (Model: Busemann.M2.2A0.74). Shock moving successively closer to the inlet lip with increase in free stream Mach number. Sonic line (grey, right most contour) at the throat indicates local flow choking, $t = 2.32$–$10.2\,\mathrm{s}$.

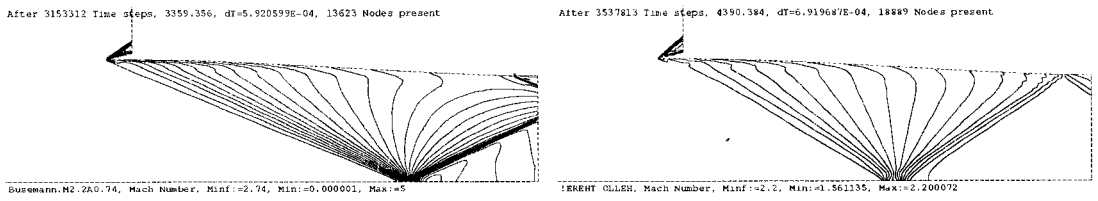

(a) (b)

Figure 4.4: Started inlet (*cf.* Fig. 4.2), iso-Mach contours: (a) during over-speeding, $M_\infty = 2.74$, $t = 11.7\,\mathrm{s}$; (b) after reaching design conditions, $M_\infty = 2.20$, $t = 15.3\,\mathrm{s}$. It is interesting to note that the time scales involved in this simulation are several orders of magnitude larger than those usually associated with shock wave propagation. It took 3.54 million time steps in total to compute this result.

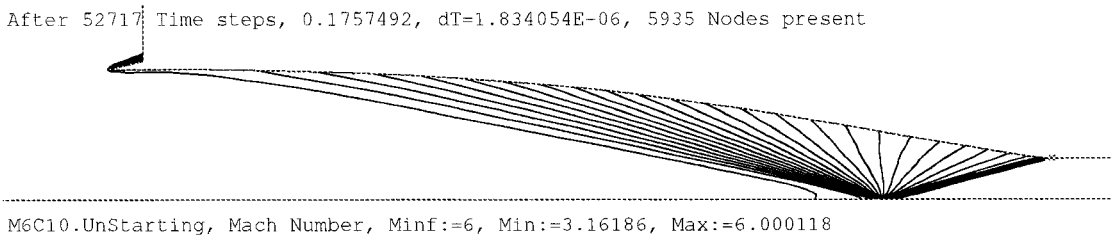

Figure 4.5: Iso-Mach contours in a Busemann inlet at design conditions (Model: Busemann.M6C10). $M_\infty = 6$, $t = 176\,\mathrm{ms}$, $r_i = 0.776\,\mathrm{m}$.

clear (see labels in Fig. 2.3), that for a fixed geometry inlet (specified area ratio), there exists a lower limit on the free stream Mach number; below this value of Mach number, the inlet will unstart. For non-isentropic flows, this value is too optimistic and generally, the inlet will unstart at slightly higher Mach numbers. In this section, CFD results showing the unstarting process will be examined. The discussion also provides a pleasantly surprising segue into the next section, as will become clear with due discourse.

Steady, started flow was established in a Busemann inlet designed for Mach 6, with a contraction ratio of 10, as shown in Fig. 4.5. The inlet was then subjected to a gradually† decreasing free stream Mach number.

†Change in free stream conditions was specified using: $\frac{\mathrm{d}M}{\mathrm{d}t} = 10^{-6}$, with $[\mathrm{d}t] \approx 2\,\mu\mathrm{s}$.

It was observed, at off-design conditions, that the internal shock structure changes continuously, and that the flow remains stable for $M_\infty > 3.95$. It was concluded that the unstarting process began at $M_\infty \approx 3.95$ (*cf.*, $M_\infty = 3.92$), vis-à-vis the lower limit on Mach number for continuous, isentropic operation at this area ratio (Fig. 2.3). As this value is approached from higher Mach numbers, wave angle increases sufficiently to cause local subsonic pockets to appear in the flow (Fig. 4.6a). Further reduction in free stream Mach number causes complete flow choking at the throat—this, and changes further ensuing, are best described by the sequence of pictures shown in Fig. 4.6. The flow can be seen spontaneously reverting to an unstarted mode starting with Fig. 4.6b.

Once unstarted, the bow shock oscillates for a while, before finding its equilibrium position. Figure 4.7 shows a few images demonstrating this phenomenon. It is interesting to note that the unstarting simulation described here took a total of 2.41 million time[†] steps to complete.

4.2.3 Second Design Point

While simulating the unstarting process described in Article 4.2.2, it was observed that as the free stream Mach number is reduced from its design value, the shock angle increases gradually, causing it to impinge upstream of the throat point. This leads to a reflected shock from the surface and the formation of an axisymmetric expansion-fan[‡] originating at the corner (Fig. 4.8a). The decrease in free stream Mach number and increase in angle of primary shock causes the reflected shock to re-reflect at the axis and interact with the expansion taking place at the corner. The change in wave-structure is progressively shown in Fig. 4.8.

[†]This example highlights the disparate time scales involved in this study (total simulation time of over 5 s!).

[‡]Strictly speaking, this analogue to the planar P-M fan is not self-similar.

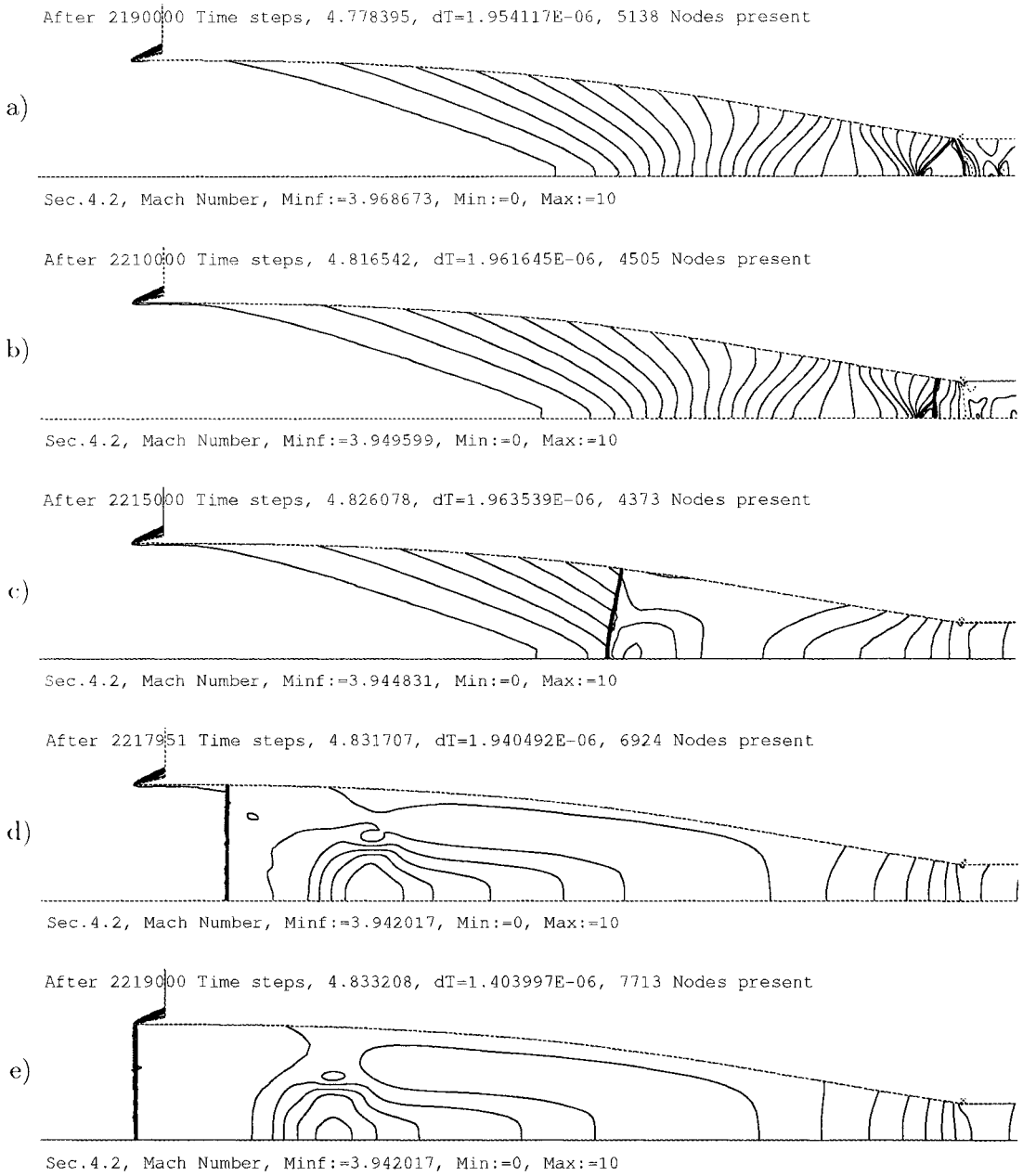

Figure 4.6: Iso-Mach contours in a Busemann inlet (Model: Busemann.M6C10). Images showing: (a) flow just prior to unstarting, whereat appearance of sonic line (grey contour) in throat region signifies presence of subsonic pockets, $M_\infty \approx 3.97$, $t = 4.78\,\mathrm{s}$; (b-e) flow during unstarting process, whereat frames in succession showing a near-normal shock moving upstream (leftward) as the inlet unstarts, $M_\infty \approx 3.94$, $t = 4.8165$–$4.833\,\mathrm{s}$.

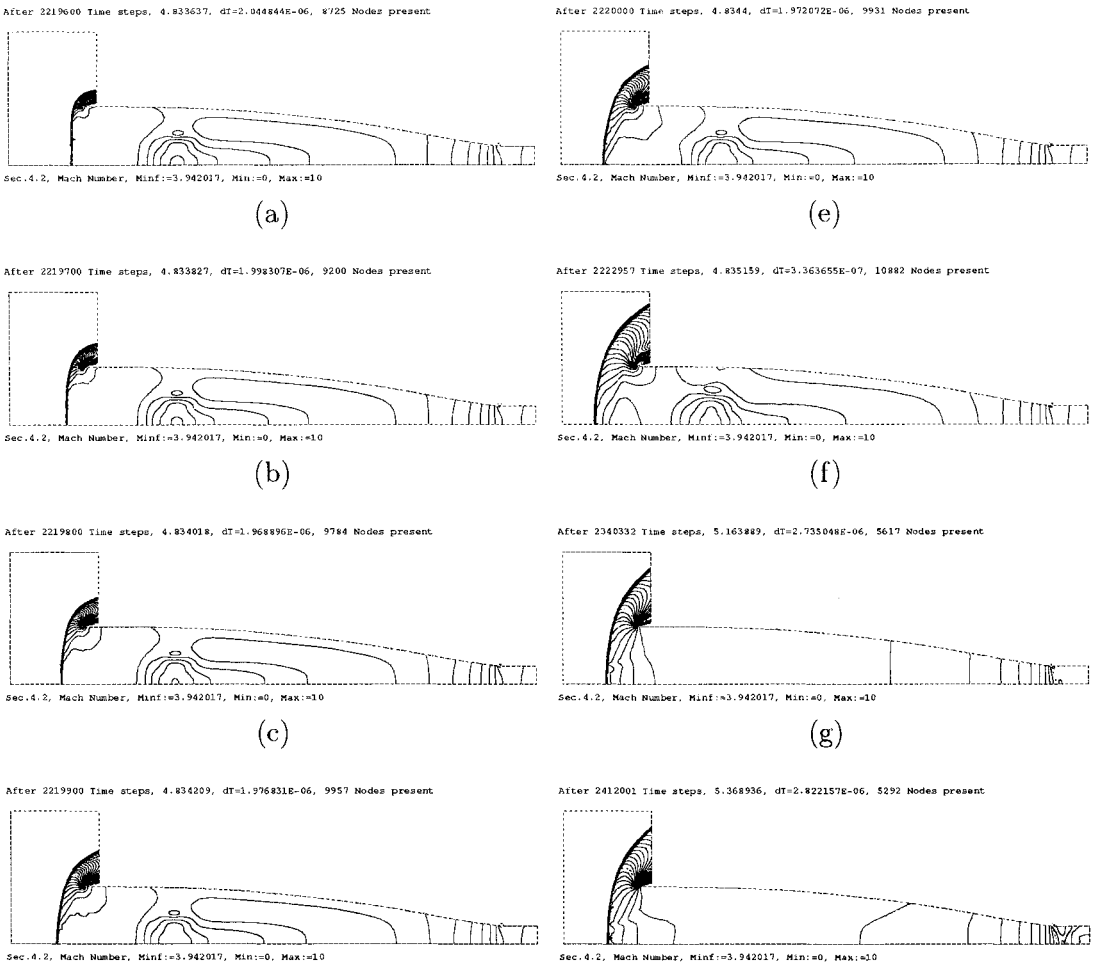

Figure 4.7: Iso-Mach contours showing establishment of a bow wave after completion of the unstarting process in a high contraction inlet (Model: Busemann.M6C10). $M_\infty = 3.94$, $t = 4.83$–5.37 s.

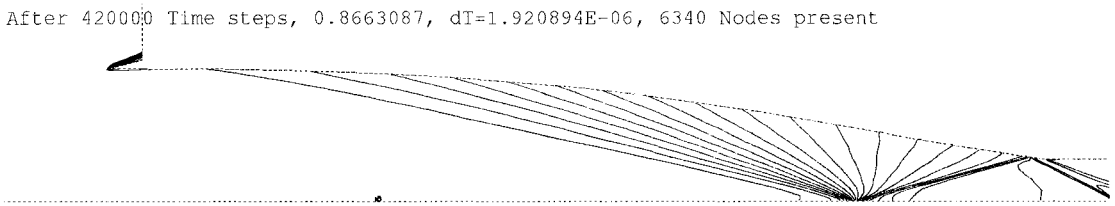

(a) $M_\infty = 5.66$, $t = 866\,\mathrm{ms}$

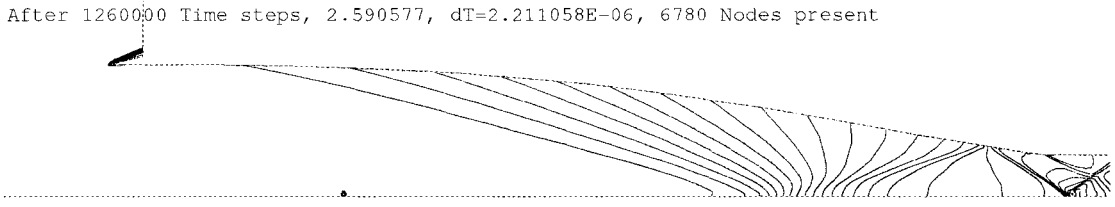

(b) $M_\infty = 4.86$, $t = 2.59\,\mathrm{s}$

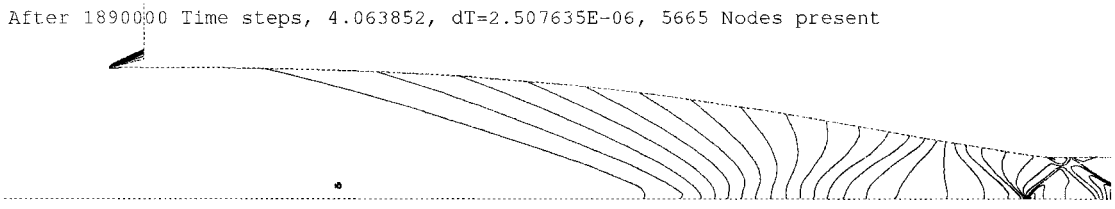

(c) $M_\infty = 4.25$, $t = 4.06\,\mathrm{s}$

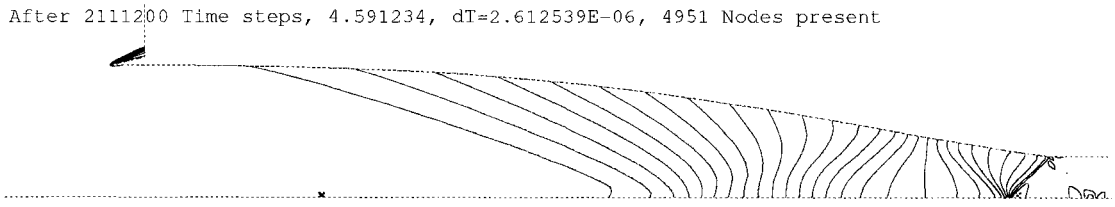

(d) $M_\infty = 4.04$, $t = 4.59\,\mathrm{s}$

Figure 4.8: Second design point—Iso-Mach contours in a high contraction inlet (Model: Busemann.M6C10).

At a certain value of free stream Mach number, the evolving flow-structure leads to a near-perfect wave-cancellation (Fig. 4.8d). It is unlikely that the exit flow can be made perfectly uniform, and the existence of a small Mach disk due to the reflected shock is almost certain. Nevertheless, a nearly uniform exit flow is produced at a Mach number that is significantly below its design value. The extent of this fortunate, multi-design-point phenomenon, in the Busemann inlet parameter space, is well worthy of further study and exploitation.

4.2.4 Perforations

As hinted earlier (Articles 1.4 and 2.2.3), there exists a surefire method of starting high contraction air inlets. An large set of numerical results has been obtained showing that slots (two-dimensional perforations) may be successfully employed for wide ranges of area contraction and free stream Mach number. The object of this discussion is to outline the important lessons relevant to the present study. For the sake of brevity, only a small sample of the results is included, and the redundant details, in the voluminous data that was generated in the process, are omitted.

4.2.4.1 Slit Modelling

The basic mechanism for flow spillage was described in Article 2.2.3 assuming that locally, the flow is steady and that dimensionally it behaves in a planar fashion. Figures 4.9 and 4.10 show the general flow structure in a perforated inlet during the unstarted mode and these results indicate that this assumption (*v.s.*) is reasonable even for relatively wide slits (as evident by near-radial rays of the internal expansion fans). It is also evident, from the adapted mesh shown in Fig. 4.9, that simulation of the external flow requires an disproportionately

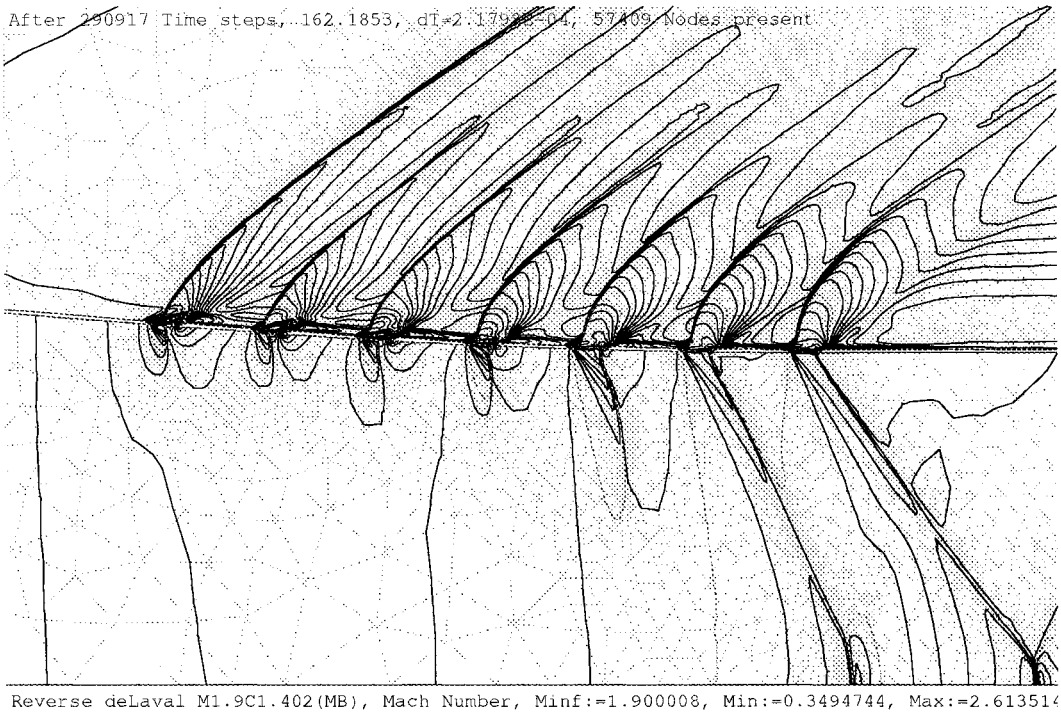

Figure 4.9: Flow through slits (Model: Reversed.de.Laval.M2.5)—Iso-Mach contours in and around the inlet with open slits. Flow is from left to right, the top flow is external to the inlet, while the inlet is unstarted with a bow shock (not shown) situated just upstream of inlet lip. $M_\infty = 1.9$.

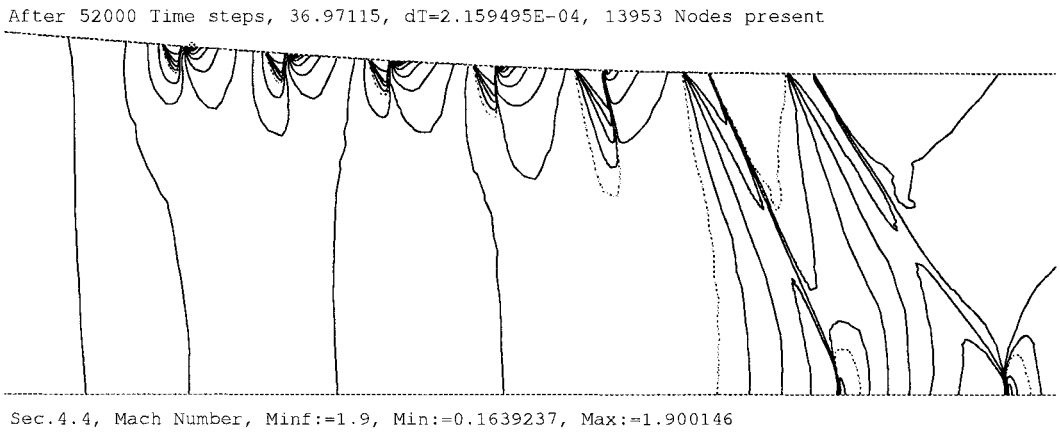

Figure 4.10: Flow through slits (Model: Reversed.de.Laval.M2.5)—Iso-Mach contours with internal flow only, *c.f.* Fig. 4.9. External pressure specified as twice the static value in free stream. $M_\infty = 1.9$.

large portion of the total number of vertices present in the mesh. For the rest of the numerical simulations with perforations, the external computational domain is culled away, and instead a pressure boundary is specified at each perforation. Figure 4.10 shows a result similar to Fig. 4.9, with external pressure set to twice the free stream static value.

4.2.4.2 Spillage Flow Coefficient

The extent to which the internal flow is influenced by the external pressure may be estimated from Fig. 2.6. Streamlines through a slit in a constant area channel are shown in Figs. 4.11a and 4.11b; the flow is parallel to the wall as it approaches the leading edge of the slit, and an initial pressure ratio of 0.1 is specified across the slit. The radial location of the streamline hitting the trailing edge of the corner has been determined using the *virtual probe*[†] feature in `SolverII`, *v.i.* The approach Mach number in Figs. (4.11a and 4.11b) is (1.01 and 1.5), while the flow coefficient is (0.26 and 0.21), respectively; these values compare favourably to (0.264 and 0.205), as obtained from Fig. 2.6 at the respective pressure ratio and Mach numbers. Some additional observations are noted regarding the particular flow depicted in Fig. 4.11: 1) it is for an isolated slit, where the approaching flow is uniform and initially parallel to the wall; 2) the combination of local Mach number and flow turning near the trailing-edge leads to an attached-shock configuration. Similar analysis (post processing) of results obtained for perforated diffusers, however, reveals that the flow coefficient, for slits downstream of the shock, typically has a higher value than 0.26 and lies in the range (0.2–0.6). The difference is attributable to departure from the simple/ideal flow described above,

[†]`SolverII` window features a multi-panel status bar displaying various mesh properties, as well as the value of displayed/contoured function at the location pointed to by the mouse cursor. It can also be used to trace the streamline which hits the slit trailing edge.

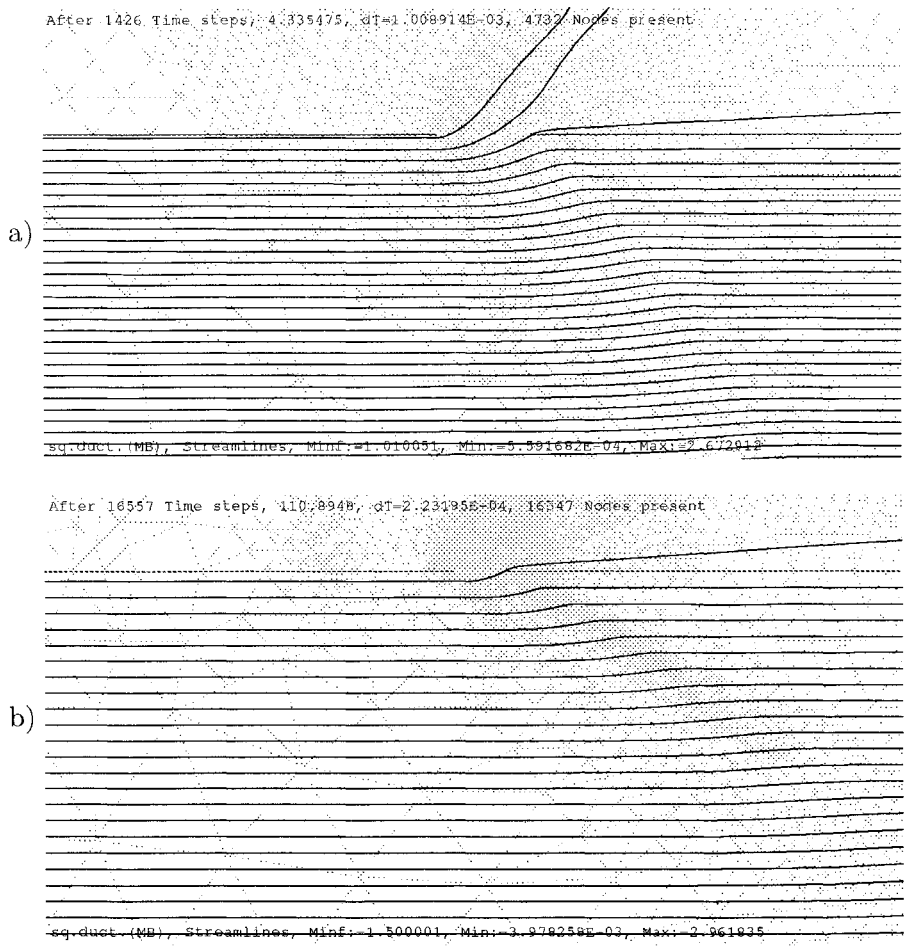

Figure 4.11: Flow spillage through an isolated slit with: (a) $M_1 = 1.01$, $\frac{p_2}{p_1} = 0.1$; (b) $M_1 = 1.5$, $\frac{p_2}{p_1} = 0.1$.

while some of the identifiable factors contributing to this favourable increase in spillage include: 1) non-uniform/non-parallel flow approaching the slits; 2) interaction between closely spaced slits; 3) detached trailing edge shock caused by large flow angle approaching the trailing edge. To validate the overall behaviour of slits, especially as it relates to spillage through perforations, in the following discussion, a quantitative comparison with the experimental work of Ref. [4] is drawn.

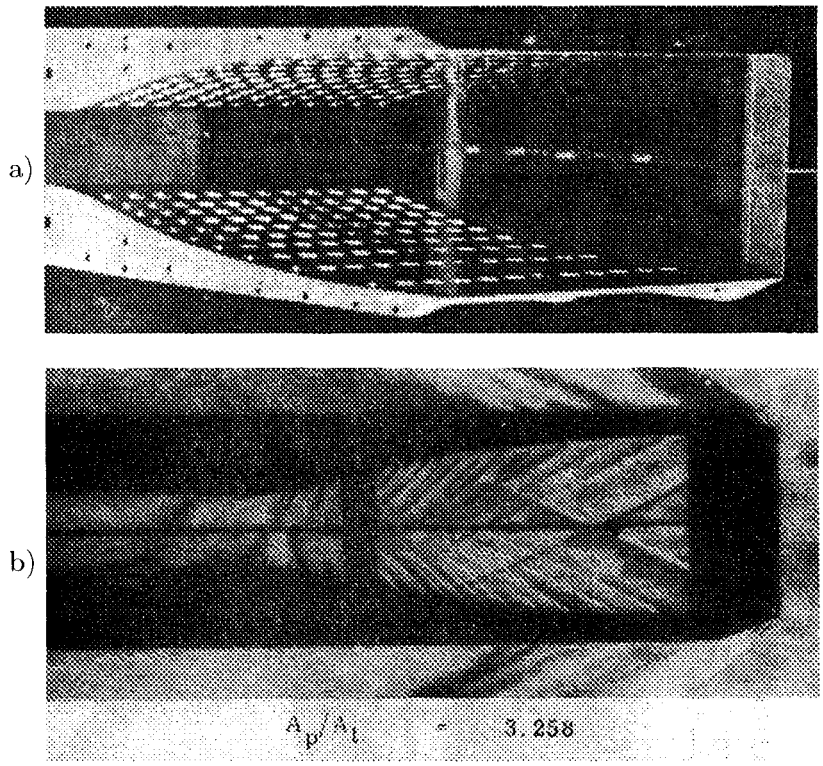

Figure 4.12: Mach 2.5 reversed de Laval nozzle, taken from Ref. [4]: (a) General view of diffuser, several rows of circular (drilled) perforations are visible; (b) Experimental schlieren, showing started flow (*cf.*, Fig. 4.13d), with $A_p/A_t = 3.258$, $A_e/A_t = 1.110$.

4.2.4.3 Clark's Experimental Work

To examine the applicability of slits in simulating perforations, results obtained here using `SolverII` are compared with the experimental work of Clark [4]. Figure 4.12a shows a planar, perforated inlet, based on a reversed de Laval nozzle design for Mach 2.5, *ibid.* In that study, it was reported that the perforation area to throat area ratio required for starting is: $(A_p/A_t \geq 3.26)$.

For the present study, a geometry was generated using Foelsch's method [6] and subjected to many different slit distributions in simulations under `SolverII`. Figure 4.13 shows a sequence of frames depicting the shock swallowing process for

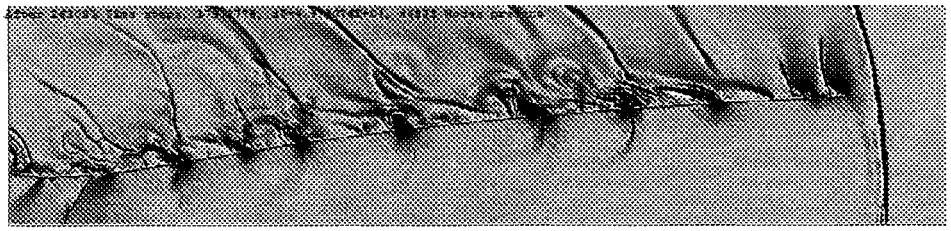

(a) $t = 1.32$ s

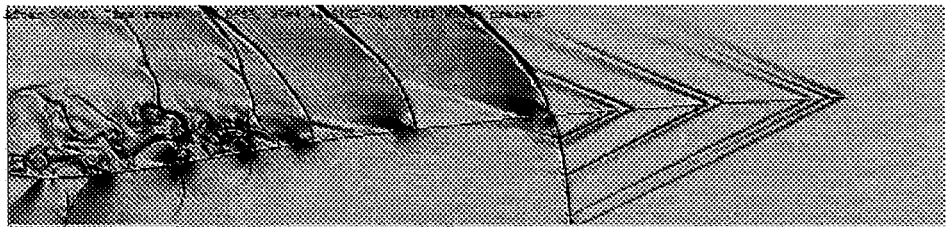

(b) $t = 1.38$ s

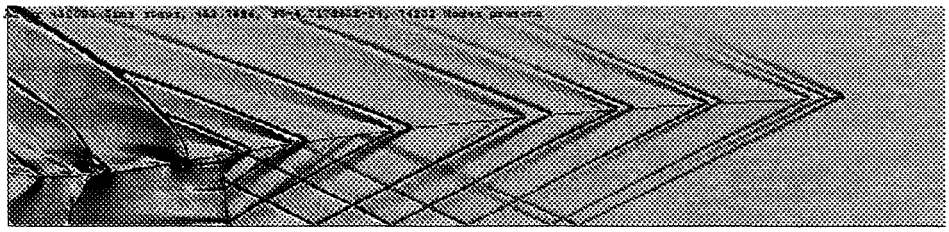

(c) $t = 1.58$ s

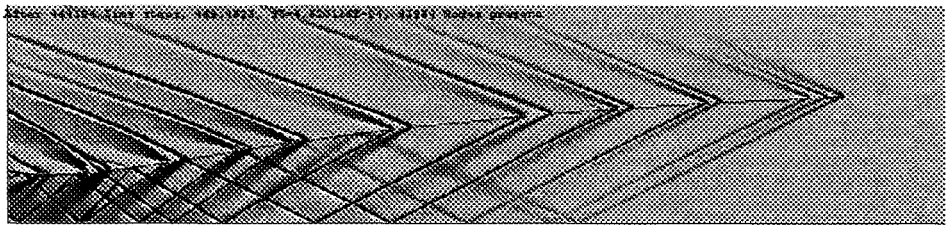

(d) $t = 1.63$ s

Figure 4.13: Mach 2.5 reversed de Laval nozzle with $A_p/A_t = 3.26$. Numerical schlieren produced using `SolverII`— images showing flow development in the perforated diffuser, where only half of the flow is simulated, benefitting from the two-fold planar symmetry; flow is from right to left. Estimated computational cost: 500 Tflop.

this model at ($A_p/A_t = 3.26$), eventually leading to a fully started diffuser (*cf.* Fig. 4.12b). It is interesting to note that despite the differences (two-dimensional spillage, modelling constraints on slit size *etc.*), in the several attempts that were made, this diffuser could not be started at a lower value of $(A_p/A_t)^\dagger$. This result suggests that slits can be used to model spillage in the context of inlet flow starting, particularly, if a row-wise distribution of perforations is to be used (Fig. 4.12a). The resemblance is also likely due to the large amount of spillage that is generally required for inlet starting; in comparison with the size of an individual slit, the total area is greater by an order of magnitude.

Fig. 4.14 shows sampled values of mass flow through some of the slits during the shock-swallowing process. The noise in this figure is attributable, largely to changes in external-flow, which occur during the starting process, nevertheless there are some visible trends. Initially, more mass flow is being spilled than is being swallowed through the choked throat (Fig. 4.14a). During the shock-swallowing process, the total spillage decreases gradually, while the mass flow ingested by the throat increases. For this particular model, mass flow, through a slit that is upstream of the starting-shock, is reduced to roughly a third of its maximum value prior to the shock travelling past the slit. Clearly, this value is a function of local Mach number and diminishes with an increase in Mach number (evident by reduced spillage at slit number 1 in Fig. 4.14b).

This concludes the discussion of Clark's model and comparison with experimental work. In the following discussion, results for higher contraction inlets are presented, thus demonstrating the application of mass spillage to such geometries.

†In this context, slit sizes are fixed. Additionally, there is a fixed number of slits between the throat and entrance sections (21 slits in this particular model); these are uniformly distributed over the diffuser surface, and from which, an arbitrary subset of slits can be selected. This footnote applies to all discussions on slit distribution, henceforth.

a)

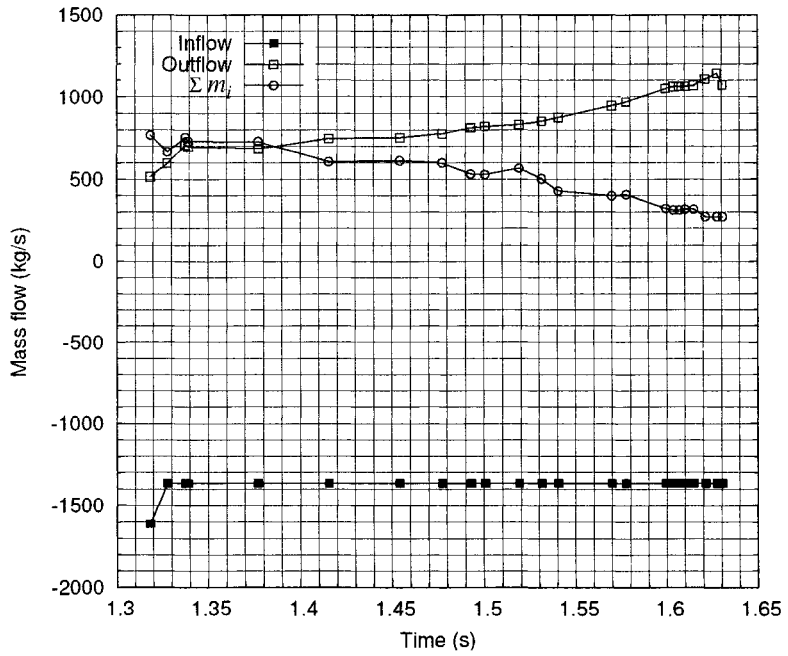

b)

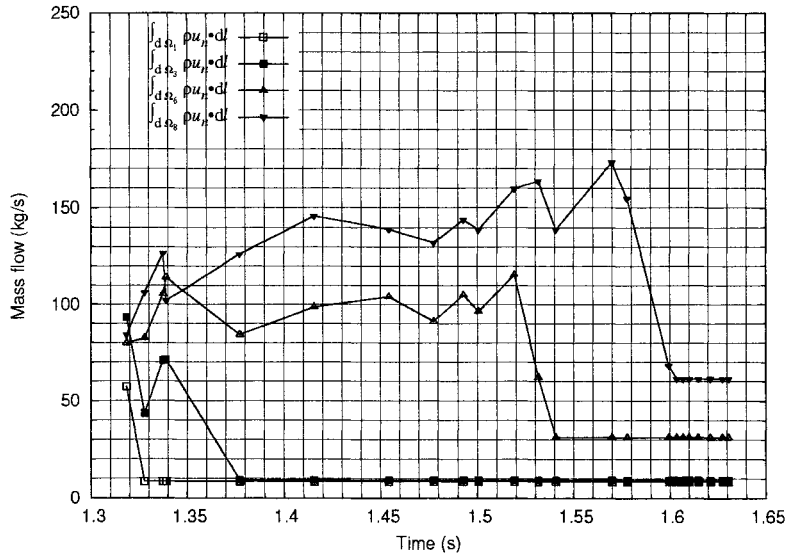

Figure 4.14: Mass flow through slits during starting, *c.f.*, Fig. 4.19: a) Inflow, outflow and the total spillage through slits; b) Breakdown of spillage at selected slits, *viz.*, values sampled during simulation for slits numbered: (1, 3, 6, and 8), with slit number 1 located near the entrance plane (right-most slit).

4.2.4.4 Opening and Closing of Perforations

In the simulations discussed henceforth, the opening and the closing of each slit is simulated as an instantaneous process. Figure 4.15 shows a sequence of frames, detailing the typical schedule of opening employed herein. Steady, unstarted flow is established first, at the design Mach number for the inlet under study. This is done in order to estimate the amount of spillage that is sufficient to restart an inlet at design conditions (recall from Fig. 2.3 that it is easier to establish starting at higher Mach numbers than at lower ones). Thus, it is not possible to start an inlet during the speedup process with the same or lower amount of perforated area; additional spillage is required for starting to take place at lower Mach numbers.

Case 1: Back to Front Sequence

Results for one of the high contraction inlets (Model: Busemann.M4C5) are presented in Fig. 4.15. Figure 4.15a shows a steady bow shock at $M_\infty = 4$, as the inlet failed to start during the acceleration-phase. The presence of a sonic line (grey contour) at the throat, as expected, indicates that the flow is choked there. Indeed, no amount of over-speeding is effective for this inlet unless an appropriate amount of mass spillage is arranged first (at $M_\infty = 4$, $A_t/A_\infty \approx 0.67$).

Figure 4.15b shows steady flow after the first perforation, located nearest to the throat, is opened and the reader will note that a new sonic line is formed, situated at the leading edge of this perforation. In this mode of spillage, from Fig. 2.6, the maximum amount of mass flow is spilled when $M_1 = 1$ at the leading edge of a perforation and when the pressure ratio across the slit is roughly below 0.2.

Figure 4.15c through Fig. 4.15g show sequential opening of perforations two

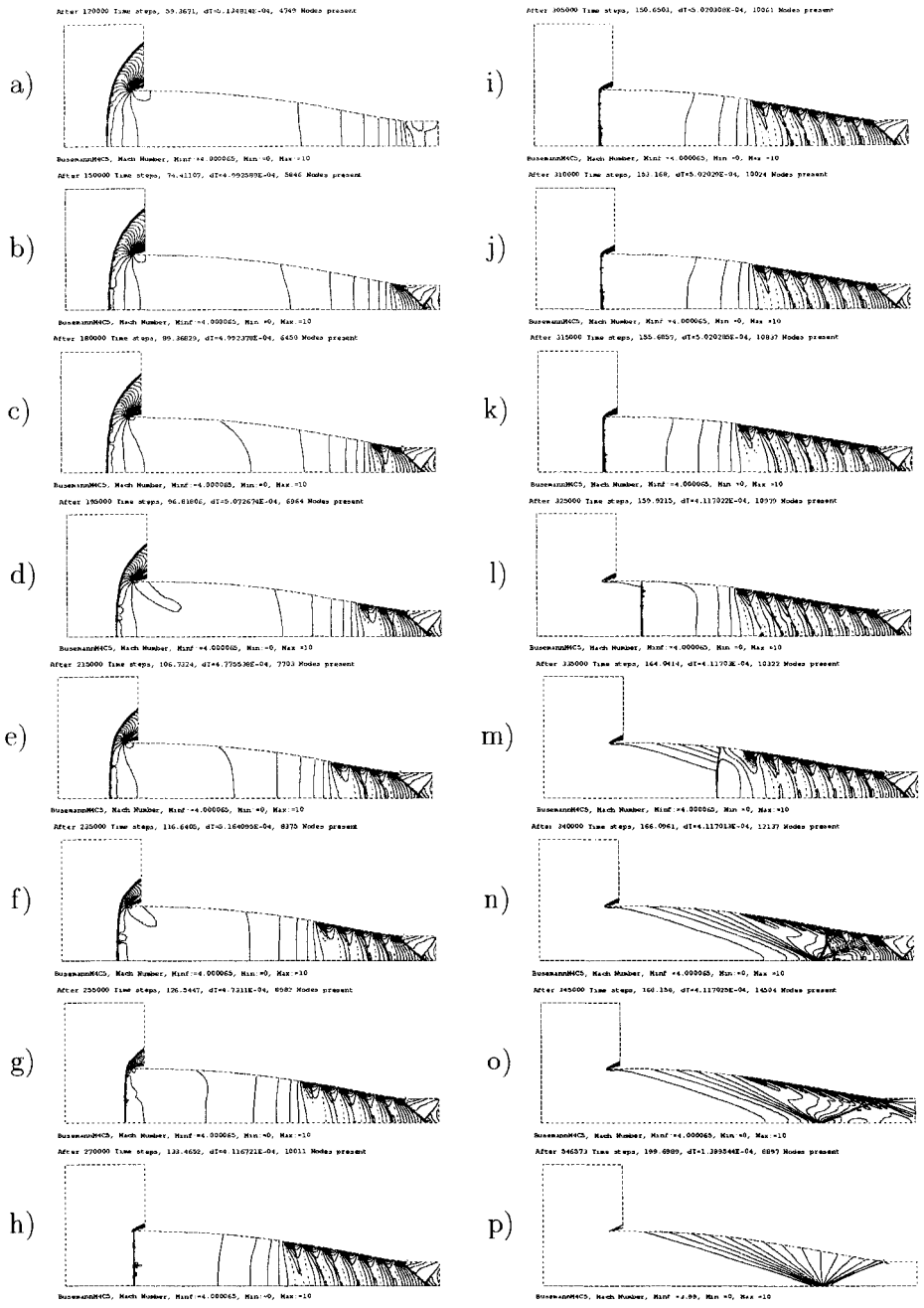

Figure 4.15: Starting by spillage—Case 1. Iso-Mach contours showing quasi-steady flow in a perforated inlet (Model: Busemann.M4C5). Multiply the displayed time (inside figures) by $[t]$ (for inlet of 1 m radius, operating at sea-level, $[t] = 2.49 \times 10^{-3}$ s).

through six. The seventh perforation is placed such that its leading edge occurs at a contraction ratio of 0.67, vis-à-vis, the maximum contraction allowed for quasi-steady starting at $M4$. Indeed, as Figs. 4.15(h–j) show, after this seventh perforation is opened, a sonic line occurs at its leading edge, and the shock situates itself at the inlet lip. Due to lack of unsteadiness in this particular flow, the shock lacks the impetus to travel far enough downstream and get fully swallowed. Such an impetus is provided here by opening the eighth and last slit (Fig. 4.15k)[†].

Figs. 4.15(l, m, and n) show a moving normal shock, with the inlet partially started upstream of it. For this particular model, the process of shock swallowing alone, took about 32 ms. It is clear that the higher momentum fluid in the started inlet (Fig. 4.15o), does not turn as much and the value of flow-coefficient at high Mach numbers is a small fraction of that occurring in the unstarted mode (Fig. 2.6). Finally the perforations may be closed as in Fig. 4.15p.

Although the opening schedule described above leads to a reliable method for starting, it does not necessarily guarantee optimal (minimal) spillage area for starting. It is desirable to obtain the minimal perforation area to throat area ratio (A_p/A_t), which just permits starting. The procedure described above leads to a perforation area ratio $(A_p/A_t = 9)$ for this particular geometry. To this end, an effort was made to determine the effect of slit distribution, on the total spillage area required for starting.

Case 2: Front to Back Sequence

Figure 4.16 shows results from a second trial, sort of an inverse analogue to the above case, whereby the slits were sequentially opened, starting close to

[†]In practice, one would have either made the perforations slightly larger, or temporarily accelerated to a slightly higher Mach number (as explained in Article 4.2.1)

the entrance plane and progressing towards the throat. This procedure was applied until the shock was fully swallowed as shown in Fig. 4.17, for which case ($A_p/A_t = 10.86$). This increase is attributable to two factors: 1) for a given slit width, the geometric spillage area increases with radius, so that in a converging geometry such as an inlet, a slit closer to entrance plane contributes more to the net spillage area than that closer to the throat; 2) spillage through a slit close to the entrance plane is greatly reduced (see Article 2.2.3) as the shock moves downstream of it, necessitating a significant amount of continued spillage downstream of the shock. This result indicates that it is not always desirable to have perforations near the entrance plane, because once the starting-shock is downstream of these perforations, minimal mass-relief is provided by them. Since the mass-flux across the shock moving downstream in a converging section increases, if sufficient (continued) spillage is not provided by perforations downstream of the shock (close to the throat), the shock will stabilise in a partially started inlet as shown in Fig. 4.16; stable location of shock is governed by conservation of mass across the shock.

Case 3: Improvement to Slit Distribution

A third test was performed to determine if some of the unnecessary spillage area could be eliminated from the geometry of Fig. 4.15. The approach taken, essentially identifies some of the slits in Fig. 4.15 as redundant, and unnecessary for (even the quasi-steady) starting process. It was found, through a trial-and-error method, that the perforation distribution of Fig. 4.15 could be modified to exclude the second and the seventh slit (these were never opened) as shown in Fig. 4.18, and in this case ($A_p/A_t = 6.77$) is sufficient to permit starting.

Experience with several geometries designed for various area ratios and Mach

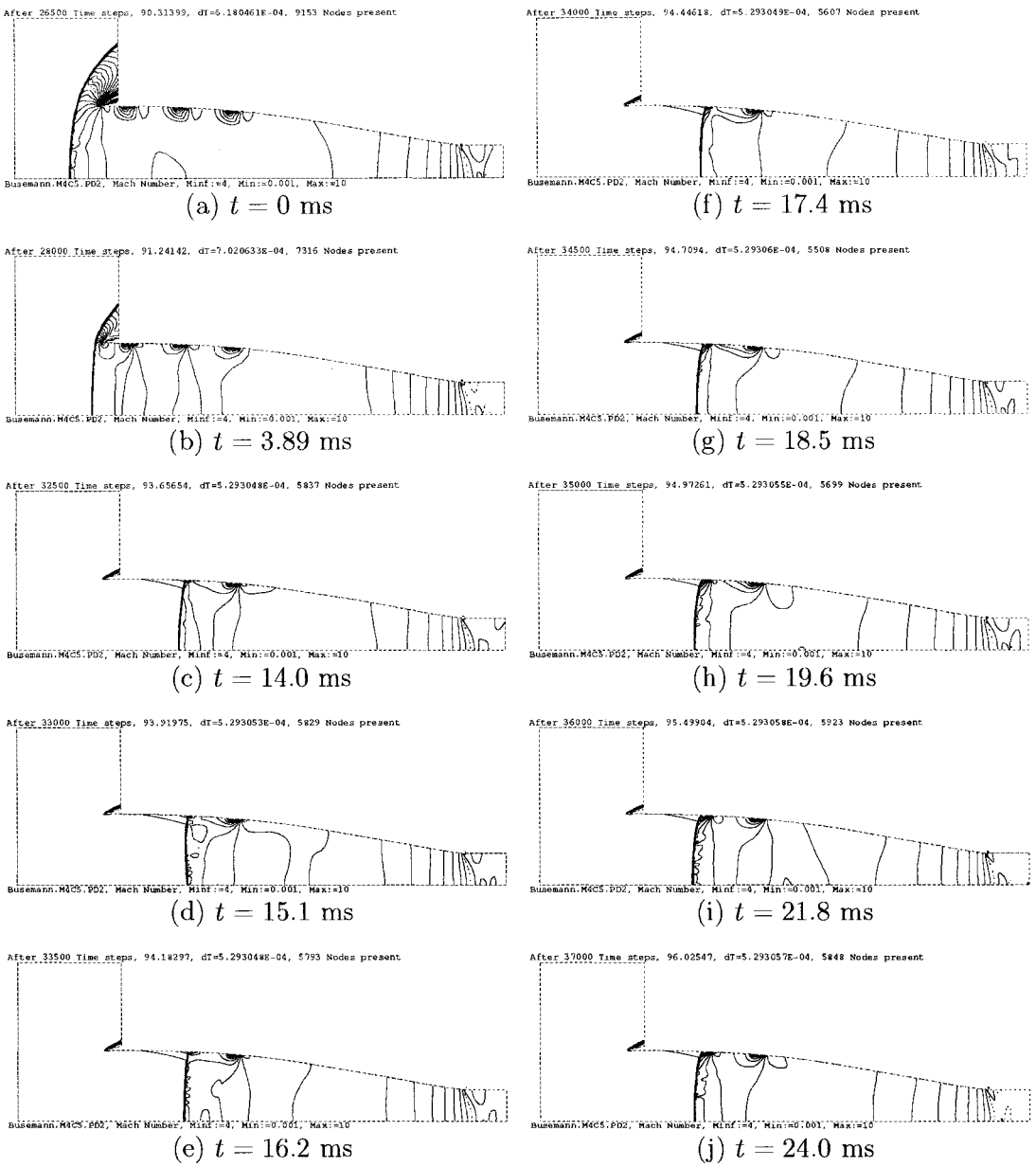

Figure 4.16: Starting by spillage—Case 2. Iso-Mach contours showing shock stabilisation in a partially started, perforated inlet (Model: Busemann.M4C5). $A_p/A_t = 10.86$, $r_i = 1$ m, $t_0 = 379$ ms.

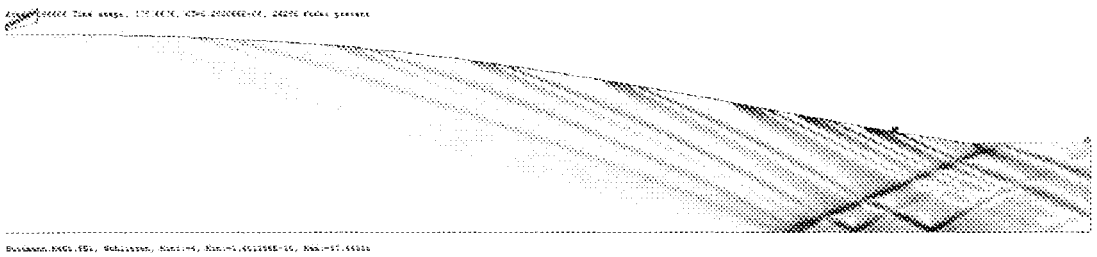

Figure 4.17: Pseudo-schlieren image showing steady flow in a perforated inlet (Model: Busemann.M4C5). Total perforation area to throat area ratio, $A_p/A_t = 10.86$.

numbers suggests that the methods described above can lead to a reliable starting process. This discussion is concluded by noting a few important points: Mass flow relief, as provided by slots is essentially a steady flow phenomenon even if the slots are opened or closed suddenly. Starting of high-contraction inlets by mass venting through surface perforations is effective and governed by the quasi-steady starting theory. A large wall perforation area is required to obtain flow starting in high-contraction inlets. Results also indicate that sudden opening of all slits at once is not significantly more effective; compared to sequential, sudden opening of the individual slits, the overall spillage area is only marginally reduced.

4.3 Unsteady Methods of Starting

Experimental work with high contraction ratio inlets using gun tunnel tests does not suffer from the starting problems; it is well accepted [17] that $CR = 10$ inlets can be successfully started at Mach 8+. The highly unsteady starting flows, coupled with a very low initial pressure and small mass of air in the model are contributing factors that promote starting in the gun tunnel environment. Although such conditions are not readily available for flight vehicles, it is still tempting to gain a fundamental understanding of the role that these factors may

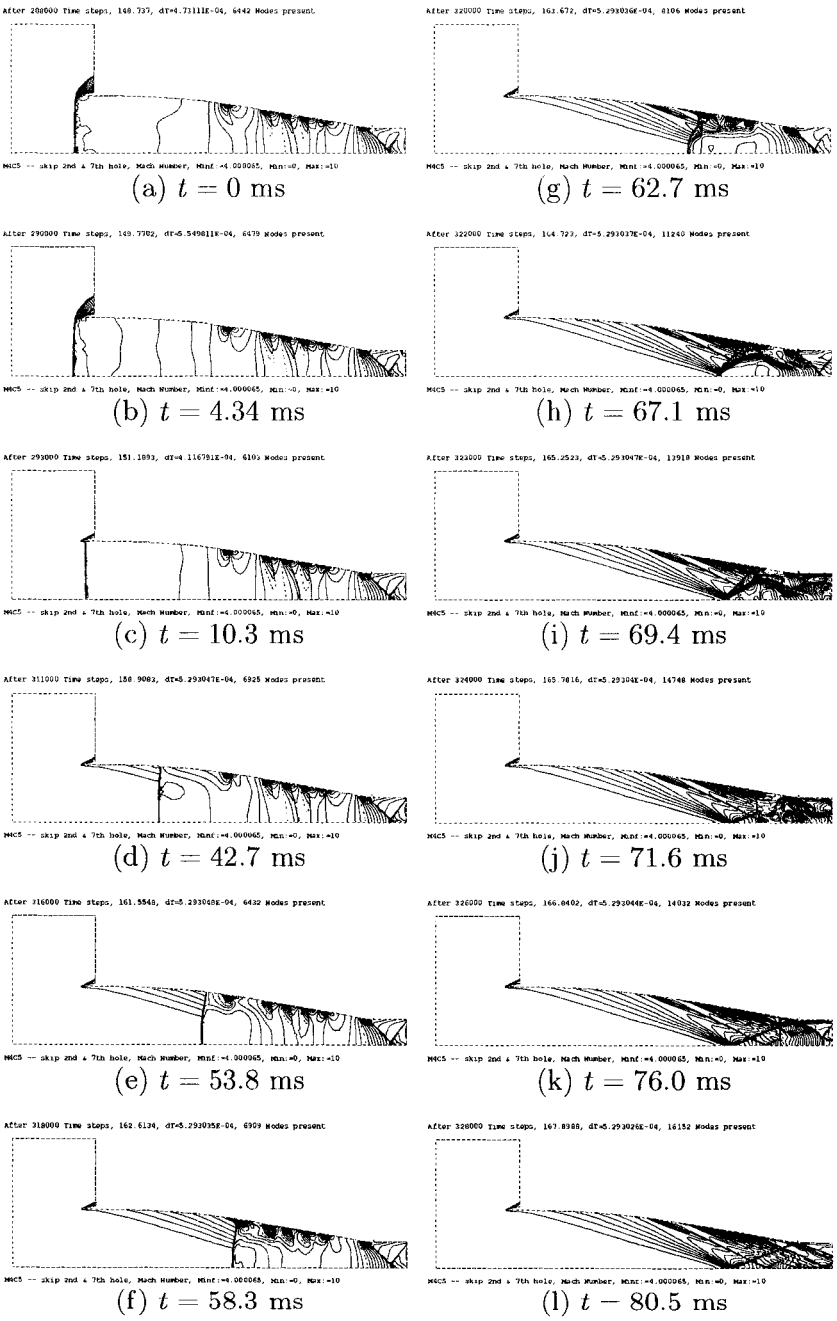

(a) $t = 0$ ms (g) $t = 62.7$ ms

(b) $t = 4.34$ ms (h) $t = 67.1$ ms

(c) $t = 10.3$ ms (i) $t = 69.4$ ms

(d) $t = 42.7$ ms (j) $t = 71.6$ ms

(e) $t = 53.8$ ms (k) $t = 76.0$ ms

(f) $t = 58.3$ ms (l) $t - 80.5$ ms

Figure 4.18: Starting by spillage—Case 3. Iso-Mach contours showing shock swallowing process in a perforated inlet (Model: Busemann.M4C5). $A_p/A_t = 6.77$, $r_i = 1$ m, $t_0 = 517$ ms.

play in inlet starting.

The above considerations led this author to numerically investigate methods of inlet starting where the flow is sufficiently unsteady (*i.e.*, to the extent that it is no longer governed by the quasi-steady limits described by Eq. (2.10) and Eq. (2.11)). For the sake of better organisation, the results have been classified under two separate categories: one pertaining to accelerative starting, and the other dealing with frangible structures; conceptually both fall under "unsteady methods of starting."

4.3.1 Accelerative Starting

To determine the efficacy of accelerative starting, dozens of computations were performed to simulate rapid acceleration of an inlet. In each case, the process is started at a certain initial Mach number M_1 (*e.g.*, $M = 0$), and the inlet is steadily accelerated (*e.g.*, 1000 *g's*), up to a desired Mach number, M_2. Clearly, if the inlet does start in this process, for it to remain started under steady operation, it must be accelerated past the Mach number for which the throat is isentropically choked (Eq. 2.10). Also, quite clearly, if the inlet is accelerated past the point of quasi-steady starting (Eq. 2.12), then it would start readily and any potential benefits of accelerative starting would not be recognisable; it should be noted that this is applicable only to the low Mach number, low contraction inlets.

Three cases are presented: The first one describes a low Mach number, low contraction ratio inlet (Model: Busemann.M2.2.A0.74); this model is located close to Kantrowitz' limit in the inlet parameter space (Fig. 4.1). The second one describes a relatively high contraction, low Mach number inlet (Model: Busemann.M2.2.A0.60), located close to isentropic operational limit. Lastly, results for a high Mach number, high contraction inlet (Model: Busemann.M6.A0.1)

are presented.

Case 1: Low Mach Number, Low Contraction

A Busemann inlet (design conditions: $M_\infty = 2.2$, AR $= 0.74$, $r_i = 1\,\text{m}$), was accelerated at various g-values to determine the efficacy of accelerative starting. For this particular model, if the Mach number reaches a value close to (or higher than) $M_\infty \approx 2.7$, then this inlet will readily start. To avoid this situation, the inlet was accelerated from $M_1 = 0$ to $M_2 = 1.9$, operating at sea level. It was found that even for such a low contraction inlet, 1200 *g's* are required to establish started flow in the manner described above. The acceleration phase was started at time $t = 0\,\text{ms}$ and lasted for 55 ms. It was determined that the same inlet could also be started, if it was accelerated for $t = 217\,\text{ms}$ at $400g$ to a higher Mach number $M_2 = 2.5$; the same was not fruitful at $200g$.

To further understand the level of unsteadiness required for starting, scale analysis for such an inlet (having entrance radius of 1 m) may be performed. If the flight takes place under atmospheric conditions at sea level (density scale, $[\rho] = 1.225\,\text{kg/m}^3$; length scale, $[L] = 1\,\text{m}$; pressure scale, $[p] = 101.325\,\text{kPa}$), then under these conditions, $a_x = g_N\,[g][\rho][L]/[p] \approx g_N \cdot 1 \times 10^{-4}$, that is to say, the inertial terms certainly play a significant role if g_N is $\mathcal{O}(10^4)$ or higher.

Additionally, the role of unsteadiness (*i.e.*, how the flow differs from a quasi-steady one) may also be evaluated by estimating the amount by which the free stream velocity changes during the time period that it takes for a disturbance to propagate from the entrance to the exit of an inlet. In other words,

$$\frac{\Delta u}{c} = \frac{a\Delta t}{c} = \frac{aL_{inlet}}{c^2} = \frac{g_N g L_{inlet}}{c^2}$$

where c is signal velocity, and L_{inlet} is the length of the inlet. For an inlet of length, $L_{inlet} = 10\,\text{m}$, one gets $\frac{\Delta u}{c} = g_N \cdot 1 \times 10^{-3}$ *i.e.*, a significant unsteady influence may be present if g_N is $\mathcal{O}(10^3)$ or higher.

Case 2: Low Mach Number, High Contraction

A 1 m radius inlet having a contraction ratio of 1.67, was accelerated from $M0$ to $M2.2$, and after nearly a dozen simulations, it was determined that the inlet could be started around 3000 *g's* (it could not be started at 2500 *g's*). The acceleration phase was started at time $t = 0\,\text{ms}$ and stopped at $t = 26.6\,\text{ms}$. Fig. 4.19 shows a sequence of frames for the accelerative starting process. It should be pointed out here that this inlet can not be started by over-speeding in the manner of Article 4.2.1.

Case 3: High Mach Number, High Contraction

A Busemann inlet designed for Mach 6, having a contraction ratio of 10 was subjected to extremely high accelerations. It was found that the inlet could be started, if somehow, it was accelerated from rest to $M4.1$ at 20 000 *g's*. It took less than 20 000 *g's*, if the inlet was accelerated for a slightly longer time, *viz.*, starting at rest, go up to Mach 5.07 under $g_N = 15\text{k}$. The acceleration phase was started at time ($t = 0\,\text{ms}$) and stopped at ($t = 11.7\,\text{ms}$). Fig. 4.20 shows a few frames in the process; particulary, the coalescence of iso-Mach fronts, leading to the formation of a shock wave, is interesting in Figs. 4.20(b–d).

This discussion is concluded with the observation that, for unstarted inlets, impulsive inlet motion as well as rapid approaching flow Mach number changes are both ineffective at *g-values* less than several thousand. It is unlikely that the unsteady effects involved in the accelerative starting process will be harnessed

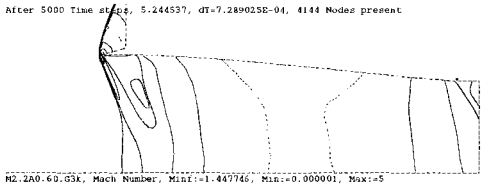

(a) $M_\infty = 1.45$, $t = 18.2\,\text{ms}$

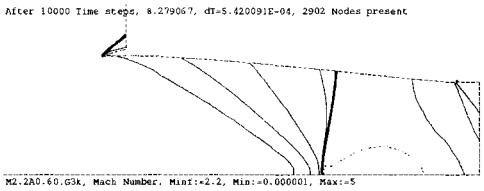

(b) $M_\infty = 2.20$, $t = 28.8\,\text{ms}$

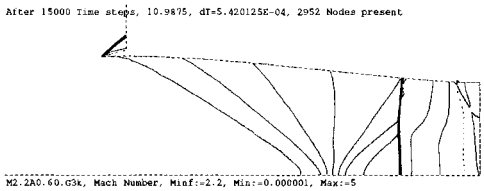

(c) $M_\infty = 2.20$, $t = 38.2\,\text{ms}$

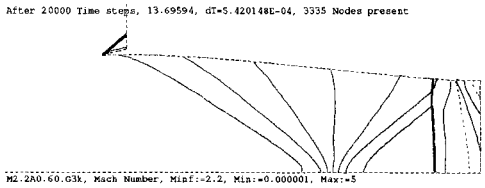

(d) $M_\infty = 2.20$, $t = 47.6\,\text{ms}$

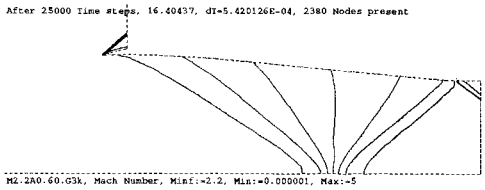

(e) $M_\infty = 2.20$, $t = 57.0\,\text{ms}$

Figure 4.19: Accelerative starting process—Case 2: Low Mach number, high contraction inlet (Model: Busemann.M2.2A0.6). Inlet being accelerated from rest to $M_\infty = 2.2$, at 3000 *g's*.

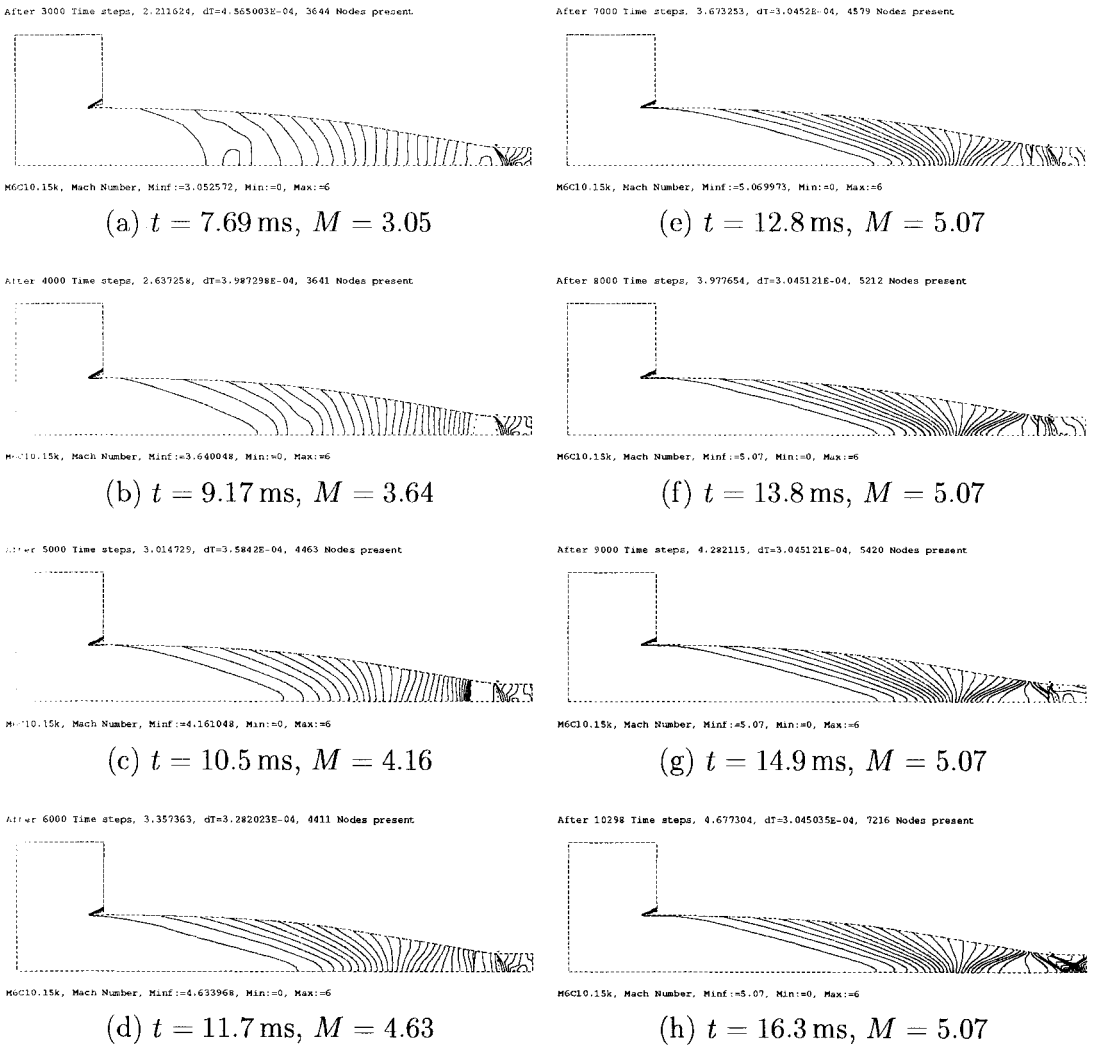

(a) $t = 7.69\,\text{ms}$, $M = 3.05$

(e) $t = 12.8\,\text{ms}$, $M = 5.07$

(b) $t = 9.17\,\text{ms}$, $M = 3.64$

(f) $t = 13.8\,\text{ms}$, $M = 5.07$

(c) $t = 10.5\,\text{ms}$, $M = 4.16$

(g) $t = 14.9\,\text{ms}$, $M = 5.07$

(d) $t = 11.7\,\text{ms}$, $M = 4.63$

(h) $t = 16.3\,\text{ms}$, $M = 5.07$

Figure 4.20: Accelerative starting in progress—Case 3: High Mach number, high contraction inlet (Model: Busemann.M6C10). Inlet being accelerated from rest to $M_\infty = 5$ at $g_N = 15\text{k}$. Displayed time corresponds to an inlet of radius 0.776 m.

by inlet designers of future space planes. It then begs the question: how were earlier researchers able to start extremely high contraction inlets in the gun-tunnel experiments? Perhaps, the answer lies in the initial conditions present in the inlet; the trail veers to a new branch of investigation, leading to the next set of simulations.

4.3.2 Frangible Structures

In a natural progression to accelerative starting, motivation in pursuing ways to harness flow unsteadiness, eventually led to the possibility of employing a diaphragm in front of the inlet. The purpose of this diaphragm would be to provide a near vacuum initial state inside the inlet, in a manner similar to low pressures used in gun tunnels. Upon rupture of the diaphragm, high spatial gradients in the flow would be imposed locally; possibly, this effect could lead to a started inlet if the bow shock was fully swallowed. For organisational sake, the results are classified into two separate categories according to the geometry used for the diaphragm—planar and conical. Although related, each case is discussed independently below.

4.3.2.1 Planar Diaphragm

In this context, the first set of computations were performed with a planar diaphragm (perpendicular to free stream flow, located at the entrance plane) in an attempt to start a full Busemann inlet. Various combinations of inlet contraction ratio, free stream Mach number and inlet evacuation pressure were examined. The general procedure was as follows: A diaphragm was placed at the inlet plane with the exit plane also plugged (solid wall boundary). Then, the inlet volume was partially evacuated (set to a low pressure). Then, steady flow was estab-

lished, resulting in the formation of a bow wave in front of the inlet as shown in Fig. 4.21a.

A noticeable shock motion was observed after instantaneous removal of the diaphragm; the extent of this motion in the downstream direction depended on the free stream Mach number as well as the initial conditions specified inside the inlet volume. Figures 4.21–4.24 demonstrate the general principle applied to a relatively low contraction geometry (Model: Busemann.M6.0A0.31.θ90.P0.85)†. In the inlet parameter space, this geometry lies at a point, where it can not be started by over-speeding, so that a start obtained here must be attributed to unsteady effects.

Figure 4.21a shows steady state solution just prior to rupture, with a bow wave situated ahead of the intact diaphragm. Figure 4.21b shows a rightward moving shock and contact surface, and the leftward running expansion waves, $514\mu s$ after rupture. The expansion causes pressure to decrease behind the bow shock, causing it to move inside the inlet. Figure 4.21c shows an oblique (locally conical) shock at the lip, which allows the flow to turn in towards the inlet (before rupture, the flow ahead of the diaphragm had a y-component of velocity); this oblique shock is then overrun by the bow wave resulting in a merged near-normal shock, travelling in the downstream direction.

Figure 4.22 shows flow evolution as the entire shock-train travels rightward; the diaphragm shock (the right-most one) and the contact surfaces can be seen leaving the computational domain.

Figure 4.23 shows normal shock moving slowly in the downstream direction, and leaving behind, a partially started inlet. In this partially started inlet, up-

†Here, $\theta = 90$, indicates angle of diaphragm, *i.e.*, planar diaphragm, perpendicular to flow. P0.85 refers to the ratio of initial evacuation pressure to the static value in free stream.

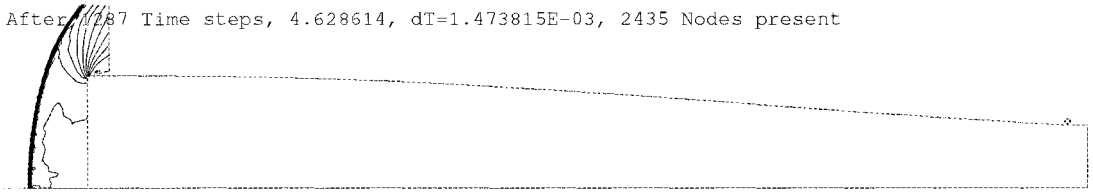

(a) steady flow with intact diaphragm, $t = t_0 = 16.1\,\text{ms}$.

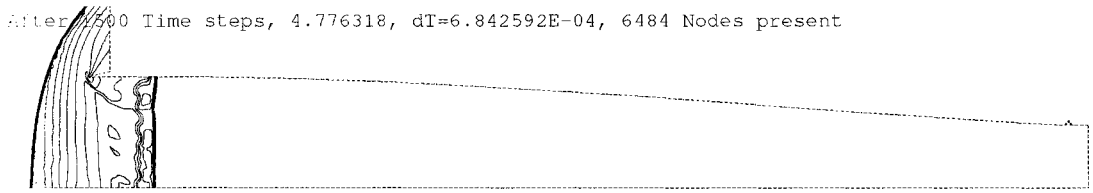

(b) flow evolution just after instantaneous removal at Mach 6, $t = 16.61\,\text{ms}$.

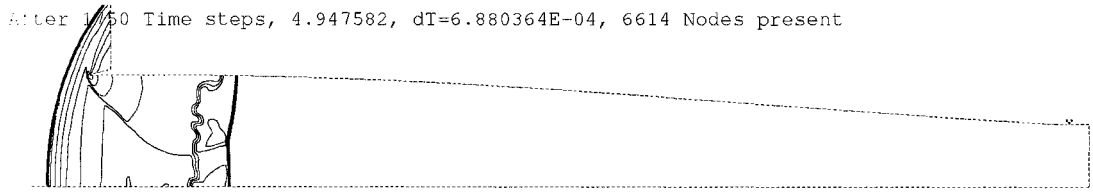

(c) oblique wave at the lip, $t = 17.2\,\text{ms}$.

Figure 4.21: Planar diaphragm rupture—Isopycnics showing flow evolution for a relatively low contraction inlet (Model: Busemann.M6.0A0.31), with initial internal pressure of 0.85.

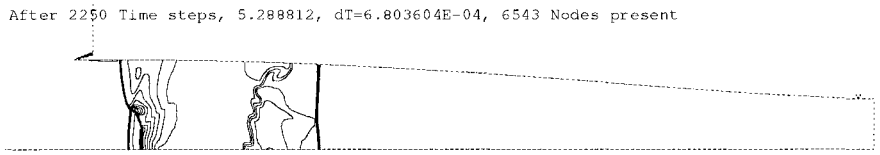

(a) after merger of bow-wave with the oblique wave, $t = 18.4\,\text{ms}$.

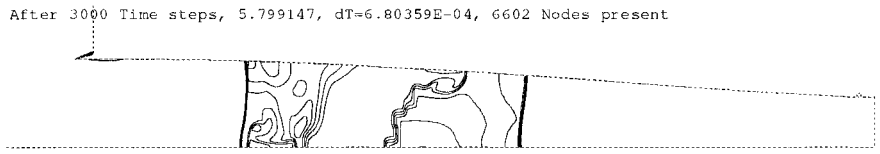

(b) shock train moving in the downstream direction, $t = 20.16\,\text{ms}$

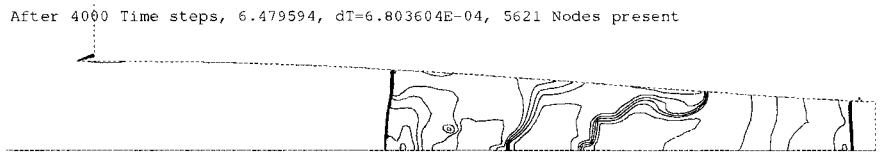

(c) diaphragm shock being swallowed, $t = 22.53\,\text{ms}$

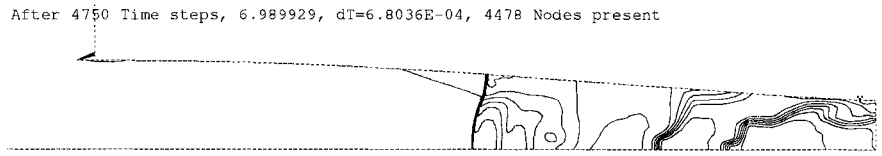

(d) partially started inlet, $t = 24.30\,\text{ms}$

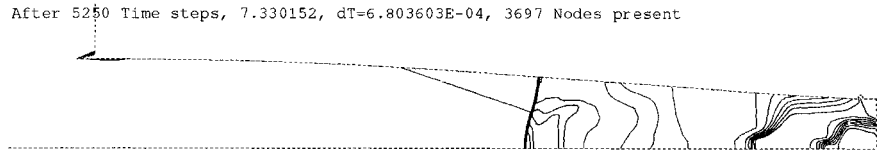

(e) partially started inlet, $t = 25.50\,\text{ms}$

Figure 4.22: Planar diaphragm rupture—Isopycnics showing flow evolution for a Mach relatively low contraction (Model: Busemann.M6.0A0.31) inlet, with initial internal pressure of 0.85.

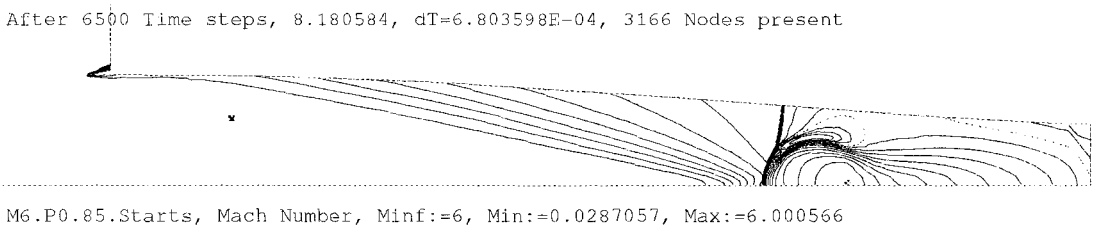

Figure 4.23: Planar diaphragm rupture—Iso-Mach contours showing partially started flow, $t = 28.4$ ms.

stream of shock, the flow is supersonic, *i.e.*, it is Busemann conical flow. When the shock is downstream of the origin, a conical shock must start to form. It was observed that as the shock approaches the "origin" of this particular Busemann inlet (Fig. 4.23), it appears to interact with the formation of the regular conical shock. This interaction between a planar and a conical shock leads to multi-dimensional phenomena, which appear to cause formation of a large vortex behind the moving normal shock (structure is visible and more pronounced near the inlet surface). Eventually, this new shock structure is also swallowed leading to a fully started inlet as shown in Fig. 4.24.

Observed Trends

Low contraction inlets such as the M6.0A0.56.θ90 (P1.0) start easily, perhaps not surprisingly. Attempts were also made to start the M2.2A0.6.θ90 (P0.0001), one of the high contraction models (Fig. 4.1 for reference, *v.s.*). Even at the extremely low internal pressures (high pressure ratios across diaphragm), the inlet could not be started. Similar attempts were also not fruitful for Models: M3A0.34.θ90 (P0.0001), M4C5.θ90 (P0.0001), and M6.0A0.10.θ90 (P0.00001).

Figure 4.25 shows a summary of results obtained for (Model: M6.0A0.31.θ90), demonstrating the effects of free stream Mach number on the value of initial

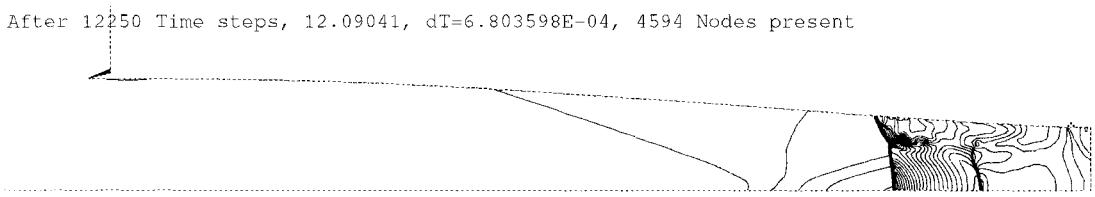

(a) $t = 42.04\,\text{ms}$

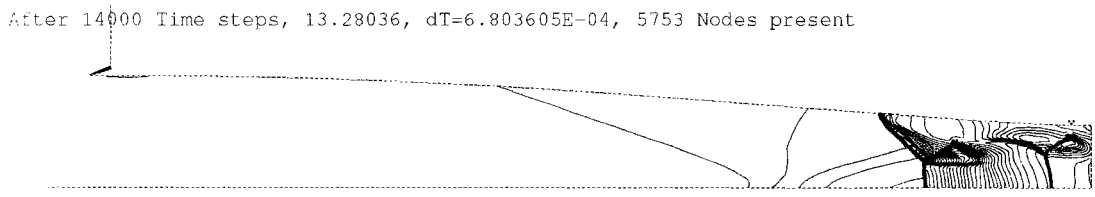

(b) $t = 46.18\,\text{ms}$

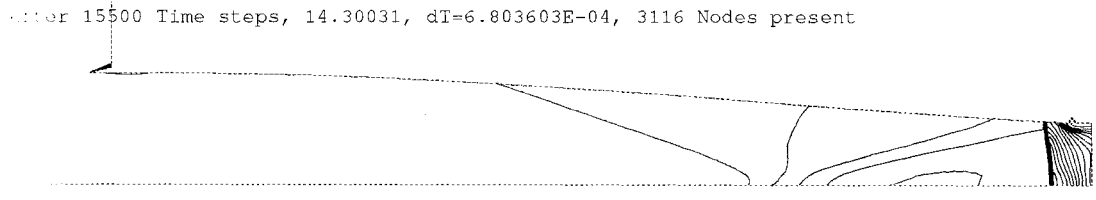

(c) $t = 49.72\,\text{ms}$

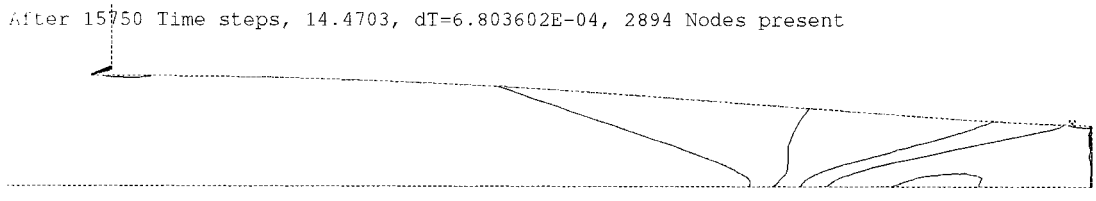

(d) $t = 50.31\,\text{ms}$

Figure 4.24: Planar diaphragm rupture—Isopycnics showing establishment of fully started flow (Model: Busemann.M6.0A0.31).

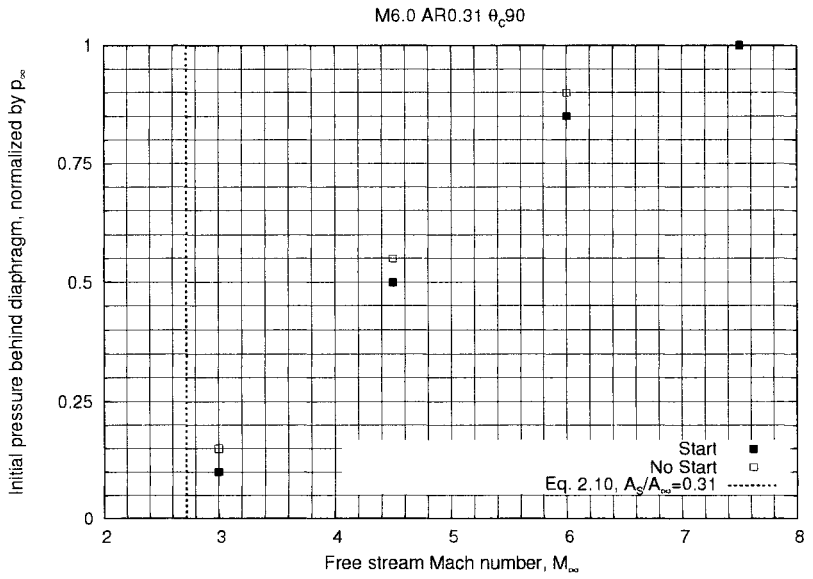

Figure 4.25: Effects of Mach number on required pressure, for starting with a planar diaphragm, (Model: M6.0A0.31.θ90.M*.P*). Estimated computational cost to produce this figure: 150 Tflop.

internal pressure that is required for starting. This result suggests that for the case of a planar diaphragm, as one approaches the operational limit described by Eq. (2.10), it also becomes harder to attain started flow under the aegis of unsteady flow phenomena. It is clear that higher values of initial pressure ratio across the diaphragm are conducive to unsteady starting.

Additionally, from the point of view of flow-evolution, it may be noticed that a core of high density fluid exists behind the bow-wave. Due to the geometry of the flow prior to rupture, a significant portion of this slug must be swallowed upon rupture, and this can hinder starting if the inlet ever becomes choked. Thus, it is desirable to minimise or eliminate this geometrical feature of the flow behind the planar diaphragm. Slight variation of the diaphragm geometry are introduced below so that (upon rupture) the flow evolves differently, and leads to a fully started inlet, rather than causing spontaneous unstarting after a partial start.

4.3.2.2 Conical Diaphragm

In an attempt to establish steady started flow in a high contraction inlet, a set of computations was performed with (Model: Busemann.M6.0A0.1), using instantaneous rupture of a new kind of diaphragm. For axisymmetric inlets, a simple change in geometry was made, and the planar diaphragm was replaced with a conical one. The general procedure was as follows: First, a conical diaphragm was placed in front of the inlet, with its apex pointing in the upstream direction, and with its base coinciding with the leading edge of the inlet. Second, the exit plane was plugged and the inlet volume was partially evacuated; steady flow was then established, resulting in a conical shock that was attached at the cone apex as shown in Fig. 4.26. Lastly, the diaphragm was removed and the flow allowed to evolve.

Figures 4.27–4.28 show flow development after a conical diaphragm having a semi-vertex angle of 14 degrees was removed at Mach 6. It is clear that this simple change in the diaphragm geometry leads to a fundamentally different shock structure, as compared to the planar diaphragm case. The right running shock and contact surfaces are initially both conical and head towards the axis of symmetry as shown in Fig. 4.27a. The external conical shock is initially weak and further made even weaker by the left running expansion waves. A shock wave is present on the inside, attached to the inlet lip, allowing for the flow to turn inwards and

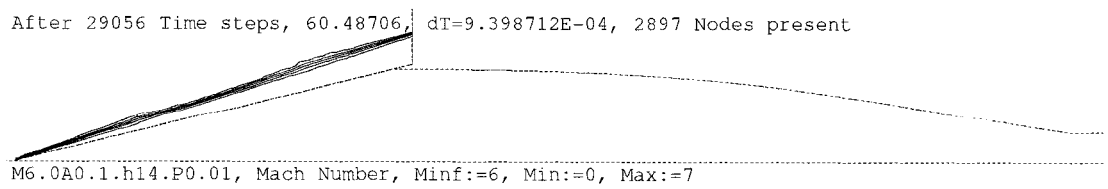

Figure 4.26: Conical diaphragm rupture—Iso-Mach contours showing steady flow with intact diaphragm (Model: M6.0A0.1θ14.P0.01), $t = t_0 = 210.3\,\text{ms}$. Inlet radius is 1 m.

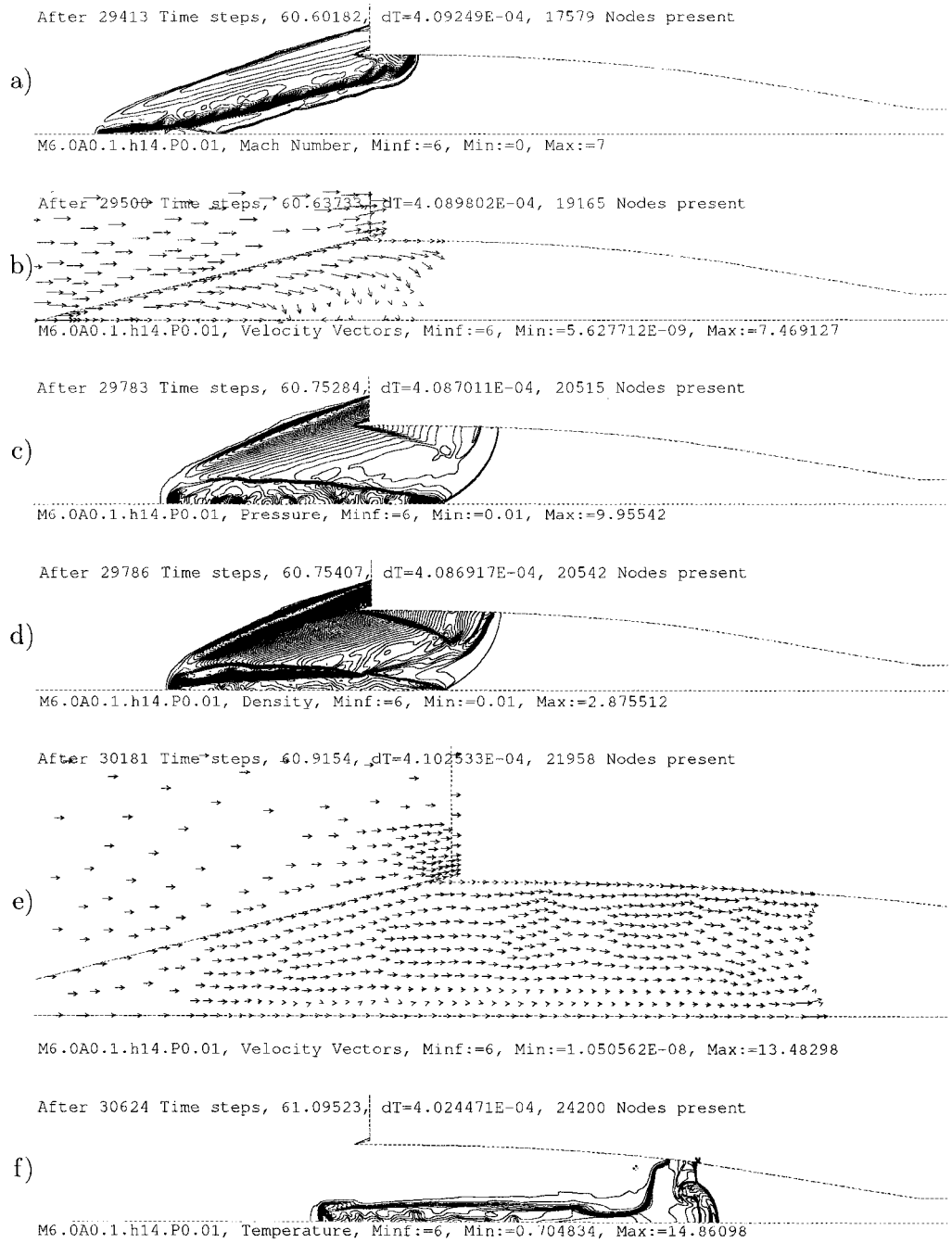

Figure 4.27: Conical diaphragm rupture: (a) iso-Mach contours at $t = 210.7\,\text{ms}$; (b) velocity vectors at $t = 210.8\,\text{ms}$; (c) isobars at $t = 211.2\,\text{ms}$; (d) isopycnics at $t = 211.2\,\text{ms}$; (e) velocity vectors at $t = 211.8\,\text{ms}$; (f) lines of constant temperature at $t = 211.8\,\text{ms}$.

become parallel to the inlet surface. The general fluid motion is in the downstream direction as well as towards the axis as shown in Fig. 4.27b.

The right running shock reflects off the axis as shown in Fig. 4.27c, leaving behind a core of high temperature (low density) mass near the axis (in this region, $T \approx 8T_\infty$). A non-reflected portion of the shock becomes near-normal and continues to move in the downstream direction; this is the right most structure. The reflected shock is horizontal in orientation, and is moving towards the inlet surface, away from the axis.

Close to the axis, Fig. 4.27d shows a shear layer (not present in the pressure plot), separating the high-speed outer flow from the nearly stagnant inner mass as shown in Fig. 4.27e; after shock reflection, high temperatures exists in this inner mass, leading to relatively low density ($\rho \approx 0.17\rho_\infty$). A bow-wave forms (more visible in Fig. 4.28 than in Fig. 4.27d , in front of this slow-moving core (in this region, $M < 0.4$, compared to $M5.5$ in the outer flow, above the slip layer). The outer most flow (between the reflected shock and the inlet surface) is moving the fastest ($M \approx 5.5$–7). Downstream of the slow-moving core, Fig. 4.27e shows the flow catching up in speed as it goes around the lump. Figure 4.27f shows the high temperature region trapped behind the slip layer, along the axis, as the overall structure progresses downstream.

Figure 4.28 shows a sequence of frames, summarising the entire process. It is clear, during this process that high spatial gradients exist in all flow variables. The resulting flow is complex, neither steady nor one-dimensional, and is definitely not restricted by the limiting criteria described in Articles 2.1.4 and 2.1.5.

From the gas dynamic viewpoint, this is indeed an attractive way of starting inlets. It might be possible to use a higher initial pressure inside the inlet, or to start at a lower free stream Mach number; these notions formed a basis for further

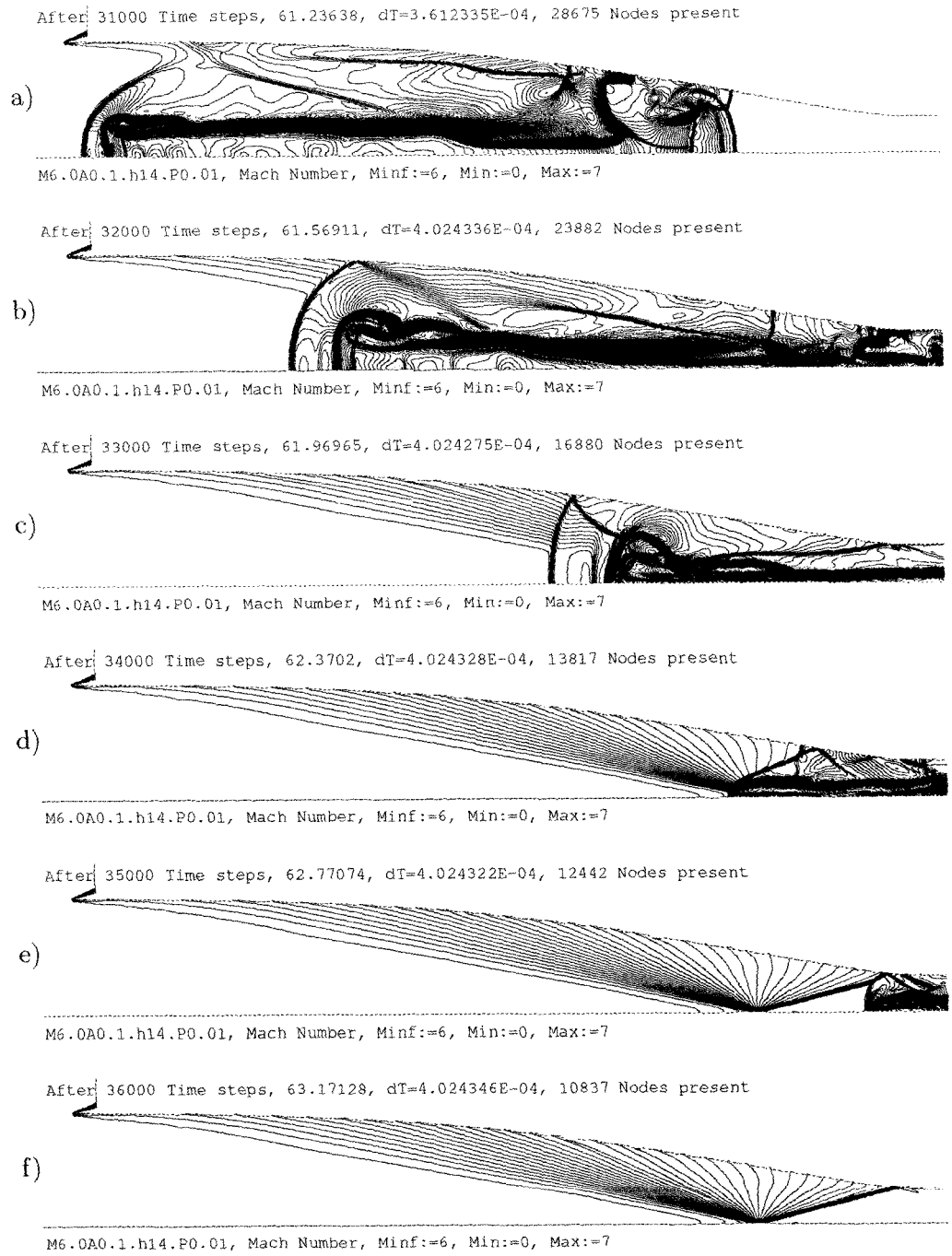

Figure 4.28: Conical diaphragm rupture—Iso-Mach contours showing the overall flow evolution after instantaneous rupture. $t = (212.9, 214.1, 215.5, 216.9, 218.3, 219.6)$ ms.

study in examining effects of cone angle and free stream Mach number on starting ability of the above model inlet.

Observed Trends

Results obtained with conical diaphragms show that starting occurs if the initial internal pressure is reduced to a low value—typically one percent of the free stream pressure. Attainment of started flow appears to be a function of this pressure as well as the cone angle. This section presents a summary of the results from (Model: Busemann.M6.0A0.10), obtained by systematic variation of these two parameters.

As noted earlier (Article 4.3.2.1), it is more difficult to start high contraction inlets at low Mach numbers than at higher ones. On the other hand, it is desirable to have an inlet started at a Mach number lower than its design value. To avail this, one may consider at $M_\infty = 4.5$ for instance, the effect of cone angle in determining the highest initial pressure ratio that will permit starting.

Figure 4.29 shows a plot of highest permissible pressure as a function of diaphragm angle. From the results obtained, it is evident that in this parameter space, there exists an optimal angle for the conical diaphragm. For the particular model under consideration, this value appears to be $\sim 35°$, thereby significantly relaxing the requirement on initial pressure. It should be pointed out that previous results were for $M_\infty = 6$, where it should be much easier to start this inlet. To examine this hypothesis, a set of computations was performed. Figure 4.30, confirms this statement, and shows that at higher free stream Mach numbers, it is generally possible to start with a higher initial pressure inside the inlet. Conversely, at low Mach numbers, as one approaches the isentropic limit described by Eq. (2.10), it becomes increasingly difficult to attain started flow.

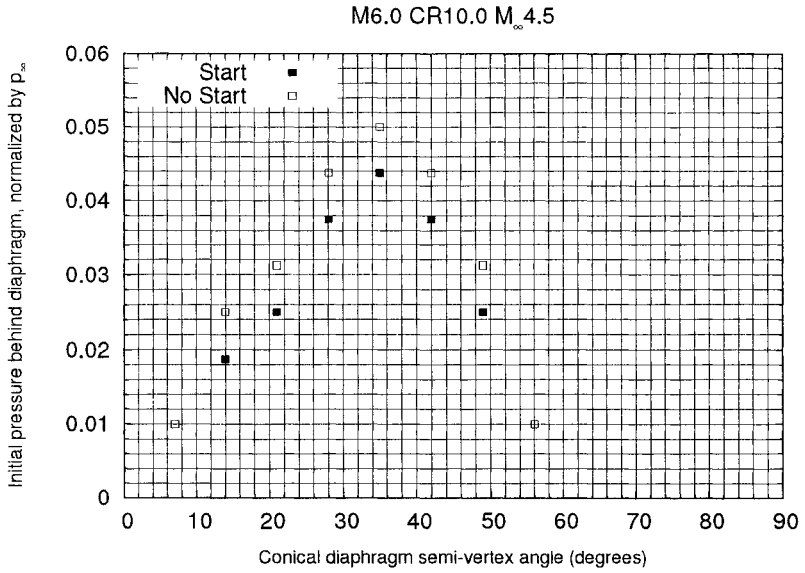

Figure 4.29: Effect of cone angle on required pressure, for starting with a conical diaphragm. Rupture at $M_\infty = 4.5$, (Model: M6.0A0.10.M4.5). Estimated computational cost to produce this figure: 500 Tflop.

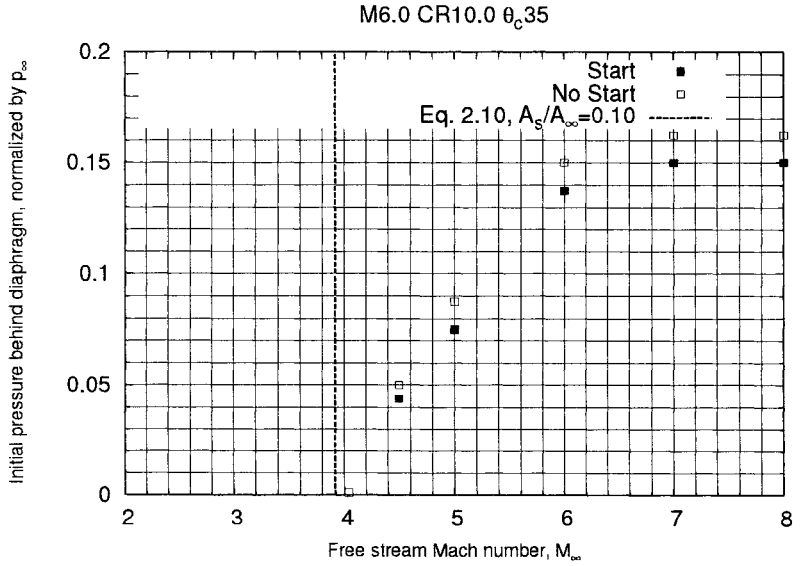

Figure 4.30: Effect of Mach number on required pressure, for starting with a conical diaphragm of semi-vertex angle, $\theta_c = 35°$, (Model: M6.0A0.10.θ35). Estimated computational cost to produce this plot: 300 Tflop.

Chapter 5

Concluding Remarks

A numerical study has been conducted to examine the effects of boundary-imposed, high temporal and spatial gradients in flow on the *inlet starting* phenomenon. Results have been shown in the form of go, no-go answers for flow starting, through a range of free stream Mach numbers, for different classes of inlets, at various area contraction ratios. Methods and conceptual devices have been proposed to facilitate unsteady starting.

It has been shown that simple starting and unstarting criteria, based on the assumption of one-dimensional flow, hold well, even in multi-dimensional flows/geometries. This implies that quasi-steady starting and unstarting processes are dominated by inherently one-dimensional phenomena. It has been concluded that unstarting takes place in fixed geometry inlets, when the flight Mach number is reduced to the value that corresponds to sonic flow at the throat. It has been found that for a high-contraction Busemann inlet, the lower limit on Mach number described by isentropic area ratio is slightly optimistic (by +0.03 in Mach number)—that is, in practice unstarting takes place at higher values of Mach number. It has been determined that after unstarting, the bow wave takes

a relatively long time to reach a stable position; the oscillations are, of course, of little consequence in an unstarted inlet.

Variable Mach number studies of fixed geometry Busemann inlets have shown that the conical shock in Busemann flow is highly stable and that the shock angle increases gradually with a decrease in free stream Mach number. There exists a strong indication that multiple "design points" exist in the Busemann inlet parameter space. Further research needs to be conducted to confirm this hypothesis. The primary design condition for a Busemann inlet has been used to verify computational tools.

It has been shown that slit-like perforations can be employed to achieve quasi-steady starting. In this context, for an inlet designer, the issue is not how to start an inlet using perforations, but how to remove perforations once the starting process has come to completion. Mass flow relief, as provided by slits is essentially a steady flow phenomenon. This is true even when the opening and closing of the slits is a rapidly occurring process. Slit theory based on Prandtl-Meyer flow may be used to estimate spillage through wall perforations based on two parameters, *viz.*, Mach number at the leading edge of the slit and the pressure ratio across the slit. Results obtained from computational experiments, have been found to agree with this analysis, indicating that flow spillage through slits may be represented by Prandtl-Meyer flow in concert with the oblique shock theory. For a perforated diffuser, starting takes place if a sonic line, at the leading edge of a slit, occurs at an area ratio equal to, or higher than, that corresponding to Kantrowitz' limit. It has been found that in the unstarted mode, the flow coefficient typically has a value between 0.2 and 0.6, and as a result, a large wall perforation area is required to obtain flow starting in high-contraction inlets.

It has been shown that purely accelerative starting is generally not possible

for inlets of any positive contraction, unless thousands of g's of acceleration are imposed. This is in agreement with scale-based analysis of accelerative starting. Thus, boundary-imposed temporal gradients do not lead to sufficiently unsteady flow phenomena so as to easily permit starting beyond Kantrowitz' limit.

It has been proposed that removal of frangible structures, such as fast rupturing diaphragms, be used to impose sufficiently high spatial gradients as are necessary to permit starting beyond Kantrowitz' limit.

It has been concluded that medium contraction inlets may be started using planar diaphragms—in some cases, even without requiring initial evacuation of the inlet. Effects of free-stream Mach number and initial pressure behind the diaphragm, have been documented. Results suggest that as one approaches the isentropic limit, it becomes more and more difficult to attain started flow under the aegis of unsteady flow phenomena. It has been determined that higher initial values of external to internal pressure ratio across the diaphragm are conducive to unsteady starting.

It has been concluded that flow starting in high-contraction inlets can be facilitated by instantaneous removal of a forward-pointing conical diaphragm from inlet entry. It has been demonstrated that optimal cone angles exist for diaphragms of conical shape, and that it is easier to start a hypersonic inlet at high Mach numbers. It has been shown that the starting problem becomes more difficult as one approaches the isentropic limit in the inlet parameter space.

References

[1] J. Anderson. *Hypersonic and High Temperature Gasdynamics.* McGraw-Hill Book Company, 4th edition, 1989.

[2] F. Billig, P. Waltrup, and R. Stockbridge. Integral-rocket dual-combustion ramjets. *AIAA Journal of Spacecraft and Rockets*, 17(5):416–424, September–October 1980.

[3] A. Busemann. Infinitesimal Conical Supersonic Flow. Tech. Memo. 1100, NACA, March 1947. Translated by Mary L. Mahler and Robert T. Jones.

[4] J. Clark. An Experimental Investigation of a Supersonic Two-Dimensional Perforated Inlet at a Nominal Free-Stream Mach Number of 2.50. Tech. Note 24, UTIA, 1958.

[5] J. Evvard and J. Blakey. The use of perforated inlets for efficient supersonic diffusion. Research Memo. E7C26, NACA, June 1947.

[6] K. Foelsch. A New Mothod of Designing Two-Dimensional Laval Nozzles for a Parallel and Uniform Jet. North American Aviation, NA-46-235, 1946.

[7] K. Foelsch. The Analytic Design of an Axially Symmetric Laval Nozzle for a Parallel and Uniform Jet. *Journal of Aeronautical Sciences*, 16(3), 1949.

[8] H. Hunczak and E. Kremzier. Characteristics of perforated diffusers at free-stream Mach number 1.90. Research Memo. E50B02, NACA, May 1950.

[9] J. John. *Gas Dynamics.* Allyn and Bacon, 2nd edition, 1984.

[10] A. Kantrowitz. The formation and stability of normal shock waves in channel flows. Tech. Note 1225, NACA, March 1947.

[11] A. Kantrowitz and C. Donaldson. Preliminary Investigation of Supersonic Diffusers. Adv. confid. report L5D20, NACA, May 1945.

[12] N. Komerath. AE 6031—Unsteady Aerodynamics, lecture notes. Georgia Institute of Technology, Fall, 2000.

[13] H. Liepmann and A. Roshko. *Elements of Gasdynamics.* John Wiley & Sons, Inc., 1953.

[14] R. Löhner. Adaptive h-refinement on 3-D unstructured grids for transient problems. AIAA 89-0365, 1989.

[15] Mayura Software Inc. Mayura Draw. `http://www.mayura.com`, 1993–2002.

[16] S. Mölder and N. D'Souza. Applicability of hypersonic small-disturbance theory and similitude to internal hypersonic conical flows. *Journal of Spacecarft and Rockets*, 7:149–154, February 1970.

[17] S. Molder, P. Sullivan, J. Sislian, J. Gottlieb, R. McGregor, T. Paisly, S. Weston, R. Rogers, R. Hawboldt, R. Deschambault, C. Groth, D. Hawken, Z. He, L. Chen, and K. Gordon. Investigations in the fluid dynamics of scramjet inlets. Final Contract Report USAF, Contract No: F33615-87-C-2748; JHU, Contract No: APL 602235-0, Ryerson Polytechnic Institute and University of Toronto Institute for Aerospace Studies, 1992.

[18] S. Mölder and E. Szpiro. Busemann Inlet for Hypersonic Speeds. *Journal of Spacecarft and Rockets*, 3(8):1303–1304, 1966.

[19] E. Mossman and F. Pfyl. An experimental investigation at Mach numbers from 2.1 to 3.0 of circular-internal-contraction inlets with translating centerbodies. Research Memo. A56G06, NACA, October 1956.

[20] NASA. Image Gallery. `URL=http://spaceflight.nasa.gov/gallery/images`.

[21] NASA. Official Website. `URL=http://www.nasa.gov`.

[22] J. Nettles. The effect of initial rate of subsonic diffusion on the stable subcritical mass-flow range of a conical shock diffuser. Research Memo. E53E26, NACA, July 1953.

[23] T. Saito, P. Voinovich, E. Timofeev, and K. Takayama. Development and application of high-resolution adaptive numerical techniques in shock wave research center. In E. Toro, editor, *Godunov Methods: Theory and Application*, pages 763–784. Kluwer Academic/Plenum Publishers, 2001.

[24] R. Scherrer and W. Anderson. Investigation of the performance and internal flow of a variable-area, variable-internal-contraction inlet at Mach numbers of 2.00, 2.50, and 2.92. Research Memo. A58C24, NACA, July 1958.

[25] G. A. Sod. A survey of several finite difference schemes for hyperbolic conservation laws. *Journal of Computational Physics*, 27:1–31, 1978.

[26] R. Tahir. 3DViewer—One-, two-, and three-dimensional, structured and unstructured mesh visualization library for Windows® NT. email: `rbt@rogers.com`, 1999–2003.

[27] R. Tahir, E. Timofeev, and P. Voinovich. `SolverII`—Two-dimensional, multi-block, adaptive, unstructured, time-dependent CFD application for MS Windows®. email: `rbt@rogers.com, timofeev@sympatico.ca, vpeter@scc.ioffe.ru`, 1999–2003.

[28] E. Timofeev, R. Tahir, and S. Molder. Analysis and CFD Work Related to Hypersonic Inlet Flow Starting. SBIR, Tech. Report, Taitech subcontract TS02-37-002, S. Molder and Associates, December 2002.

[29] E. Toro. *Riemann Solvers and Numerical Methods for Fluid Dynamics.* Springer-Verlag, 2nd edition, 1999.

[30] P. Voinovich. Two and three-dimensional, unstructured, adaptive, Euler codes. email: `vpeter@scc.ioffe.ru`, 1993–2003.

[31] P. Voinovich and A. Galyukov. UGG. Two- and three-dimensional, triangular and tetrahedral, unstructured grid generators. email: `vpeter@scc.ioffe.ru`, 1993–1999.

[32] D. Wie and S. Mölder. Application of Busemann Inlet Designs for Flight at Hypersonic Speeds. In *Aerospace Design Conference.* AIAA 92-1210, February 1992.

[33] D. Wilcox. *Turbulence Modeling for CFD.* DCW Industries, 2nd. edition, 1998.

[34] T. Williams, C. Kelley, R. Lang, D. Kotz, J. Campbell, G. Elber, A. Woo, and many others. gnuplot. `http://gnuplot.info`, 1986–1993, 1998–2002.

[35] J. Wu. An Experimental Study of Perforated Intake Diffusers at a Free-Stream Mach Number of 2.50. Tech. Note 69, UTIA, 1960.

Glossary

AMR Adaptive Mesh Refinement (classical red-green h-refinement)

CFD Computational Fluid Dynamics

CPDE Computational Partial Differential Equation(s)

DARPA Defense Advanced Research Projects Agency

ET External Tank(s)

LEO Low Earth Orbit(s)

MHM MUSCL-Hancock Method

MUSCL Monotone Upwind Scheme for Conservation Laws

NACA National Advisory Committee for Aeronautics

NASA National Aeronautics and Space Administration

NASP National Aerospace Plane

ODE Ordinary Differential Equation(s)

RBCC Rocket Based Combined Cycle

SRB Solid Rocket Booster(s)

SSTO Single Stage To Orbit

STS Space Transportation System

TVD Total Variation Diminishing

UGG Unstructured Grid Generator

USAF United States Air Force

WWII World War II

Index